Volume 7, Issue 1, 2024 e-ISSN: 2667-484X

KOCAELI JOURNAL OF SCIENCE AND ENGINEERING

http://dergipark.org.tr/kojose
kojose@kocaeli.edu.tr

Printed By

Kocaeli University - Graduate School of Natural and Applied Sciences - Umuttepe Campus 41001, Kocaeli / TURKEY
Tel: +090 (262) 303 35 56 Fax: +090 (262) 303 30 33 E-mail: kojose@kocaeli.edu.tr

Kocaeli University

Kocaeli Journal of Science and Engineering

http://dergipark.org.tr/kojose

Koc. J. Sci. Eng., 7(1): (2024) 1-8 https://doi.org/10.34088/kojose.1228645

Kocaeli University

Kocaeli Journal of Science and Engineering

http://dergipark.org.tr/kojose

Dynamics of Hot Exciton Relaxation in Conjugated Polymer Chain

Muhammet Erkan KOSE [1,*], Esra KOSE [2], Zafer ERZURUMLUOGLU [3]

[1] *Department of Chemistry, Kocaeli University, Kocaeli, 41001, Turkey,* ***ORCID:*** *0000-0003-3153-7436*
[2] *Department of Physics, Kocaeli University, Kocaeli, 41001, Turkey,* ***ORCID:*** *0000-0001-7135-6432*
[3] *Department of Chemistry, Kocaeli University, Kocaeli, 41001, Turkey,* ***ORCID:*** *0000-0003-2332-1029*

Article Info

Research paper

Received : January 3, 2023
Accepted : March 23, 2023

Keywords

Conjugated Polymer
Dynamics
Energy Transfer
Exciton
Exchange Coupling

Abstract

Hot excitons are formed after photoexcitation of conjugated polymer chains. Hot excitons relax and convert into cold excitons with the aid of vibrational modes. In this study, the dynamics of such conversion is studied within the strong coupling regime. It has been found that the magnitudes of electronic coupling integrals for hot exciton relaxation are mostly due to exchange interactions between the interacting units. During relaxation, hot excitons oscillate back and forth between two different sites until they lose their extra energy. The time step for each oscillation has been found as small as 0.3 fs. It has also been found that photoexcited states in conjugated polymer chains do not necessarily localize at their initial location formed. Monte-Carlo simulations show that hot excitons can sustain their coherent motion along the conjugated backbone to some extent before total relaxation.

1. Introduction

The electronic energy transfer between chromophores is generally studied in the strong and weak coupling regimes [1]. Coherent energy transfer is usually seen in the strongly coupled chromophores with significant exchange correlations among the clouds of the interacting units [2, 3]. When the chromophores are well separated in space with negligible overlap of wavefunctions, incoherent energy transfer then becomes the major mechanism for energy transfer through Coulombic interactions [4, 5]. One of the famous examples in the weak coupling limit is Förster energy transfer, which assumes that energy transfer rate from a donor chromophore to an acceptor chromophore occurs in a time scale much shorter than relaxation rate of acceptor site. Thus, there is a little chance of energy transfer back to donor chromophore from acceptor chromophore [6]. On the other hand, strong coupling of donor and acceptor chromophores causes oscillation of photoexcited energy between the donor and the acceptor sites. Thus, the system can be seen as single pair with well delocalized wavefunctions, which does not allow distinguishing the donor chromophore from the acceptor chromophore [7]. Strong coupling between the chromophores causes energy level splitting. One of the well-known examples of energy transfer in the strong coupling regime is observed in the energy transfer interaction of chromophores in H- and J-aggregates of conjugated small molecules [6].

Upon photoexcitation in conjugated systems, hot excitons are formed [8]. Such excitons lose their energy to bath and form cold excitons from where emission is observed in luminescent materials. The relaxation dynamics of hot excitons in conjugated materials in ultrafast time scales are difficult to study both theoretically and experimentally [9]. The reason stems from the fact that expensive instrumentation is needed to analyze the excitonic decay mechanisms by using indirect methods [10-12]. Theoretical background that describes relaxation dynamics of highly energetic excitons is not adequately developed yet [13-15]. Since there is significant wavefunction overlap anticipated among interacting units,

* Corresponding Author: erkan.kose@kocaeli.edu.tr

the use of Förster type energy transfer mechanism for strongly coupled systems is not appropriate. As a consequence, more advanced theories and approaches need to be utilized for simulation of hot exciton relaxation dynamics. There are numerous methods in the literature that examines energy transfer processes in the weak coupling regime [13, 16, 17]. Strong coupling regime studies are mostly focused on systems with significant wavefunction overlap between two different chromophores [7]. In this article, an attempt has been made to understand the relaxation dynamics of hot excitons in a conjugated polymer chain by using theoretical methodologies developed for strongly coupled chromophores [18]. The results indicate that exchange interactions are the dominant type of interactions when hot excitons oscillate between different sites during cooling process.

2. Theoretical Methods

An electronically excited chromophore may transfer its energy to a nearby non-excited chromophore due to Coulombic interaction and exchange correlations. Since the nearest chromophores next to the initially excited chromophore should be considered, exchange correlations become important part of excitonic dynamics along a polymer chain. An isolated two-level chromophoric system (a donor (D) and an acceptor (A)) is the starting point to describe the hot exciton relaxation dynamics through energy transfer to lower energy sites. In such dual system, $|D_0A_0\rangle$, $|D_1A_0\rangle$, $|D_0A_1\rangle$, and $|D_1A_1\rangle$ represents ground state, singly excited states, and doubly excited state, respectively. Since there are four states, the interaction between the donor and the acceptor chromophores should ideally be investigated in a 4 × 4 matrix. Although strong coupling regime is operative in such situation, it is assumed that inter-chromophoric coupling is not involved in the mixing of the ground state and the doubly excited state. Therefore, there are two states left, $|D_1A_0\rangle$ and $|D_0A_1\rangle$, that describes energy transfer from a donor chromophore to an acceptor chromophore. Then, after following Harcourt model [19] the electronic coupling between these two states can be represented as:

$$V \cong \langle D_1A_0|\hat{V}|D_0A_1\rangle \cong 2\langle dd'|aa'\rangle - \langle d'a'|ad\rangle \cong 2J - K \qquad (1)$$

where $\hat{V}$ is the Hamiltonian, d and d' are the highest occupied and the lowest unoccupied molecular orbitals on donor chromophore involved in the excited state formation. Similarly, a and a' are the highest occupied and the lowest unoccupied molecular orbitals on acceptor chromophore. J is the Coulombic coupling term whereas K is the exchange coupling term which includes ionic configurations and can be regarded as the charge-transfer or polarization character of the state.

Electronically excited state is on the donor chromophore initially, thus the system is in $|D_1A_0\rangle$ state. The hot exciton then relaxes and migrates to an acceptor chromophore, which can be deduced as $|D_0A_1\rangle$ state. The wavefunction for this two level system is $|\psi_i\rangle = c_D\,|D_1A_0\rangle + c_A\,|D_0A_1\rangle$. The eigenvalues can be obtained by solving the equations for the following matrix: [20]

$$\begin{bmatrix} E_D & V \\ V & E_A \end{bmatrix}\begin{bmatrix} c_D \\ c_A \end{bmatrix} = E\begin{bmatrix} c_D \\ c_A \end{bmatrix} \qquad (2)$$

Here, $E_D = E(D_1) - E(D_0)$ and $E_A = E(A_1) - E(A_0)$. For this special case, E_D corresponds to the excitation energy that eventually leads to the formation of hot exciton. The eigenvalues of the secular determinant can be calculated as:

$$E_\pm = \frac{E_D+E_A}{2} \pm \sqrt{\Delta^2 + V^2} \qquad (3)$$

with $\Delta = \frac{E_D-E_A}{2}$. It is important to note that in the strong coupling regime, hot exciton relaxes to the neighboring acceptor sites for which $E_D \cong E_A$ and Δ is quite small in comparison to V. Therefore, the wavefunctions of the coupled states are found to be as:

$$\psi_\pm = \frac{1}{\sqrt{2}}(|D_0A_1\rangle \pm |D_1A_0\rangle) \qquad (4)$$

Since time evolution of coupled donor-acceptor pair is of interest, the time dependent wavefunction can be written as $|\psi(t)\rangle = \hat{U}(t,t_0)|\psi(t_0)\rangle$ and in the basis set of $|\psi_+\rangle$ and $|\psi_-\rangle$ as: [20]

$$|\psi(t)\rangle = c_+e^{-iE_+(t-t_0)/\hbar}|\psi_+\rangle + c_-e^{-iE_-(t-t_0)/\hbar}|\psi_-\rangle \qquad (5)$$

The hot exciton is located on the donor chromophore first, therefore one can easily notice $|\psi(t_0)\rangle = |D_1A_0\rangle$. However, hot exciton moves to acceptor chromophore at time t. To reveal the dynamics of exciton relaxation, it is vital to find the probability of excited state relaxation on acceptor chromophore by calculating the overlap between $|\psi(t)\rangle$ and $|D_0A_1\rangle$. After solving overlap based equations, the probability of occupation on acceptor site and the corresponding rate equation are found as: [20]

$$P_A(t) = |\langle D_0A_1|\psi(t)\rangle|^2 = \frac{|V|^2}{\Delta^2+|V|^2}\sin^2\frac{\sqrt{\Delta^2+|V|^2}t}{\hbar} \qquad (6)$$

$$k_{DA} = \frac{dP_A(t)}{dt} = \frac{|V|^2}{\hbar\sqrt{\Delta^2+|V|^2}}\sin\frac{2\sqrt{\Delta^2+|V|^2}t}{\hbar} \qquad (7)$$

According to Eq. (7), $|V|$ and Δ parameters must be

evaluated in order to calculate the time dependent rate value for hot exciton relaxation. $|V|$ can be estimated by using Eq. (1) for which Coulombic and exchange integrals need to be calculated explicitly. The energy difference between the donor and the acceptor sites, Δ, is quite small; as will be discussed below. Thus, hot exciton for the most part oscillates back and forth between the donor and the acceptor chromophores until total relaxation.

As a model conjugated polymer, a short segment of polythiophene with 20 α-linked fully planar thiophene rings (th20) is chosen for this study. Both ground and excited states geometries are obtained using 3-21G basis set with Hartree-Fock (HF) and spin restricted configuration interactions with single excitations (RCIS) methods, respectively. Excitonic absorption and emission energies were obtained by employing time dependent density functional theory (DFT) with B3LYP functional and 6-31G(d) basis set on HF and RCIS optimized geometries. All calculations were performed with Gaussian 09 software package [21]. 3D transition density plots for the lowest excitonic transitions were constructed by using the formula below: [4, 8]

$$\rho_{\mu 0}(r) = \sum_{h,l} C_{\mu hl} \phi_h \phi_l \quad (8)$$

where $C_{\mu hl}$ is the configuration interaction coefficients of the transition between occupied (ϕ_h) and unoccupied (ϕ_l) molecular orbitals.

The dynamics of relaxation has been carried out with Monte-Carlo methods. Monte-Carlo simulations start at the location where the photoexcitation occurs. Two rates are calculated with Eq. (7), one for self-localizing (k_{self}) exciton (hopping distance = 0 Å) and the other for hopping exciton (k_{hop}) to either the left or right direction of conjugated chain (hopping distance = 3.93 Å, one thiophene unit migration). One of the rates is chosen on the basis of their weighted probabilities for the hopping process. The hopping time is estimated based on the following equation: [22]

$$\tau = \frac{-\ln(rand)}{k_{self} + k_{hop}} \quad (9)$$

where $rand$ is a random number between 0 and 1. The Monte-Carlo simulation runs until the formation of cold exciton. 10,000 Monte-Carlo runs are found to be sufficient to get converged results.

3. Results and Discussion

Hot exciton relaxation mechanism through various potential energy surfaces is illustrated in Figure 1. In the model presented in this work, hot exciton strongly couples with the nearby excited states, which act as acceptor chromophores. Such chromophores have very similar potential energy surfaces and resemble very much initially excited state chromophore with slight deviations in the reaction coordinate. The movements in the reaction coordinate are facilitated by vibronic modes coupled to the excited states. After relaxation of hot exciton to the lowest energy site, a cold exciton forms, which decay to the ground state either radiatively (by emitting photon) or non-radiatively [23]. In order to reveal the dynamics of hot exciton relaxation, one needs to exploit those intermediate excited states and figure out the main vibrational mode(s) that transform hot exciton into cold exciton.

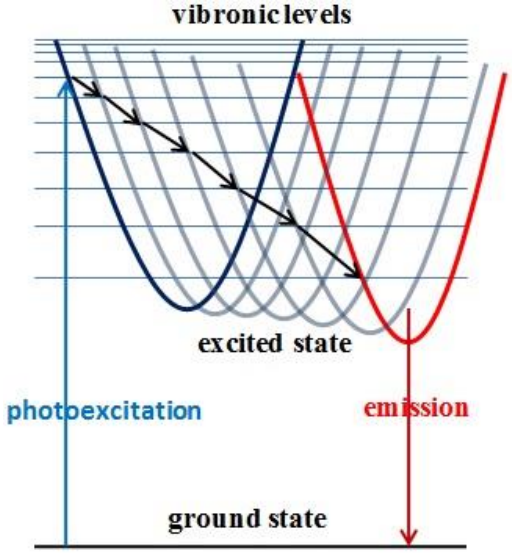

Figure 1. The relaxation mechanism of hot exciton to cold exciton through intermediate excitonic states with the use of vibrational modes.

The size and location of hot and cold excitons can be best visualized by transition density plots [8]. Figure 2 shows that hot exciton on th20 oligomer is much more delocalized than cold exciton, as one might expect. It has been shown in many different studies that relaxation of hot exciton is accompanied by structural changes over the chromophoric unit [8, 11, 24]. The major change in thiophene based systems is lengthening of C=C double bonds while shortening of C-C single bonds along the conjugated backbone. Such structural change is achieved by involvement of C-C stretching modes around 1,600 cm^{-1}. Indeed, C-C stretching modes are the major players of vibrational modes that transform hot exciton into cold exciton in conjugated materials [11]. Therefore, it is assumed that the timescale of motion for this vibrational mode determines the timescales of hot exciton relaxation. In addition, there is experimental evidence that indicates photoexcited states relax in timescales less than 100

femtoseconds (fs), mainly limited by the sensitivity of utilized equipment [10, 12, 25]. The stretching motion at 1,600 cm^{-1} is completed at 30 fs. Half of the periodic motion should, in principal, give adequate room for hot exciton to structurally convert into cold exciton in a perfectly planar system that does not possess any kind of defects, kinks, torsional degrees of freedom, and possible interchromophoric migration sites for exciton hopping.

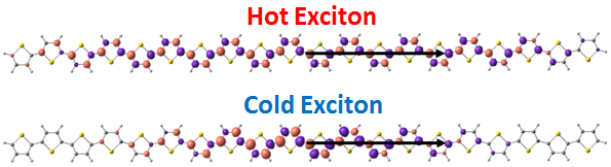

Figure 2. 3D transition density plots (isovalue surface: 0.0004 au) of hot exciton and cold exciton on th20 oligomer. Blue color represents negative and red color represents positive transition density coefficients. Black arrows show the direction of transition dipole moments.

The minimum energy required for formation of hot exciton is 2.09 eV, according to time dependent DFT calculations (Table 1). Vibrationally coupled relaxation of hot exciton yields cold exciton, which has emission energy of 1.70 eV. The symmetries of both transitions are the same and both transitions are mostly dominated by HOMO to LUMO transitions. It is important to note that the calculated transition energies are very similar to those of poly(3-hexylthiophene), implying the accuracy of calculations in predicting polymeric properties from relatively large oligomer derivatives [26]. The Stokes shift, 0.39 eV, is the energy hot exciton loses via vibronic modes through relaxation.

Table 1. Photoexcitation / emission transition energies, involved molecular orbitals, transition dipole moments (μ), oscillator strengths (f), and symmetry of transitions are given below.

structure	transition (eV)	orbital transitions	μ (D)	f (a.u.)	symmetry
hot exciton	2.09 ($S_0 \rightarrow S_1$)	H - 2 → L + 2 (4%) H - 1 → L + 1 (24%) H → L (72%)	11.40	6.66	^1B_u
cold exciton	1.70 ($S_1 \rightarrow S_0$)	H - 1 → L + 1 (5%) H → L (95%)	11.85	5.83	^1B_u

Table 2 lists the calculated J and K coupling integrals for hot exciton relaxing to various acceptor sites. The relative dielectric constant of the medium in the relevant integral calculations is assumed to be 3, which is a typical number for organic semiconductor thin films [22]. In small molecules, hot exciton is expected to relax to its own location due to presence of well delocalized wavefunctions that cover the whole molecule. However, in supramolecular materials such as in conjugated polymers, the excitons might find an opportunity to move extra dimensions due to available sites for exciton migration. Such migration is well-known and experimentally measured for relaxed excitons (cold excitons) in the weak coupling regime. Cold excitons in conjugated polymers can diffuse an average of 10 nm before decaying either radiatively or non-radiatively [17]. Nonetheless, the effect of hot exciton relaxation on exciton diffusion is neglected or unknown for two major reasons. One of them is the experimental difficulties in working on the timescales of such dynamics due to very fast relaxation of hot excitons over the photoexcited chromophore as mentioned above. The second reason is due to fact that excitons are neutral quasiparticles and they are hard to observe experimentally and therefore their dynamics can only be investigated using indirect methods. Therefore, hot excitons might cover some distances before relaxing into a cold exciton and such possible migration needs to be studied in the simulation methods.

Table 2. The magnitude of *J* and *K* coupling integrals for hot exciton relaxation to various acceptor sites for relative dielectric constant of 3.

Donor / Acceptor	*J* (eV)	*K* (eV)	|V| (eV)	Covered Distance (Å)
hot exciton / hot exciton	1.69	41.59	38.21	0
hot exciton / shifted hot exciton	-1.55	-11.63	8.53	3.94
hot exciton / shifted cold exciton	-1.47	-15.60	12.66	3.93
cold exciton / cold exciton	2.97	38.76	32.82	0
cold exciton / shifted cold exciton	-2.75	-21.89	16.39	3.92

Two possible cases are considered for hot exciton relaxation during simulations. In the first case, exciton relaxes at the location it is formed and therefore the center of transition density does not move. In the second case, exciton can move to the nearest acceptor site along the chain. For polythiophene chain, this can be thought of shifting of transition density coefficients one thiophene unit along the conjugated backbone as long as the

symmetry and phase of the electronically excited state is preserved.

The donor / acceptor pairs for excitonic motion are listed in Table 2 along with the calculated coupling integrals. Hot exciton gradually decreases in size and transforms into cold exciton; therefore, hot exciton / hot exciton coupling integrals have initially been used to calculate the rate between the donor and the acceptor for exciton relaxing at its initial position. One will notice that Coulombic coupling integral (1.69 eV) is much smaller than the exchange coupling integral value (41.59 eV). All these calculated coupling integrals are quite large numbers in comparison to the electronic coupling integrals used in the weak coupling regime [27]. The reason stems from the fact that there is huge overlap between the wavefunctions of the donor and the acceptor sites. Consequently, much strong coupling integrals emerge from the calculations. It is important to note that exchange correlations are much stronger than Coulombic interactions and relaxation of hot exciton to low energy sites are driven by exchange mechanism. This observation is valid for all the donor / acceptor pairs studied in this work.

In the presented model, many intermediate excitonic transition densities participate in the gradual formation of cold exciton. The basis of such assignment will be further discussed below. As those intermediate excitonic states lose energy, cold exciton / cold exciton coupling integral becomes the last coupling integral that has to be included in the simulation in the strong coupling regime. After formation of cold exciton, intermediate or weak coupling regimes prevail in the migration of exciton to the other sites [9].

The gradual decrease in the value of electronic coupling element from hot exciton / hot exciton pair into cold exciton / cold exciton pair has been taken as a guide to simulate the time dependent hot exciton cooling rate according to Eq. (7). Afterwards, the probability of exciton occupying acceptor site is estimated according to Eq. (6). The upper panel in Figure 3 shows the rate dependence as a function of time. Since the rate equation has sine function, one also gets negative rate, which corresponds to back exciton transfer to donor site. Therefore, the absolute value of the rate for exciton relaxation has been used in the relevant graph in Figure 3. The average rate for each oscillation has been found as 3.75×10^{15} s^{-1}, which is much faster than typical rate constants predicted for incoherent motion of cold excitons in the weak coupling regime. The time step for exciton motion between intermediate excitonic states (see Figure 1) is predicted to be ~0.3 fs. This is rather short due to the extremely fast relaxation dynamics. $P_A(t)$ values in Figure 3 shows that while exciton relaxing, it can occupy both donor and acceptor site with almost similar probability. That is, hot exciton oscillates back and forth between donor and acceptor chromophores at ultrafast speeds. Due to very short time steps involved, the hot exciton gradually visits many intermediate excitonic states before forming cold exciton. That is why many intermediate states are needed to explain the relaxation dynamics in conjugated materials. As hot exciton relaxes to lower energy excitonic states, the magnitude of $|V|$ has been predicted to quadratically decrease (due to typical parabolic shape of potential energy surface) after each hop until cold exciton forms along the backbone.

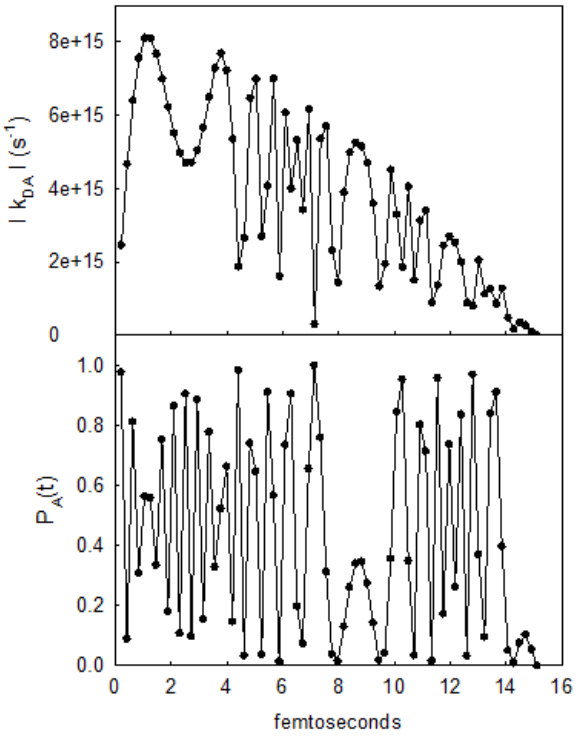

Figure 3. The time dependent rate values for hot exciton relaxation in the strong coupling regime (upper panel) and the occupation probability of acceptor site (lower panel).

In the simulation, $|V|$ has been found to be much larger than Δ, which is estimated as 0.39 eV divided by the number of hops between the donor and the acceptor sites. Due to extremely large electronic coupling integrals involved, exciting the polythiophene chain at the band edge or at higher energies would not yield very different hot exciton relaxation dynamics based on the model presented here. Indeed, Banerji et al. showed that the initial anisotropy decay profile for hot exciton relaxation is independent of chosen excitation wavelength in PCDTBT samples, supporting the conclusions given in this work [12].

Since conjugated polymers can be viewed as multi-chromophoric systems with varying sizes, then there is room for exciton hop to the nearest acceptor sites and this

diffusion must be accounted for proper evaluation of hot exciton dynamics. If one assumes that hot exciton hops to the nearest site instead of localizing at its initial location, then $|V|$ is calculated as 8.53 eV (Table 2). From Eq. (7), one can estimate that the initial rate is six times faster when hot exciton relaxes at the original position (k_{self}) than jumping to the next chromophore (k_{hop}). In addition, when exciton starts hopping from one site to another, the geometrically relaxed exciton needs certain amount of energy for each hop [24]. Such energy loss for each excitonic hop limits the number of hops and hence distance an exciton can travel along the chain. Keeping all these considerations at hand, a Monte-Carlo simulation has been carried out for hot exciton formed by band edge excitation. Figure 4 shows the histogram plot of 10,000 exciton hopping trajectories on polythiophene chain. It is clear that hot exciton relaxes at its current position most of the time but can also travel distances as long as 2 nm. However, the root-mean-squared displacement of exciton hopping is calculated as 0.41 nm, corresponding to roughly one unit thiophene shift of the center of transition density within the duration of relaxation in the strong coupling regime. Thus, one can easily conclude that hot excitons can also migrate to some extent over the chain during the relaxation process.

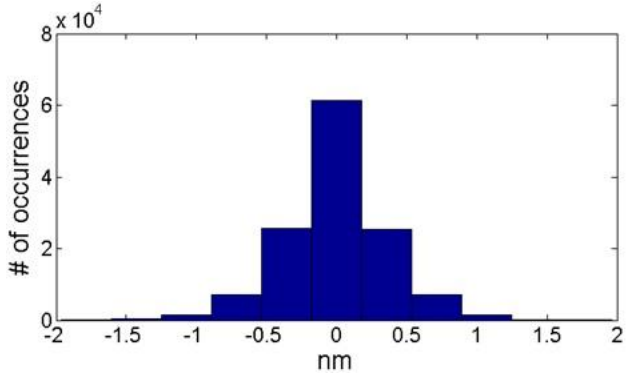

Figure 4. The histogram plot of hot exciton migration trajectories on conjugated polymer chain with band edge excitation after 10,000 Monte-Carlo runs.

4. Conclusions

In this work, hot exciton relaxation dynamics is studied for a conjugated polymer chain. Hot exciton on a perfectly linear polymer polythiophene chain relaxes at femtosecond time scale with the aid of vibrational modes, in accordance with experimental observations. During relaxation, hot exciton oscillates between the donor and the acceptor site until it cools down. Exchange coupling integrals dominate the total electronic coupling integral with only limited contribution coming from Coulombic interactions between the donor and the acceptors sites. Presented model predicts that it is possible for hot exciton to gain same mobility along the conjugated backbone over polythiophene chain during relaxation. Nonetheless, the extent of such mobility might differ from one conjugated polymer to another and more research is needed to unravel the dynamics of hot exciton migration among various types of conjugated materials.

Declaration of Ethical Standards

The authors of this article declare that the materials and methods used in this study do not require ethical committee permission and/or legal-special permission.

Conflict of Interest

The authors declare that they have no known competing financial interests or personal relationships that could have appeared to influence the work reported in this paper.

Acknowledgments

This work was supported by a grant from The Scientific and Technical Research Council of Turkey (TUBITAK, Project No: 120Z662).

References

[1] Scholes G.D., 2003. Long-range resonance energy transfer in molecular systems. Annual Review of Physical Chemistry, **54**, pp. 57-87.

[2] Collini E., Scholes G.D., 2009. Coherent Intrachain Energy Migration in a Conjugated Polymer at Room Temperature. Science, **323**(5912), pp. 369-373.

[3] Spano F.C., Clark J., Silva C., Friend R.H., 2009. Determining exciton coherence from the photoluminescence spectral line shape in poly(3-hexylthiophene) thin films. Journal of Chemical Physics, **130**(7), no. 074904.

[4] Kose M.E., Graf P., Kopidakis N., Shaheen S.E., Kim K., Rumbles G., 2009. Exciton Migration in Conjugated Dendrimers: A Joint Experimental and Theoretical Study. ChemPhysChem, **10**(18), pp. 3285-3294.

[5] Traub M.C., Lakhwani G., Bolinger J.C., Vanden Bout D., Barbara P.F., 2011. Electronic Energy Transfer in Highly Aligned MEH-PPV Single Chains. Journal of Physical Chemistry B, **115**(33), pp. 9941-9947.

[6] Hestand N.J., Spano F.C., 2018. Expanded Theory of H- and J-Molecular Aggregates: The Effects of Vibronic Coupling and Intermolecular Charge Transfer. Chemical Reviews, **118**(15), pp. 7069-7163.

[7] Duan H-G., Nalbach P., Prokhorenko V.I., Mukamel S., Thorwart M., 2015. On the origin of oscillations in two-dimensional spectra of excitonically-coupled molecular systems. New Journal of Physics, **17**(7), no. 072002.

[8] Kose M.E., Mitchell W.J., Kopidakis N., Chang C.H., Shaheen S.E., Kim K., Rumbles G., 2007. Theoretical Studies on Conjugated Phenyl-Cored Thiophene Dendrimers for Photovoltaic Applications. Journal of the American Chemical Society, **129**(46), pp. 14257-14270.

[9] Hwang I., Scholes G.D., 2011. Electronic Energy Transfer and Quantum-Coherence in pi-Conjugated Polymers. Chemistry of Materials, **23**(3), pp. 610-620.

[10] Maimaris M., Pettipher A.J., Azzouzi M., Walke D.J., Zheng X.J., Gorodetsky A., Dong Y.F., Tuladhar P.S., Crespo H., Nelson J., Tisch J.W.G., Bakulin A.A., 2022. Sub-10-fs observation of bound exciton formation in organic optoelectronic devices. Nature Communications, **13**(1): no. 4949.

[11] Garratt D., Misiekis L., Wood D., Larsen E.W., Matthews M., Alexander O., Ye P., Jarosch S., Ferchaud C., Struber C., Johnson A.S., Bakulin A.A., Penfold T.J., Marangos J.P., 2022. Direct observation of ultrafast exciton localization in an organic semiconductor with soft X-ray transient absorption spectroscopy. Nature Communications, **13**(1), no. 3414.

[12] Banerji N., Cowan S., Leclerc M., Vauthey E., Heeger A.J., 2010. Exciton Formation, Relaxation, and Decay in PCDTBT. Journal of the American Chemical Society, **132**(49), pp. 17459-17470.

[13] Rohr M.I.S., Marciniak H., Hoche J., Schreck M.H., Ceymann H., Mitric R., Lambert C., 2018. Exciton Dynamics from Strong to Weak Coupling Limit Illustrated on a Series of Squaraine Dimers. Journal of Physical Chemistry C, **122**(15), pp. 8082-8093.

[14] Zhang Y.S., Shi H.Y., Luo J.T., Shen J.G., Li S., George T.F., 2021. Lattice Vibrations and Time-Dependent Evolution of Local Phonon Modes during Exciton Formation in Conjugated Polymeric Molecules. Polymers, **13**(11), no. 1724.

[15] Perez I.G., Barford W., 2021. Ultrafast Fluorescence Depolarization in Conjugated Polymers. Journal of Physical Chemistry Letters, **12**(22), pp. 5344-5348.

[16] Hennebicq E., Pourtois G., Scholes G.D., Herz L.M., Russell D.M., Silva C., Setayesh S., Grimsdale A.C., Mullen K., Bredas J.L., Beljonne D., 2005. Exciton migration in rigid-rod conjugated polymers: An improved Forster model. Journal of the American Chemical Society, **127**(13), pp. 4744-4762.

[17] Bjorgaard J.A., Kose M.E., 2015. Simulations of singlet exciton diffusion in organic semiconductors: a review. Rsc Advances, **5**(11), pp. 8432-8445.

[18] You Z.Q., Hsu C.P., 2014. Theory and Calculation for the Electronic Coupling in Excitation Energy Transfer. International Journal of Quantum Chemistry, **114**(2), pp. 102-115.

[19] Harcourt R.D., Scholes G.D., Ghiggino K.P., 1994. Rate Expressions for Excitation Transfer. II. Electronic Considerations of Direct and through-Configuration Exciton Resonance Interactions. Journal of Chemical Physics, **101**(12), pp. 10521-10525.

[20] Cohen-Tannoudji C., Diu B., Laloe F., 1977. Quantum Mechanics, 1st ed., John Wiley and Sons, Paris, France.

[21] Frisch M.J., Trucks G.W., Schlegel H.B., Scuseria G.E., Robb M.A., Cheeseman J.R., Scalmani G., Barone V., Mennucci B., Petersson G.A., Nakatsuji H., Caricato M., Li X., Hratchian H.P., Izmaylov A.F., Bloino J., Zheng G., Sonnenberg J.L., Hada M., Ehara M., Toyota K., Fukuda R., Hasegawa J., Ishida M., Nakajima T., Honda Y., Kitao O., Nakai H., Vreven T., Montgomery J.A., Peralta J.E., Ogliaro F., Bearpark M., Heyd J.J., Brothers E., Kudin K.N., Staroverov V.N., Kobayashi R., Normand J., Raghavachari K., Rendell A., Burant J.C., Iyengar S.S., Tomasi J., Cossi M., Rega N., Millam J.M., Klene M., Knox J.E., Cross J. B., Bakken V., Adamo C., Jaramillo J., Gomperts R., Stratmann R.E., Yazyev O., Austin A.J., Cammi R., Pomelli C., Ochterski J.W., Martin R.L., Morokuma K., Zakrzewski V.G., Voth G.A., Salvador P., Dannenberg J.J., Dapprich S., Daniels A.D., Farkas O., Foresman J.B., Ortiz J.V., Cioslowski J., Fox D.J., 2009. Gaussian 09, Revision B.01, Gaussian, Inc., Wallingford, CT.

[22] Kose M.E., Long H., Kim K., Graf P., Ginley D., 2010. Charge Transport Simulations in Conjugated Dendrimers. Journal of Physical Chemistry A, **114**(12), pp. 4388-4393.

[23] Dimitrov S., Schroeder B., Nielsen C., Bronstein H., Fei Z., McCulloch I., Heeney M., Durrant J., 2016. Singlet Exciton Lifetimes in Conjugated Polymer Films for Organic Solar Cells. Polymers, **8**(1), no. 14.

[24] Kose M.E., 2011. An activated scheme for resonance energy transfer in conjugated materials. Journal of Chemical Physics, **135**(24), no. 244512.

[25] Wells N.P., Boudouris B.W., Hillmyer M.A., Blank D.A., 2007. Intramolecular exciton relaxation and migration dynamics in poly(3-hexylthiophene). Journal of Physical Chemistry C, **111**(42), pp. 15404-15414.

[26] Gierschner J., Cornil J., Egelhaaf H.J., 2007. Optical bandgaps of pi-conjugated organic materials at the polymer limit: Experiment and theory. Advanced Materials, **19**(2), pp. 173-191.

[27] Kose M.E., 2011. Evaluation of Excitonic Coupling and Charge Transport Integrals in P3HT Nanocrystal. Journal of Physical Chemistry C, **115**(26), pp. 13076-13082.

Koc. J. Sci. Eng., 7(1): (2024) 9-19 https://doi.org/10.34088/kojose.1115308

Kocaeli University

Kocaeli Journal of Science and Engineering

http://dergipark.org.tr/kojose

Breakdown Voltage Estimation in Transformer Oils with Low-Cost Humidity Sensor

Doruk GÜNEŞ [1,*], Hüsnügül TEKİN [2], Bora ALBOYACI [3], Özgür YILMAZ [4]

[1] *GENETEK Ltd. Şti., Kocaeli, 41170, Turkey,* ***ORCID:*** *0000-0002-7204-3769*
[2] *Dicle Elektrik Dağıtım A.Ş., Diyarbakır, 21070, Turkey,* ***ORCID:*** *0000-0002-9817-9373*
[3] *Department of Electrical Engineering, Kocaeli University, Kocaeli, 41001, Turkey,* ***ORCID:*** *0000-0002-1117-0326*
[4] *Dicle Elektrik Dağıtım A.Ş., Diyarbakır, 21070, Turkey,* ***ORCID:*** *0000-0003-0972-0226*

Article Info

Research paper

Received : *May 13, 2022*
Accepted : *March 14, 2023*

Keywords

Breakdown Voltage
Humidity Sensor
Moisture in Oil
Relative Saturation
Water activity
Water Content

Abstract

The relative humidity and temperature of the oil used for insulation purposes in transformers directly affect the breakdown voltage of the oil and accordingly the life of the transformer. Continuous monitoring of the moisture content and breakdown voltage of the transformer oil provides the basis for predictive maintenance practices. This study aims to develop a sensor to continuously monitor the moisture content of the insulating oil and to calculate the breakdown voltage approximately. In this context, firstly, measurements were taken with an industrial oil monitoring sensor which calculates the breakdown voltage in transformer oils with high accuracy and was verified with laboratory measurements. At the same time, EE364 by E+E™ and SHT10 by Sensirion™ also used for temperature and humidity measurements. By comparing the measured data with each other, a relationship was formulated between the humidity and temperature values and the breakdown voltage. As a result, an approximate breakdown voltage calculation method that can be used considering the characteristic parameters of transformer oil has been introduced. Thus, a cost-effective function has been developed that can be widely used for transformer monitoring systems.

1. Introduction

Transformers are one of the most critical elements of the grid. It has become a necessity today to carry out predictive maintenance practices and health index studies on transformers in order to have high network reliability and low SAIDI and SAIFI indices[1]. According to the results of the Cigré 642 document, approximately 36% of the faults that occur in transformers are due to dielectric faults. [2]. When the root causes of the faults are examined, it is seen that 12% of them are due to aging. It can be said that one of the most important factors that accelerate aging in transformers is humidity. In transformers, approximately 98% of the moisture is in the cellulosic insulation paper and 2% is in the transformer oil, and this ratio varies depending on the loading[3]. The amount of moisture in the transformer and the location of the humidity change depending on parameters such as the ambient temperature of the transformer, the load curve, and the amount of load. With the increase in humidity in the transformer, the depolymerization rate of the cellulosic paper increases and the aging rate of the transformer also increases[4]. In addition, with the increase of moisture content in the oil, the breakdown voltage of the oil decreases and fault risk increases. [5].

The breakdown voltage in transformer oils varies according to the relative humidity or water content (wc) in the oil. These parameters differ depending on the temperature. On the other hand, due to the hysteresis feature of the balance between cellulosic paper and transformer oil, different relative humidity values can be seen at the same temperature values. Therefore, it is important to understand the dynamics of moisture content in transformer oil. Once the related concepts are understood, it is possible to switch from relative humidity to breakdown voltage data. In this context, to calculate the breakdown voltage in oils, the relationship between the

* Corresponding Author: doruk.gunes@genetek.com.tr

relative humidity parameter and the breakdown voltage should be considered.

In the literature, there are many studies carried out to characterize dielectric liquids and express their different properties with equations. Although breakdown events are likened to gases and solids in different aspects of liquids, in general, the approaches and equations created for gases or solids are not valid for liquids. At present, the breakdown voltage of dielectric fluids (insulating oils) used in transformers to provide insulation and help cooling is determined based on the values measured as a result of the tests performed in the laboratory. However, it is of great importance to prevent possible failures for transformers, which are constantly in operation and are one of the key equipment of a reliable network structure.

In the literature, there are projects in which the concepts of water content, relative humidity, and breakdown voltage in transformer oils are examined and various studies are carried out. In [6], the elements used as the insulation material of the transformer and the necessary terms are explained and the balance between the water content in the cellulosic paper and insulating oil is explained according to the curves and different references. In [7], the effect of the water content in the transformer oil on the breakdown voltage is examined. [8] explains the relationship between the water content in transformer oil and the relative humidity. In this context, the types of water content that can be found in transformer oil, concepts such as solubility and relative humidity, the relationship between relative humidity and water content and breakdown voltage are explained. In [9], the movement of the water content in the insulation system of the transformer between the cellulosic insulation material and the insulation oil was investigated. The relative humidity and water content values that change depending on the temperature are explained through graphics and the hysteresis movement of the water content depending on the temperature is explained.

In [10], the relationship between water content, humidity and temperature in transformer oils is examined with online sensors. Accordingly, measurements were taken with different parameters in different oils and the results were compared. In [11], the structure of a sensor developed to monitor the breakdown voltage of insulating oil in transformers online and continuously is examined. In [12], the variation of relative humidity and water content in transformer oil is examined according to temperature. As a result of the tests carried out, it is said that the flow rate of the oil affects the relative humidity value. In [13], the breakdown voltage of different oil types and their water content at this voltage are compared. In addition, the viscosity values at different temperatures and the relative electrical conductivity values at different water contents are compared. In [14], hysteresis curves for temperature-water content of different humidity sensors are compared. In addition, water content curves are shown according to the temperature of different types of transformer oils.

In [15], the water contents of four different transformer oils, which contain both used and new oils of the same brand, are examined according to the relative humidity values of thirty-five degrees. In [16], mineral and natural ester oils used in transformers are compared. While making this comparison, events such as the water content value formed according to the temperature, the water balance between the cellulosic insulation paper and the oil, the water content in the oil and the change of the water content in the cellulosic insulation paper with time were examined. In order to make these examinations, dynamic models were created and simulations were carried out.

In [17], the breakdown voltage of transformer oil is compared according to relative humidity and temperature values. In [18], the water content values corresponding to the relative humidity values of mineral, natural ester and synthetic ester oils used in transformers were investigated. In addition, the analyzed oils were dried online and their water content removal performances were evaluated. In [19,20], health index studies were carried out in which the breakdown voltage and the water content in the oil were also evaluated.

In this study, we aimed to realize the approaches for calculating the breakdown voltage for oils over the measured values of temperature and humidity parameters and to create the product design. In this context, measurements were carried out using a datalogger and web interface structure with a commercial brand of breakdown voltage sensor (Trafostick™), which is sold for high accuracy calculation of the breakdown voltage in transformers, and after the breakdown voltage and relative humidity content were taken as data, it was verified with laboratory measurements. Then, the breakdown voltage calculated according to the moisture content output by the Trafostick™ equipment was graphically plotted and a curve suitable for the graph was created. E+E™ 364 model sensor, which is also another trademark, only gives the relative humidity and temperature value to the user. Measurements were also taken with this sensor, and the relative humidity content taken from the Trafostick™ sensor and the relative humidity content, which is the output of the E+E™ sensor, were compared and verified each other. According to the relative humidity-breakdown voltage graph found from the output of the transformer sensor, the breakdown voltage was obtained from the relative humidity data of the E+E™ sensor. Then, measurements were taken with a single sensor named Sensirion that only gives relative humidity, the results were verified with the E+E™ sensor and the breakdown voltage

was calculated. In this context, it is seen that the breakdown voltage value calculated with the help of a single humidity sensor is close to the rupture voltage value given by a commercial brand. Although there are no definitely true results in applications such as transformer stick or oil test, a suitable single sensor application has been carried out for the application of trend analysis approach in small power transformers.

2. Relationship Between Humidity and Breakdown Voltage

For the reliability and sustainability of transformers, the relationship between transformer oil and moisture should be well understood. The humidity in the transformer oil affects the breakdown voltage of the oil depending on various parameters. Moisture content in transformer oil can be in different phases. These can be listed as the bonding of dissolved water to the hydrocarbon molecules that make up the oil with hydrogen, the emulsified water being supersaturated in solution but not yet completely separated from the oil, being supersaturated in the free water solution and having a high concentration to form water droplets and separate from the oil.[8].

The moisture that can be dissolved in the transformer oil changes depending on the temperature, and accordingly, the breakdown voltage also changes depending on the temperature. While calculating the breakdown voltage in transformer oil, both the relative humidity value and the water content value can be used.

To calculate the relative humidity value, the maximum solubility values of the environment where the sensor is located must be known. This value changes depending on the temperature.

For liquids, the relative humidity is shown in terms of water activity (aw). When calculating the relative humidity, the calculated value (P) is written in the numerator and the maximum value (P_0) that the environment can solve at the current temperature value in the denominator Eq. (1).

$$a_w = 100x\frac{P}{P_0} \tag{1}$$

In order to calculate the water content, the maximum solubility (S_0) at the relevant temperature must be calculated first. In the literature, the following formula is used to calculate the solubility [8] Eq.(2).

$$logS_0 = \frac{A}{C+273} + B \tag{2}$$

The coefficients A and B in the equation are the characteristic information of the oil. A and B parameters for transformer oils were accepted as -1663.30 and 7.37, respectively. 'C' is the temperature value in Celsius. When the values are substituted in the equation, the solubility value for the relevant temperature can be calculated. The relative saturation (RS) value is the amount of water measured in the oil according to the solubility level at the relevant temperature. That is, the value given as a percentage is the ratio of water content to solubility (S_0) [8] Eq.(4).

$$RS = \frac{w_c}{S_0} \tag{3}$$

When the formulas are simplified.

$$w_c = RSx10^{\left(\frac{A}{Temperature+273}+B\right)} \tag{4}$$

It appears that the relationship between the breakdown voltage of the oil and the relative humidity is more linear than that of the water content. Due to the time constants between the transformer oil and the cellulosic insulation paper, the moisture content of the oil may differ at the same temperatures. This is related to the hysteresis behavior of the isolation system. This phenomenon is shown in the following sections of the article together with the measurement results.

3. Material and Methods

3.1. Introduction of Sensors

Capacitive humidity sensors are generally used in industrial temperature and humidity measurement products. Figure 1 shows the geometric structure of the capacitive sensor.

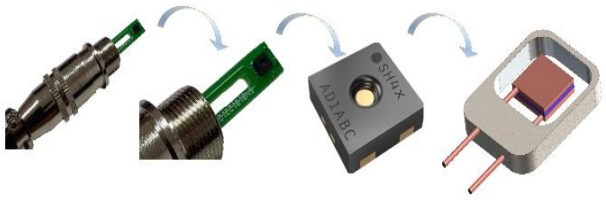

Figure 1. Geometric structure of industrial capacitive humidity sensor

In this study, three different sensors were used to measure the humidity in transformer oil. The first of these is an industrial sensor called Trafostick™, which has been produced as a transformer oil monitoring sensor. Trafostick™ measures and calculates the breakdown voltage, relative humidity, water content and temperature

of the transformer oil. While calculating these values, it shows the results as the average of certain sampling intervals as well as the instantaneous calculations. While the Trafostick™ product was being designed, the breakdown voltages obtained from the laboratory results were evaluated in order to calculate the breakdown voltage according to the measured relative humidity value. Accordingly, tests were carried out by taking 3800 oil samples from more than 900 transformers.[21]. In this context, it can be said that the Trafostick™ sensor calculates the breakdown voltage with high accuracy. The other sensor used is the sensor named E+E364. This sensor is a compact temperature and humidity sensor used for measuring the relative humidity and temperature in oils. The sensor provides the relative humidity and temperature information of the oil to the user [22].

The last sensor used in the study is a single sensor named Sensirion SHT10. This sensor is designed for use in the air environment and only gives the temperature and relative humidity information to the user.[23]. In this study, the sensor named Sensirion SHT10 was used to measure the relative humidity of transformer oil, and the results were compared in detail with the results of other sensors. Three-dimensional CAD models of Trafostick™, E+E™364 and Sensirion SH10 products are shown in Figure 2 (a), (b) and (c), respectively. In addition, the capacitive sensor shown in Figure 1 is the Sensirion product. The sensor visible when the brass coating on the front of the structure shown in Figure-2 (c) is removed is shown in Figure 1.

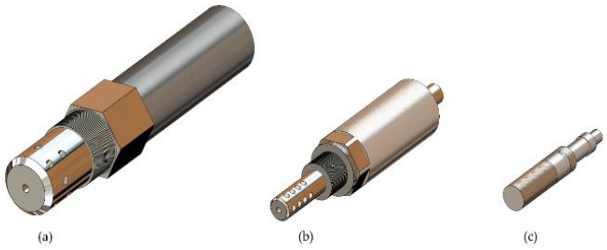

Figure 2. 3D CAD models of humidity-temperature sensors used in the project (a) Trafostick™ (b) E+E™364 (c) Sensirion SHT10.

3.2. Installation of Sensors on the Transformer

When the devices are mounted on the transformer, the oil must be in contact with the sensors. In this context, a suitable place should be determined in the transformer tank. Due to the radiator positions of the transformer, the upper part of the tank is usually more suitable. For the mounting process of the sensors, a suitable hole is drilled in the relevant location and a rod adapter is welded there. Then the sensors are mounted on the rod adapter. In Figure 3, the position of the Transformer and E+E364 sensors on the transformer tank is shown in the three-dimensional CAD model.

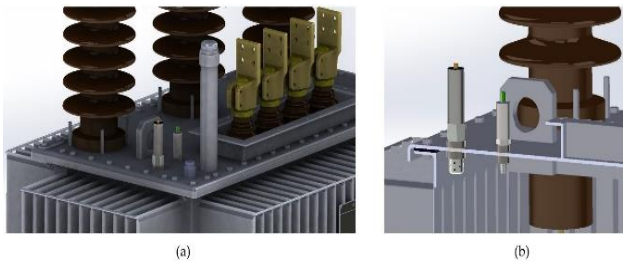

Figure 3. 3D CAD model of Transfostick and E+E364 sensor mounted on transformer tank.

3.3. Introduction of the Web Interface

The sensors used give raw data output with MODBUS. A parameter is defined for each address used in the sensors. To retrieve data, there must be a datalogger communicating over the MODBUS protocol. Within the scope of the project, a data logger was designed and manufactured to communicate with the sensors. The designed datalogger (named PDA Gateway) has one Ethernet port, one USB port for network operators to connect wireless internet providers, an RS485 connection port, and sensor connection inputs.

Sensors can be used on transformers located in areas where continuous site visits and data acquisition are not possible. In this context, the product called PDA Gateway can upload raw sensor data to a server via cellular or serial internet connection. USB-type cellular modem of mobile network service providers is used for internet connection. On the developed web-based user interface, measurement data can be plotted instantly and historical data can be downloaded in ".csv" format. In this way, it is possible to make trend analysis according to daily, monthly and even annual measurement data. [24].

4. Results and Discussion

4.1. Heating Analysis Tests

First, the heating analysis tests were carried out in the distribution company on the 400 kVA transformer where the Trafostick™ and E+E364 sensors were mounted. While performing these tests, both the data obtained from the sensors were examined and the breakdown voltage tests were carried out simultaneously. The field view of the sensors mounted on the transformer is shown in Figure 4.

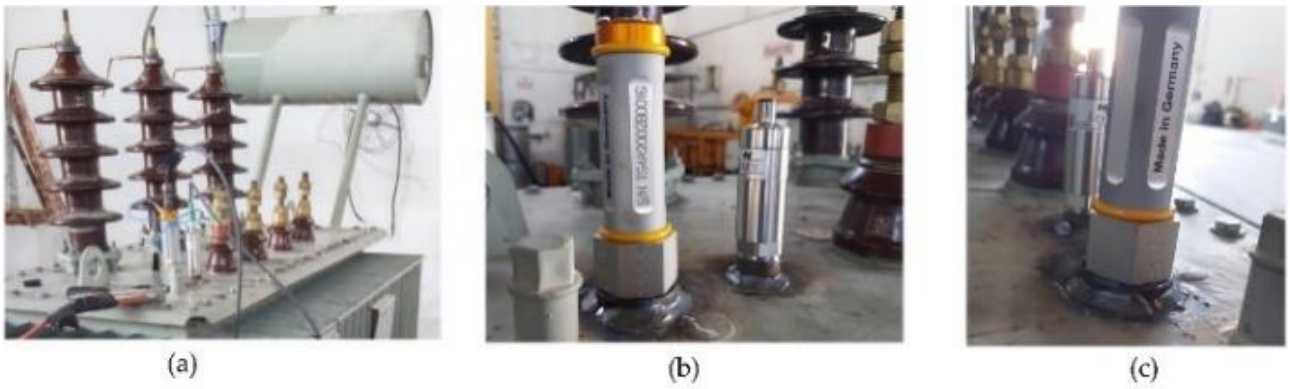

Figure 4. Views of the Trafostick™ and E+E™ sensors mounted on the transformer in the distribution company for heating tests.

The purpose of the heating tests is to compare the breakdown voltage data given by the Trafostick™ sensor with the test results and evaluate its accuracy. In addition, it has been determined to constantly monitor the breakdown voltage and relative humidity, establish a relationship between them and use this relationship in E+E364 and Sensirion sensors. In this context, five different heating tests were carried out. The start and end dates of the heating tests performed are shown in Table 1.

At the beginning and end of the heating tests, oil samples were taken from the transformer tank and tests were carried out in accordance with the IEC 60156:2018 standard. [25]. Tests were carried out with a Multi-Tech MTH-OBDV-80 device.

Table 1. Start and end dates of heating tests.

Test adı	Start date	End date
First oil test	23.11.2020 17:32	24.11.2020 08:06
Second oil test	26.11.2020 09:46	27.11.2020 10:09
Third oil test	01.12.2020 19:38	02.12.2020 10:32
Forth oil test	03.12.2020 19:51	04.12.2020 10:21
Fifth oil test	07.12.2020 23:56	08.12.2020 10:58

As a result of five different heating tests, the data of the Trafostick™ sensor was examined and compared with the data of the test device. In Figure 5 the temperature, relative humidity and breakdown voltage values given by the Trafostick™ sensor as a result of the third heating test are shown.

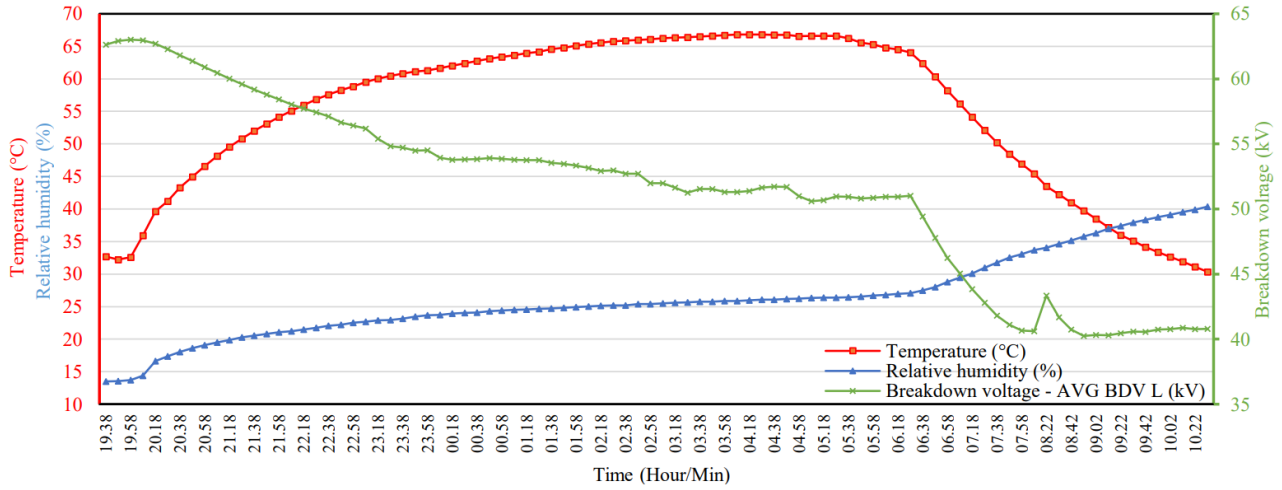

Figure 5. Temperature, humidity and breakdown voltage values measured by the Trafostick™ sensor during the heating tests (for the 3rd heating test)

As can be seen from the third test result, the oil temperature rises from about 32 ºC degrees to 67 ºC degrees in the heating test. It can be said that the relative humidity increased from approximately 13% to 27% during this period. As the transformer heats up, the moisture contained in the cellulosic paper passes into the oil. As the temperature increases, the maximum amount of water that can be dissolved by the oil increases, so the increased rate of relative humidity in this range is less compared to the cooling period. As the transformer cools, the maximum amount of moisture that the oil can dissolve decreases. On the other hand, the rate of return of the water content in the oil back to the cellulose paper is less than the cooling rate of the oil. For this reason, it can be seen from

the graph that the relative humidity value increases while the transformer cools down. As a result, it can be said that there is a dynamic hysteresis loop between the transformer oil and the water content in the cellulosic insulation paper. Heating tests are insufficient to clearly see the hysteresis curve, however, the hysteresis curve formed according to the results obtained from long-term measurements is shown in Figure 6.

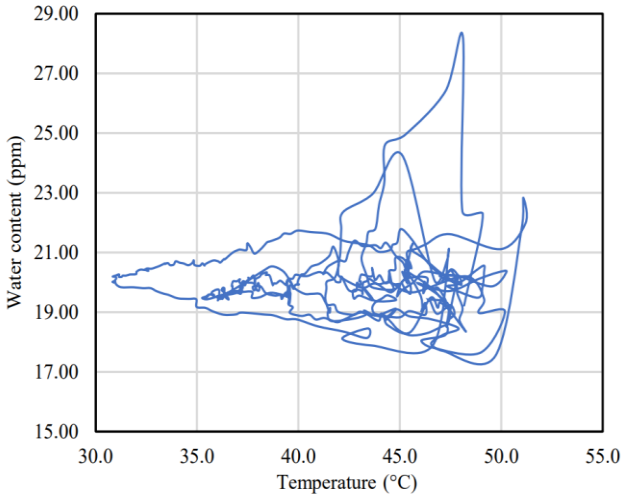

Figure 6. Hysteresis curve created according to the measurement results

The superimposed version of the temperature and humidity values measured during each test is shared in Figure 7.

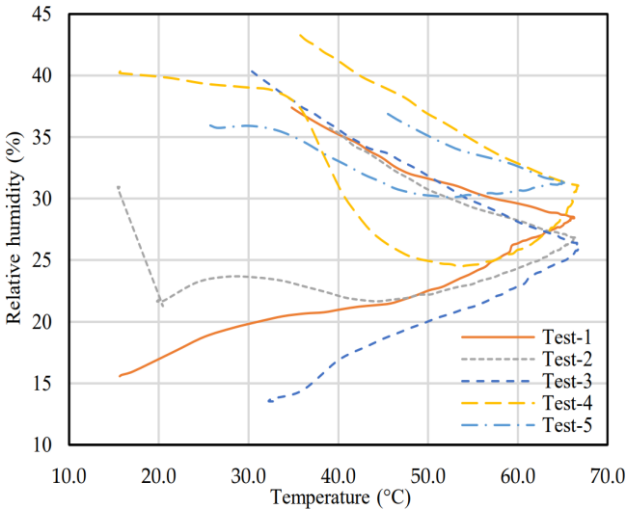

Figure 7. Temperature-humidity curve for each test

As a result of the five tests performed, the results of the test for breakdown voltage and the Trafostick™ sensor are shown in Table 2. According to the IEC 60422:2013 standard, a breakdown voltage between 30 kV and 40 kV is defined as normal, above 40 kV as good, and below 30 kV as bad.[26].

Table 2. Comparison of the breakdown voltages found by the Trafostick™ and breakdown voltage tester as a result of the heating tests carried out

Oil sample	Samples Taken	Oil temperature	Breakdown voltage (kV) (Test device)	Breakdown voltage (kV) (Trafostick™)
First oil	Before test	15 °C	72	68
	After test	35 °C	40	40
Second oil	Before test	15 °C	58	52
	After test	40 °C	29	31
Third oil	Before test	33 °C	53	62
	After test	30 °C	45	41
Fourth oil	Before test	16 °C	53	48
	After test	35 °C	41	40
Fifth oil	Before test	25 °C	43	44
	After test	45 °C	18	29

As seen in Table 2, it can be said that the breakdown voltage calculations of the Trafostick™ sensor and the test results are consistent. There are some differences, but various parameters such as the time the oil is exposed to air during sampling can affect the results. While evaluating the breakdown voltage of the transformer oil, it is more useful to examine the change in a certain period instead of examining it momentarily. According to the value of the breakdown voltage or humidity level, appropriate actions can be taken on the transformer and unplanned interruptions can be prevented[27]. For this reason, constantly monitoring the breakdown voltage online is a more reliable application than having a test at certain periods. In addition, when oil samples are taken from a transformer in operation and tests are carried out, the results may be affected by environmental conditions and the equipment used in the laboratory. In this context, the applicability of the trend analysis approach of online breakdown voltage monitoring systems is important because of the shortening of the response time in case of risk occurrence and predictive maintenance applications thanks to continuous monitoring.

By evaluating the data of the five heating analyses carried out, the relationship between the breakdown voltage of the Trafostick™ sensor and the relative humidity was examined. In this context, the moisture values in all the data and the breakdown voltages were matched and plotted on a graph. The breakdown voltage given by the Trafostick™ sensor according to the relative humidity is shown in Figure-8. According to the results shown in Figure 8, a curve was created to calculate the breakdown voltage from the relative humidity. This curve

is shown as the black line shown in Figure 8 and its equation was obtained. After the relative humidity values of the E+E™364 and Sensirion SHT10 sensors are verified with the Trafostick™ sensor, the equation obtained will be used in the breakdown voltage estimation.

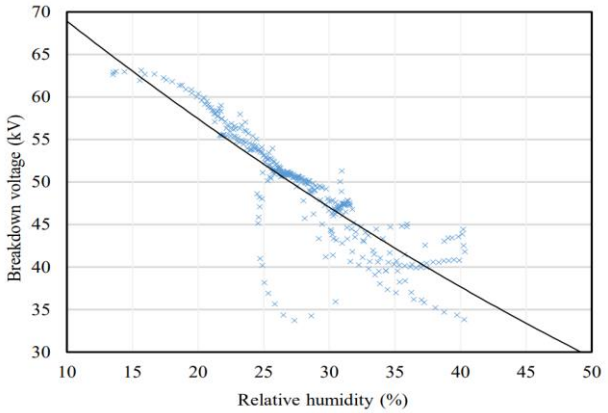

Figure 8. The graphical status of the relative humidity values corresponding to the breakdown voltages according to the Trafostick™ data obtained as a result of the heating tests

4.2. Long Term Field Measurement

After the accuracy of the Trafostick™ sensor was confirmed by the test results, the transformer where the Trafostick™ and E+E™364 sensors were mounted was taken to the place where it was planned to be installed and commissioned. At this stage, the relative humidity measurement values of the Trafostick™ and E+E™364 sensors have been compared. The E+E™ sensor only outputs relative humidity and temperature. In this context, by using the temperature and humidity values measured by the E+E™ sensor, we will try to approximate the breakdown voltage calculated by the Transformer sensor. In the next step after the verification, the relative humidity value of the E+E™364 sensor and the Sensirion sensor will be compared and the breakdown voltage will be tried to be estimated by calculations. In this context, after the installation of the transformer, the data of both sensors were compared and examined. Accordingly, the temperature and humidity values are shown in Figure 9.

According to the measured data examined, it is seen that the relative humidity values of the E+E™364 and Trafostick™ sensors are consistent. To ensure this consistency, the raw data of the E+E™364 sensor has been multiplied by a constant value. Since the sensors are different, it is considered natural to have differences between them. In the literature, it is seen that there are similar differences due to the different reference values of sensors belonging to different brands. Since the data of the Trafostick™ sensor is considered as a reference, the data of the E+E™364 sensor has been manipulated to be close to the data of the Trafostick™ sensor.

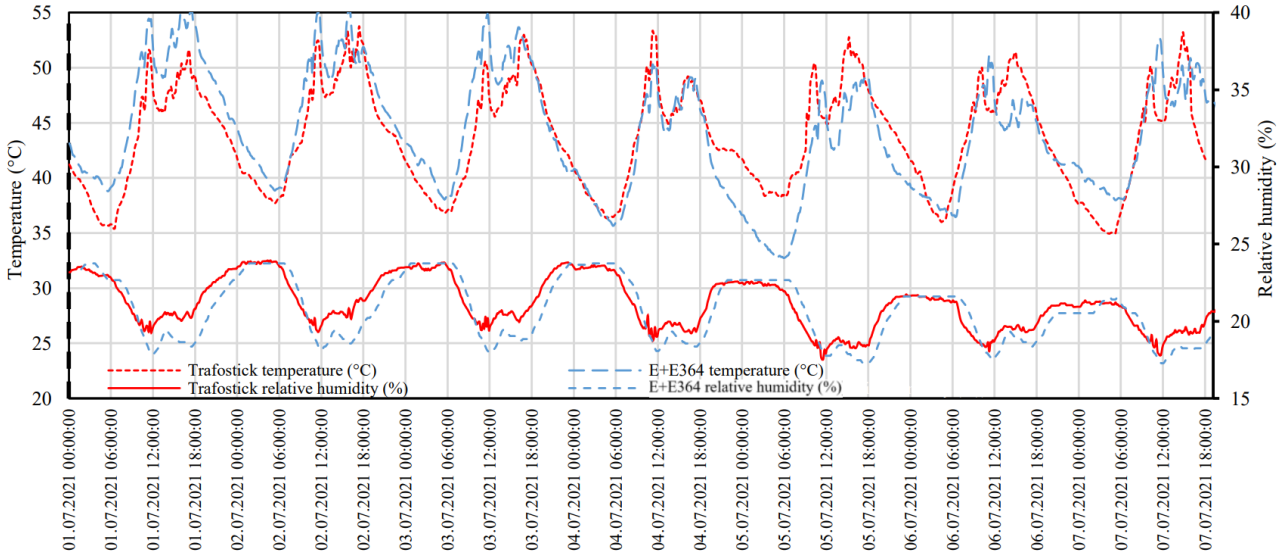

Figure 9. As a result of long-term field measurement, the relative humidity and temperature graph, taken from the Trafostick™ and E+E364 sensor in a one-week time interval.

The breakdown voltage was calculated with the measured data of the E+E™364 sensor, using the relationship between the breakdown voltage and the relative humidity obtained from the heating test. For this purpose, the relative humidity value of the manipulated E+E™364 sensor was multiplied by the formula obtained from the heating test to estimate the breakdown voltage. When the estimated breakdown voltage is compared with

the Trafostick™ sensor, it is seen that the results are close to each other. The graph in which these data are compared is shown in Figure 10.

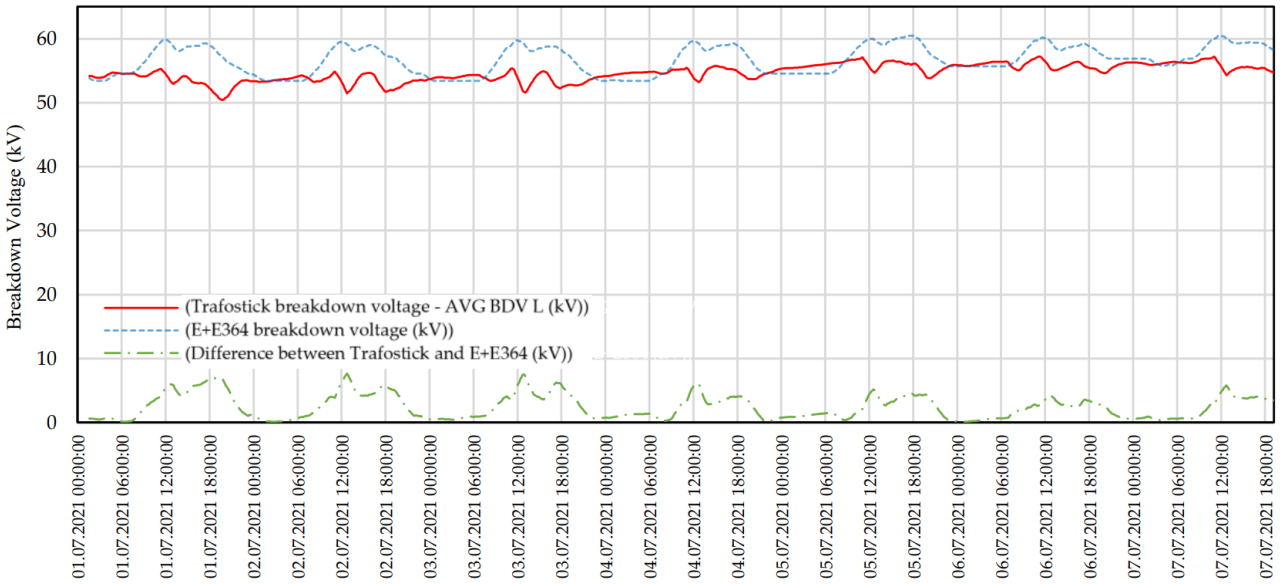

Figure 10. As a result of long-term field measurement, the breakdown voltage graph, taken from the Trafostick™ and E+E364 sensor in a one-week time interval.

When the breakdown voltage graph is examined, it is seen that the results are consistent. In some areas, even if the difference gets higher, the values are still close. In this context, it has been confirmed that the curve created according to the results of the heating test for the estimation of the breakdown voltage from the relative humidity is approximately consistent.

4.3. Measurement Studies with Sensirion

In the heating tests and long-term field measurement studies, the breakdown voltage data of the Trafostick™ sensor was confirmed by laboratory tests, and the relative humidity data was compared with the data of the E+E™364 sensor. Approximate breakdown voltage was calculated according to the relative humidity data from the formula created with the help of the obtained breakdown voltage and humidity graph. In this context, it is aimed to calculate the approximate breakdown voltage with the Sensirion™ SHT10 sensor, which is a low-cost single sensor. The relative humidity value obtained from this sensor has shifted with a constant to equalize with the relative humidity value given by the Trafostick™ sensor and the breakdown voltage is calculated. In the previous section, the relative humidity value of the E+E™364 sensor and the breakdown voltage were calculated. Measurement studies carried out in this section were made with Sensirion SHT10 and E+E™364 sensors. These two sensors were immersed in transformer oil in a jar and measurements were taken. Since the data belongs to E+E™364 sensor and Trafostick™ compared, E+E™364 accepted as a reference in this step. In this context, firstly, the manipulated relative humidity values of the E+E™364 sensor according to the Trafostick™ sensor were compared with the Sensirion™ SHT10. The difference between the response times due to the membrane structure of the sensors used in the study is reflected in the graphics.

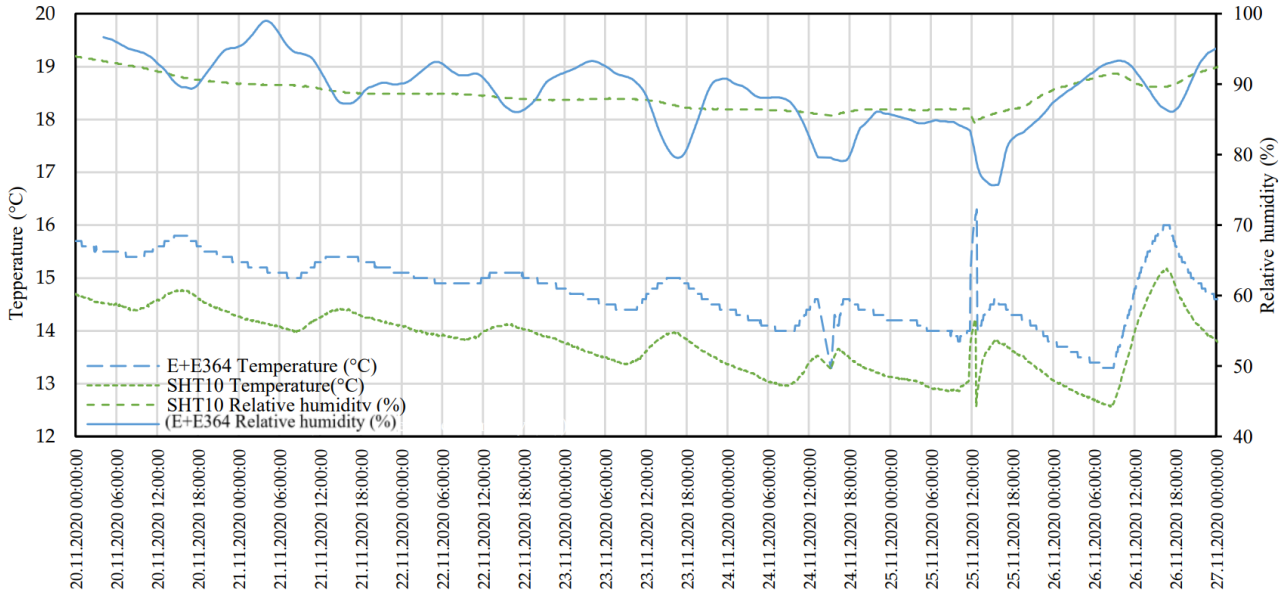

Figure 11. As a result of the measurement studies carried out with the SHT10 and E+E364 sensors, the temperature and relative humidity graphs of both sensors were taken in a one-week period.

The relative humidity-time graph formed according to the measurement results is shown in Figure 11. Here, the relative humidity value of the E+E™364 is 1.1 times higher than the measured value. This manipulation was applied since the Trafostick™ has been considered as a reference. The data of the SHT10 sensor is multiplied by 1.24, at this rate the data of the two sensors were very close to each other. This difference occurred due to the different calibration settings of the sensors, this problem almost disappears with manipulated values. According to the breakdown voltage-relative humidity graph obtained from the heating tests, the output of the SHT10 and E+E™364 sensors and the estimated breakdown voltage graph are shown in Figure-12.

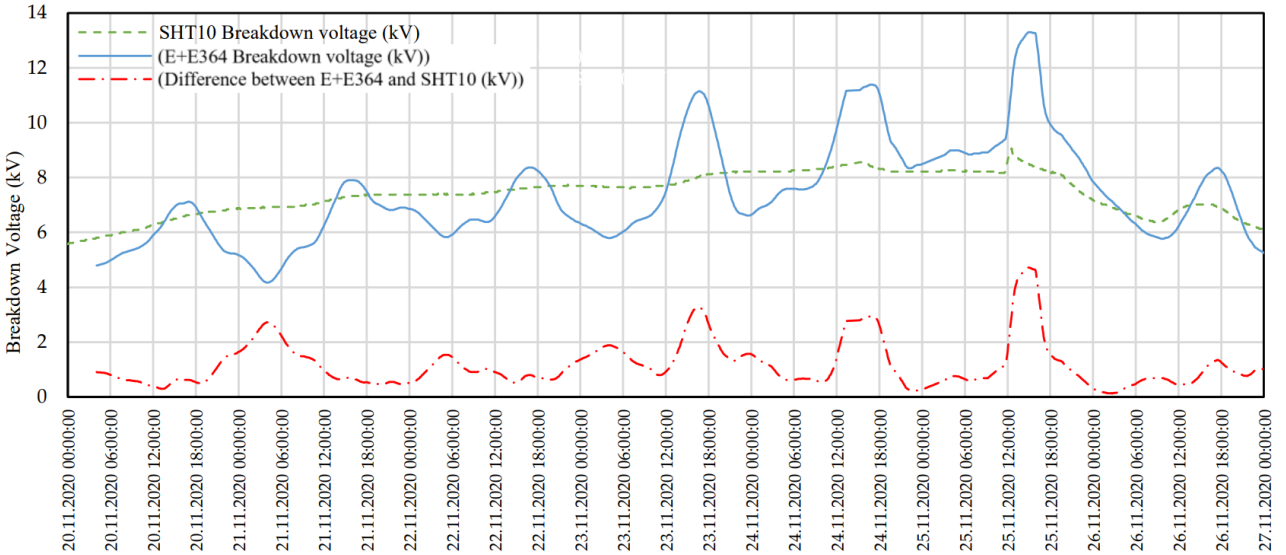

Figure 12. As a result of the measurement studies carried out with the SHT10 and E+E364 sensors, the breakdown voltage graph of both sensors was taken in a one-week period.

5. Conclusions

Dielectric oils are used in transformers to provide insulation inside the tank. The breakdown voltage of these oils is directly dependent on the humidity and temperature values. As the relative humidity of the oil increases, the breakdown voltage decreases. In addition, the moisture content directly affects the life of the transformer. In this context, continuous monitoring of the humidity, temperature and breakdown voltage of the transformers and trend analysis applications are important in terms of operational reliability. With online monitoring systems,

different analysis results can be combined, and predictive maintenance applications can be carried out together with health index studies.

This study aims to develop an approach that measures humidity, temperature and estimates approximate breakdown voltage using a low-cost single sensor. In line with this goal, first of all, laboratory tests were carried out together with the heating tests by using the Trafostick™ by Passerro, which is an industrial oil monitoring sensor that calculates the breakdown voltage in transformer oils with high accuracy, and it has been confirmed that the product calculates the breakdown voltage reliably. At this stage, an equation was created between the relative humidity and breakdown voltage values to be used in other sensors. Then, the relative humidity values measured by the E+E™364 by E+E™ sensor were verified with reference to the Trafostick™, and the breakdown voltage was calculated. Finally, measurements were taken with the low-cost single sensor. The measurements were verified, and the breakdown voltage was calculated with the obtained formula. The features related to sensors and measurements are mentioned in detail in the article.

In this context, the relative humidity in the transformer oil was measured with the Sensirion used to measure the humidity in the air in a single sensor structure, and the breakdown voltage was calculated approximately. Although the calculated breakdown voltage is not as consistent and reliable as an industrial product e.g. Trafostick™ and conventional oil testers, it provides an advantage in terms of the feasibility of the trend analysis approach by enabling continuous monitoring. It is seen that the low-cost single sensors are suitable for use in trend analysis and health index applications in distribution transformers that are not at very high power levels and have a low risk ratio. In addition, it is recommended that products with high reliability of calculations such as Trafostick™ should be used in transformers with high power or in critical position.

Declaration of Ethical Standards

The authors of this article declare that the materials and methods used in this study do not require ethical committee permission and/or legal-special permission.

Conflict of Interest

The authors declare that they have no known competing financial interests or personal relationships that could have appeared to influence the work reported in this paper.

References

[1] Dupont C., Beauchemin C., Buckley G., Bukvic M., 2015. Cigré Brochure 630 A2.44 -Guide On Transformer Intelligent Condition Monitoring (TICM) Systems. CIGRE Tech Broch.

[2] Tenbohlen S., Jagers J., Bastos G., Desai B., Diggin B., 2015. Cigré Brochure 642 A2.37 -Transformer Reliability Survey. CIGRE Tech Broch.

[3] Atanasova I., Agren P., Cucek B., Davidov V., 2018., Cigré Brochure 741 D1.52 -Moisture Measurement and Assessment in Transformer Insulation – Evaluation of Chemical Methods And Moisture Capacitive Sensors. CIGRE Tech Broch.

[4] Pahlavanpour B., Pablo A., Tumiatti W., Martins M., 2010. Cigré Brochure 413 D1.01 -Insulating Oil Regeneration and Dehalogenation. CIGRE Tech Broch.

[5] Solokov V., Aubin J., Davydov V., Gasser H., Griffin P., 2008. Cigré Brochure 349 A2.30 - Moisture Equilibrium and Moisture Migration Within Transformer Insulation Systems. CIGRE Tech Broch.

[6] Du Y., 1999. Moisture equilibrium in transformer paper-oil systems. IEEE Electrical Insulation Magazine, **15**, pp.11–20.

[7] Julliard Y., Badent R., Schwab AJ., 2001. Influence of water content on breakdown behavior of transformer oil. Paper presented at Annual Report Conference on Electrical Insulation and Dielectric Phenomena, Kitchener, Canada, 14-17 October, pp. 544–547.

[8] Lewand L., 2002. Understanding Water in Transformer Systems. Neta World, pp. 1–4.

[9] Roizman O., 2019. Moisture equilibrium in transformer insulation systems: Mirage or reality? Part 1. Transformers Magazine, **6**, pp. 44–51.

[10] Gradnik T., Končan-Gradnik M., Petric N., Muc N., 2011. Experimental evaluation of water content determination in transformer oil by moisture sensor. Paper presented at IEEE International Conference on Dielectric Liquids, Trondheim, Norway, 26-30 June, pp. 1–4.

[11] Wrobel M., 2017. Acoustic hybrid sensor for BDV monitoring in insulating oil. Paper presented at IEEE International Ultrasonics Symposium, Washington, DC, USA, 6-9 September, pp. 1–5.

[12] Martin D., Saha T., Perkasa C., Lelekakis N., Gradnik T., 2016. Fundamental concepts of using water activity probes to assess transformer insulation water

content IEEE Electrical Insulation Magazine, **32**, pp. 9–16.

[13] Pagger E., Muhr M., Pattanadech N., Kongdang P., Tieber M., Rapp K., Maneerot S., 2020. How Water Affects the Properties of Insulating Liquids. Paper presented at 8th International Conference on Condition Monitoring and Diagnosis, Phuket, Thailan, 25-28 October, pp. 322–325.

[14] Gradnik T., Čuček B., Končan-Gradnik M., 2014. Temperature and chemical impact on determination of water content in dielectric liquids by capacitive moisture sensors. Paper presented at 2014 IEEE 18th International Conference on Dielectric Liquids, Bled, Slovenia, 29 June-3 July, pp. 1–5.

[15] Du Y., Mamishev A V., Lesieutre BC., Zahn M., Kang SH., 2001. Moisture Solubility for Differently Conditioned Transformer Oils. IEEE Transactions on Dielectrics and Electrical Insulation, **8**, pp. 805–811.

[16] Villarroel R., García de Burgos B., García DF., 2021. Moisture dynamics in natural-ester filled transformers. International Journal of Electrical Power & Energy Systems, **124**, pp. 1–11.

[17] Hasheminezhad M., Ildstada Nysveen E., 2008. Electrical breakdown strength of interfaces between solid insulation and transformer oil with variable water content. Paper presented at Conference on Electrical Insulation and Dielectric Phenomena, Quebec, QC, Canada, 26-29 October, pp. 575–578.

[18] Cybulski M., Przybylek P., 2021. Application of molecular sieves for drying transformers insulated with mineral oil, natural ester, or synthetic ester. Energies, **14**, pp. 1–13.

[19] Nurcahyanto H,, Nainggolan JM,, Ardita IM,, Hudaya C,, 2019. Analysis of Power Transformer's Lifetime Using Health Index Transformer Method Based on Artificial Neural Network Modeling. Paper presented at International Conference on Electrical Engineering and Informatics, Bandung, Indonesia, 9-10 July, pp. 574–579.

[20] Azmi A., Jasni J., Azis N., Kadir MZAA., 2017. Evolution of transformer health index in the form of mathematical equation. Renew Sustain Energy Rev, **76**, pp. 687–700.

[21] Trafostick™ website, https://en.passerro.eu/Trafostick™.

[22] E+E364 website, https://www.epluse.com/products/moisture-in-oil-instrumentation/oil-measurement-transmitter/ee364/.

[23] Sensirion website, https://www.sensirion.com/en/environmental-sensors/humidity-sensors/.

[24] Solokov V., Alcantara G., Astrom B., Aubin J., 2003. Cigré Brochure 227 A2.18 -Life Management Techniques for Power Transformers. CIGRE Tech Broch.

[25] IEC International Standart-TC 10. IEC 60156: Insulating liquids — Determination of the breakdown voltage at power frequency — Test method, 1996.

[26] IEC International Standart-TC 10. IEC 60422: Mineral insulating oils in electrical equipment — Supervision and maintenance guidance, 2013.

[27] IEEE Guide for the Evaluation and Reconditioning of Liquid Immersed Power Transformers. IEEE Std C57140-2006.

Koc. J. Sci. Eng., 7(1): (2024) 20-29 https://doi.org/10.34088/kojose.1126357

Kocaeli University

Kocaeli Journal of Science and Engineering

http://dergipark.org.tr/kojose

Energy and Exergy Analysis of Heat Recovery from the Accumulating Tanks of a Central Heating System by Employing a Sample of Thermoelectric Generators

Orhan SAHMERDAN [1], Ismet TIKIZ [2,*]

[1] *Department of Mechanical Engineering, Kocaeli University, Kocaeli, 41001, Turkey,* ***ORCID:*** *0000-0001-8129-6808*
[2] *Department of Marine Engineering, Kocaeli University, Kocaeli, 41001, Turkey,* ***ORCID:*** *0000-0003-4477-799X*

Article Info

Research paper

Received : *June 5, 2022*
Accepted : *April 8, 2023*

Keywords

Analysis
Energy
Exergy
Thermoelectric Generator

Abstract

Heat recovery using a series of thermoelectric generator (TEG) samples improved and studied previously is investigated in this paper. For this, such TEGs are connected to the accumulating tanks (ATs) of a geothermal central heating system assisted by natural gas to recover all waste heat from those devices. The study was carried out based on energy and exergy analysis. In the energy analysis part of the study, the proposed energy conversion efficiency of the TEG sample for the temperature difference in an AT-TEG system in this current study, which is 2%, was applied to find power output and energetic efficiency. As a result, total net power production was 9.888 kW, while overall energy efficiency was 7.717%. It can be observed that this amount of net power generation is sufficient to supply 61.262% of the electrical power needed for the circulating pumps in the remaining parts of the central heating system. This research reveals that TEG application in heat recovery is a promising way forward, but there is still a need to enhance the conversion efficiency of such devices.

1. Introduction

The Peltier effect in cooling usage that consumes electricity to be powered and the Seeback impact on a usage that produces electricity due to a temperature difference are the two purposes that define thermoelectric use. In this paper, the former category needs to be studied; only applications producing electricity are addressed.

The applications of a TEG can be categorized into three classes according to the type of heat source: (i) waste source of heat, (ii) natural source of heat, and (iii) radioisotope source of heat.

A substantial amount of low-grade waste heat is discarded into the atmosphere with no attempt to recover it. Thermoelectric (TE) technology may readily be merged with the physical properties of a specified heat recovery (HR) application, such as the pressure, temperature, and heat transfer fluid. A TE's waste heat recovery techniques (WHR) can be divided into two primary groups: WHR from transport systems and WHR from industry and homes.

In Europe, around 20% of the total CO2 emissions are caused by road transportation, of which three-fourths stem from automobiles, and similar percentages are also present in Asia and America. For light commercial vehicles and passenger cars, European policies aim to reach a CO2 emission goal of 95 g/km and 68 g/km by 2021 and 2025, respectively. It is worth considering that 66.66% of the energy produced by combustion in a vehicle is wasted as drain heat, and 40% of this quantity is contained in the hot exhaust gas. Therefore, it will be feasible to decrease fuel consumption by about 10% if around 6% of the waste heat in exhaust gases can be converted into electricity. This is why the central European, Asian, and American automakers are working to improve different types of TEGs to maintain and gain an additional share of the private car market in the future, which is predicted to be more constrained. Furthermore, they collaborate with research universities and institutes to develop vehicle models with better fuel economy [1].

In this regard, Lan et al. [2] designed a dynamic type TEG consisting of commercial thermoelectric modules and counter-flow heat exchangers (HXs) to recuperate refusal

* Corresponding Author: ismet.tikiz@kocaeli.edu.tr

heat in the exhaust gas of a heavy-duty vehicle. They modeled a TEG mounted on the after-treatment system of the car to estimate the power production and temperatures in the dynamically operated cycle. According to the output data of the simulation, approximately 20% of the power output rise can be realized with an optimal coefficient of heat transfer of the HX on the hot side and the thermal contact conductance. Orr et al. [3] studied two beneficial up-and-coming technologies: TEGs and heat pipes (HPs). They indirectly aimed to enhance a car's efficiency by employing a junk heat retrieving-based system. They concluded that HPs could decrease the thermic resistance between the gases and TEG. Also, HPs can reduce pressure loss in the gas flow thanks to a narrowed fin surface area.

Furthermore, HPs can regulate the temperatures of the TEGs and enable a more flexible design due to the TEG position that is not constrained to the surface of the exhaust pipe. Luo et al. [4] conducted an optimization study based on the structure of a converging TEG to develop the performance of waste heat recovery. Additionally, they assessed the TEG system behavior by proposing a numerical model based on a multiphysics fluid-thermoelectric system. They concluded that the converging TEG produces more electricity, causes a lower pressure loss on the backpressure side, and provides a more uniform temperature gradient than the classic structure. Finally, Ziolkowski et al. [5] applied simulations to a TEG between the cool bypass and hot side stream at the nozzle of an aero turbofan engine. The finite element model (FEM) served as the basis for these simulations. They observed that the output power runs at 1.65 kW per engine when covering the TEG face with the entire nozzle surface.

Moreover, system-level requirements for gravimetric power density greater than 100 W/kg can be met with only a 21% fill factor. F. Kousksou et al. [6] investigated the electric power possible from the conical nozzle of a helicopter with thermoelectric modules (TEMs). The TEM in this system was exposed to hot exhaust gas from the helicopter's turbine and coolant oil. According to the results obtained for different working conditions, the electrical power generation in actual working conditions is notable but insufficient in terms of the weight-to-power ratio. Eddine et al. [7] studied the characterization and optimization of a TEG prototype for a marine engine. The power output of the TEM based on bismuth-teluride was 70% higher than the silicon-germanium TEM, but the first one deteriorated fast at inlet air temperatures higher than 300 °C. Finally, Olaniyi and Prause [8] analyzed investing in building WHR systems in ships' engines using the real-options method and usual budgeting indicators to provide assumed and predicted future alteration in the volatile maritime markets. The capital budget analysis, which provides a more realistic assessment of the project, revealed that investing in the marine WHR system is only profitable under the precise, sketchy circumstances in the study.

According to Dai et al. [9], 33% of the energy produc ed by industry is emitted directly into cooling systems or th e atmosphere as waste heat in the United States. If TEMs w ith ZT values on average varying between 1 and 2 exist, thi s heat could generate between 0.9 TWh and 2.8 TWh of ele ctrical power annually. As a result, technical and economic analyses are required to improve the possibility of widespr ead use of TEGs in the medium and long term. That analys is may make the heat a competitive, clean energy source. O ver the last three decades, a concerted effort has been made to improve the efficacy of TEMs in HR systems [1].

For example, Wang et al. [10] conducted an empirical study to recover waste heat at high temperatures by a heat pipe TEG in industrial applications. They designed and fabricated an experimental rig of HPTEG constituted of skutterudite TEGs and potassium HPs to acquire electric generation and passive thermal management. They realized that the effective thermal conductivity of the HP reaches 35831 W/mK, which is 100 times higher than that of copper at 630 °C. Employing an effective thermal conductivity and seeback coefficient, the simulation deviation of HPTEG system performance has been significantly reduced. Meng et al. [11] analyzed the impacts of some crucial parameters, like cooling water and exhaust gas heat transfer coefficients and the inlet temperature of the exhaust gas, on the ideal length of the TE for industrial gas phase application to recover waste heat. They derived that the temperature of the gas decreased fast due to the less specific heat value of the exhaust gas. Improving gas heat transfer can effectively increase power output but not efficiency. The heat transfer coefficient and inlet temperature of the exhaust gas have a remarkable impact on the ideal length of the thermoelectric elements, which is approximately 2 mm. Araiz et al. [12] suggested applications of TEGs to convert the waste heat of hot gas into beneficial electricity at a stone wool-producing plant. They employed, improved, and validated two models combined to carry out optimization from a double perspective: energy output and economic cost.

According to the simulated findings, the optimal net output power generation was 45838 W with a filling ratio of 0.40 and a fin space of 10 mm. For the filling ratio of 0.24, a minimal installation cost of 10.60 €/W was observed. The levelized cost of electricity for a TEG was computed for the first time in this study, and it was around 15 c€/kWh. Zou et al. [13] conducted an empirical and mathematical modeling study on WHR from wastewater to produce electricity by a Bi2Te3-based TEG system with a low-temperature distribution. They presented data

revealing a potential for the direct generation of electricity based on TEG through advanced source recovery from wastewater and motivated the future discovery of this procedure. Ramadan et al. [14] proposed a system based on three components: the condenser exhaust airflow that is emitted by the condenser of a heating, ventilation, and air conditioning (HVAC) system; the exhaust airflow of the HVAC system, which is used as the cool side; and TEG to generate green electricity. According to the findings, with a cooling load of 100 kW for the space, a 40 by 40 cm2 flat plate can produce 90 W of electricity.

All too many home applications emit energy as heat within water or exhaust gases [15]. Therefore, many studies have been conducted to recover this heat from the sources in question. For example, Khaled and Ramadan [16] proposed a system with TEG comprised of a multi-tube tank heat exchanger, utilizing the exhaust gases of a chimney to heat residential water by WHR. They studied the system's thermal behavior to determine the effects of the various heat transfer modes driving the system by presenting a prototype to be applied and tested. According to tests, the temperature of a 95-liter water tank can be raised by 68 °C in one hour. Also, the convection and radiation changes at the tank's bottom surface significantly affect the water's overall heat transfer rate (as high as 70%). Panwar and Kumar [17] developed a family-sized cookstove operated by biomass and equipped with a TEG to generate electricity by using the waste heat released from the outer casing and grill of the cooker. An oblong metal plate with a 0.12×0.08 m2 area was employed to line up five TEG modules. The panel was bonded to the outer casing of the cookstove to derive waste heat lost via conduction. The TEG's produced electricity was utilized to drive a small fan (12 Volt DC, 0.16 A) that provided fuel combustion primary and secondary fans. It was discovered that the generated power was sufficient to run the fan in the mode of forced air supply, while it was insufficient in the natural operating state. Sakdanuphab and Sakulkalavek [18] devised and implemented a waste heat recovery (WHR) system to utilize waste heat from a cooking burner. The thermal energy of the burner was transformed into electrical power by a TEG and used in a hot water boiler. The temperature of the heater was found to be more effective than the volume of water. In addition, the thermal efficiency of a cooking stove outfitted with the WHR system was assessed. Results demonstrated that its thermal efficiency declined by less than 5% when mounting the WHR system. Montecucco et al. [19] presented a TEG application for heat transfer to the water for domestic or heating use while also charging a lead-acid battery for a solid-fuel stove. A general solid-fuel stove indicates the practicability of the suggested combined heat and power (CHP) system. During a 2-hour test, this system generates an average of 27 W (42 W electricity peak) and 600 W of thermal energy, demonstrating the maximum power point tracker (MPPT) efficiency of the power transformers used and the TEG efficiency of about 5%. Jaber et al. [20] studied a hybrid HR system, which produces electrical power by utilizing a TEG and domestic hot water, to evaluate the effect of varying the temperature of exhaust gases on the system's performance. They applied a resistive thermal model to determine the temperature of the exit water and power generation via TEGs. According to the results, when the temperature of the exhaust gas increases, the temperature in the HX without layer discrimination and heat rate rise linearly. Additionally, the power generation of TEGs rises with increasing exhaust gas temperatures.

Producing electrical power from natural heat sources by using TEG can be divided into three groups: (i) sun sources, (ii) human bodies, and (iii) natural gases and biomass.

Applications of solar thermoelectric generators (STEG) are based on recovering heat from solar radiation and transforming it into electrical power using a TEG. Although its conversion efficiency is low, it has been an alternative and is rivaling solar photovoltaic systems [1]. Indra et al. [21] reviewed different combination alternatives of concentrator photovoltaic (CPV)-TEG applications and current developments of various geometries of hybrid CPV-TEG systems containing CPV-TEG with phase-changing material, CPV/thermal-TEG and CPV-TEG with a spectral beam splitter. They dedicated it to the fact that a CPV-TEG solar system has higher thermal and electrical efficiency than a standard PV-TEG system. They also made some suggestions for future improvements to CPV-TEG systems. Faddouli et al. [22] analyzed a novel solar system directly coupled with a TEM regarding energy efficiency to generate electricity and heat simultaneously, use the entire solar spectrum, and enhance the efficiency of conventional solar collectors. They found that the novel hybrid system remarkably enhances the storage process by varying the flow rate depending on the concentration. This flow rate reaches the amount of 1200.453 l/day and provides considerable extra electrical energy around 10.41 W with a $0.92 \times 1.9 \times 0.05$ m3 collector sloping 30° under 20 suns.

Because human body heat is natural and immovable, it may generate energy in specific applications, such as medical ones. The human body generates between 100 and 525 W of heat at rest and during physical exercise. Many investigations have been conducted since 2001 to produce wearable thermoelectric generators (WTEGs) [1]. For instance, Sun et al. [23] made a woven thermoelectric cloth, designing an unostentatious operating TEM without using thermoelectric fibers. Using elasticity welding on interlaced TEMs, tensible 3D TEGs without an underlayer

can be produced to achieve sufficient alignment with the heat flux direction. The textile producer demonstrates a maximum power density of 70 mW/m2 and great tensibility with no production deformation at a 44 K temperature difference. Xu et al. [24] proposed a plan of dimensionality morphology to manufacture organic-inorganic TE composites. A maximum normalized power density for a prototype TEM based on suitable flexible composites in the whisker-like semiconductor Ta4SiTe4 with substantial interfacial conformity and chain-shaped polyvinylidene fluoride (PVDF) was stated. It was discovered that a lesser number of n/p pairs are required for a module to satisfy the outset voltage, owing to the composite having a high seeback coefficient.

TEGs, or thermopiles, are currently configured to provide energy for autonomous sensors established in remote locations due to harsh ambient conditions, i.e., inaccessible places with shallow temperatures where traditional alternative energy sources, such as wind and solar energy, are not available regularly. Heat is often delivered via a flameless catalytic burner. TEGs energized by natural gas are fabricated in more than 55 countries. For example, Gentherm produces TEGs whose powers vary between 15 W and 550 W. Those TEGs are generally employed on petrol platforms, at high altitudes, along pipelines, or near gas wells. Farwest Corrosion Control is another case in point, a corporation that produces and installs TEGs to avoid pipe corrosion through cathodic protection and has over 15,000 generators in 51 countries.

Many goods have been designed and marketed for public use. The thermoelectric candle radio (1990) can be cited as an example, which utilizes the heat from candles to energize a radio with iron disulfide (FeSi2) TE. However, these technologies need to be updated due to the appearance of other more advantageous applications. Yet there are even more unique applications like CampStove. In general, this device was projected for camping to generate 5 V and 2 W of 0.4 A power by burning wood and using a TEG to which electrical gadgets can be attached through a USB port [1].

This study examines heat recovery via TEGs from the accumulating tanks (ATs) of a geothermal central heating system (GCHS) assisted by natural gas based on energy and exergy analysis. This application of a TEG falls under the heading of ‘waste heat recovery from industry and homes.' In this field, research has been done on heat recovery from municipal wastewater, hot gases from factories and wood stoves, the heat emitted from air conditioning systems, the heat of boilers for autonomous working, hydronic central heating units on a residential scale to supply electrical power for their equipment, and lastly, work equipment in a natural gas field. However, as seen from the latest explanation, even though there are some applications of heat recovery from industry and homes in the literature, there still needs to be more heat recovery from some devices of a central heating system on an industrial scale. That is the reason that encourages us to carry out the current analysis. In this study, we aim to mount a TEG sample with an 8% conversion efficiency at a 230 °C temperature difference between its hot and cool sides to the ATs of a GCHS and find energetic and exergetic results for the temperature difference and usage proposed in this study. The GCHS was studied by [25], while the TEG was submitted and fabricated by [26].

2. Materials and Methods

2.1. System Description

The GCHS, assisted by liquid natural gas (LNG), is in Oylat Spa Town, Bursa Province, not southwest Turkey. The schematic layout of the GCHS is depicted in Figure 1. The GCHS uses low-enthalpy geothermal water and LNG as energy sources for heat generation to heat the districts' hotel rooms.

The geothermal water (GW) springs from the production well at 40 °C; then, it is conveyed to the geothermal pool (GP). The GW exits the pool at 35 °C since some of its heat is obtained by the heat exchangers (HEs) there. Afterward, the heat derived by the HEs is transferred into the circulating water (CW) between the heat pumps (HPs) and HEs, increasing the temperature of this CW from 20 °C to 30 °C. In the HP-HE cycle, the CW enters the first HP at 30 °C and leaves the second HP at 20 °C. The temperature of the CW decreases by 5 °C in each one of these HPs subsequently. In the AT-HP cycle, the temperature of the CW rises to 60 °C from 50 °C, with a 5 °C increase in each HP. In a word, the heat acquired from the GW is transmitted into the water in the ATs.

Additionally, the heat from firing the natural gas in the condensing combi boilers (CCBs) is transmitted into the ATs through the CCB-AT cycle to supply additional heat for the districts. The CCB group contains 8 CCBs, which raise the water temperature in the CCB-AT cycle from 60 °C to 80 °C.

All heat acquired from the GW and natural gas is first transferred into the water in ATs and then conveyed to the wall heating panels (WHPs). In the case of heating the districts with only the GW, the temperature of water circulated between ATs and WHPs ranges from 53 °C to 60 °C, while it is between 73 °C and 80 °C, providing extra heat by firing natural gas. In this paper, calculations have been performed for the latter case.

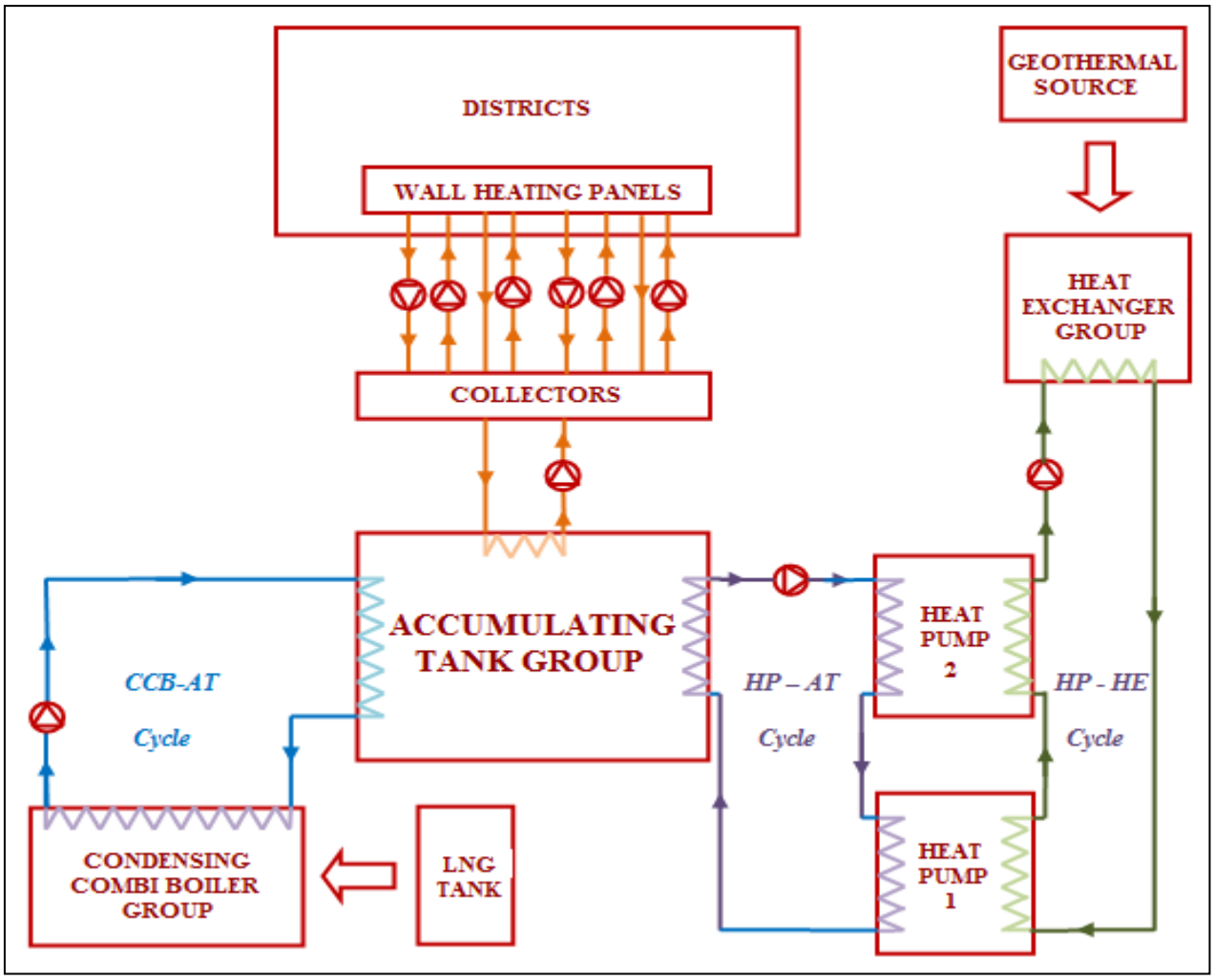

Figure 1. The schematic presentation of the GCHS was studied by [25].

It can be seen that the ATs in the AT group serve as a bridge in the entire system because all heat attracted from the sources is first transferred into the water in this group before it is transported to the WHPs. That is why a significant amount of heat loss occurs in the AT group, and some of it can be recovered by mounting TEGs.

The AT group contains 6 ATs with a total heat loss and storage capacity of 645.960 kW and 30000 lt, respectively. Therefore, the heat loss and storage capacity per AT are 107.660 kW and 5000 lt, respectively. 2 TEGs are connected to an AT, so there are a total of 12 TEGs, and each TEG acquires 53.830 kW of heat energy from an AT. Therefore, the identical AT-TEG systems are working under the same conditions. The calculations have been performed for only one AT-TEG system. The overall energy and exergy results have been determined for all AT-TEG systems by multiplying the values found for one system by 6.

The schematic layout of one AT-TEG system is depicted in Figure 2. In this system, the hot side water leaves the AT at a mass flow rate of 4 kg/s and 80 °C (point 1). Then, it splits in half and enters each of the 2 TEGs at a 2 kg/s flow rate and 80 °C (points 2 and 3). In each TEG, the heat of the hot side water is released into the coolant water. The hot side water then exits each TEG at 2 kg/s and 73.6 °C (points 4 and 5) and returns to the AT at 4 kg/s and 73.6 °C (point 10).

The coolant water is indeed the GW leaving the geothermal pool at 35 °C. We imagine transporting some of this water to the cold sides of the TEGs to be used as coolant water via 12 water lines independent of each other. So, there is one water line for one TEG (6-7 and 8-9). In a water line, the coolant water enters a TEG at 35 °C (points 6 and 8) and exits it at 38.6 °C and 3.5 kg/s mass flow rate (points 7 and 9). The flows of the coolant and hot side water through the TEG are in reverse directions from each other.

A TEG is primarily based on the Seeback effect, invented by Thomas Seeback [27]. As shown in Figure 3, the TEG sample that we use is made up of top and bottom aluminum nitride (AlNi) substrates with low electrical conductivity but high thermal conductivity to effectively

transfer heat from the hot side to the TEG, copper (Cu) links that provide a series of electrical connections, joint bars that supply thermal and electrical conduction between

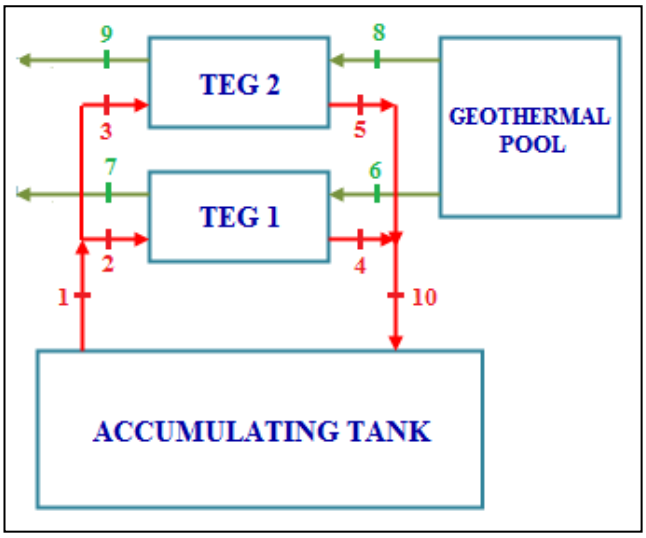

Figure 2. The schematic layout of the AT-TEG system.

Table 1. The inlet and outlet temperatures of the hot side and coolant fluids.

Fluid	Inlet Temperature (°C)	Outlet Temperature (°C)	Mean Temperature (°C)
Hot Water	80	73.5	76.8
Coolant Water	35	38.6	36.8

substrates and legs, and finally p- and n-type TE legs. Bi0.4Sb1.6Te3 and Bi2Te2.7Se0.3S0.01Cu0.01 materials are used for the p-type and n-type legs, respectively [26]. If a temperature difference ΔT occurs between the TEG substrates, the TEG generates electrical voltage [27]. The present TEG sample, developed and fabricated by [26], will be tested for a ΔT value, which is the difference between the mean temperatures of the hot side and coolant water. [26] shows the conversion efficiency for this ΔT value.

2.2. Energy and Exergy Analysis

For energy and exergy analysis of the TEGs, each TEG's energy and exergy balance formulas must be expressed and solved in order. Then, the equations below are applied:

$$\dot{Q}_{C.V} - \dot{W}_{C.V} = \sum \dot{m}_{out} h_{out} - \sum \dot{m}_{in} h_{in} \quad (1)$$

$$\dot{E}_i = \dot{m}_i[(h_i - h_0) - T(s_i - s_0)] \quad (2)$$

Where $\dot{Q}$ indicates the heat rate transferred to the control volume, $\dot{W}$ is the acquired work, h represents the fluid enthalpy, and $\dot{m}$ denotes the mass flow rate. $\dot{E}$ and s represent exergy rate and entropy, respectively, and the subscripts in and out mean the inlet and outlet. I substitute the state points.

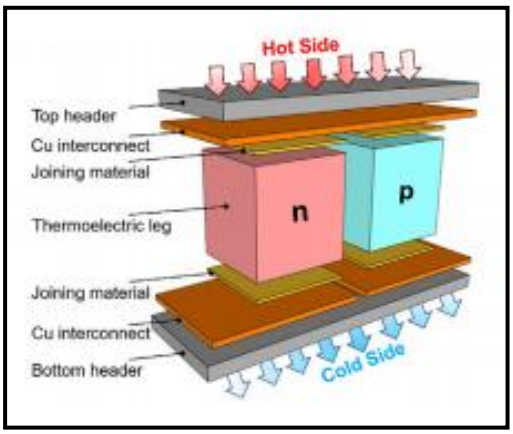

Figure 3. The schematic structure of the TEG used in this study.

The relevant thermoelectric formula is as follows:

$$\eta_{TEG} = \eta_C\left[\left(\sqrt{1+ZT_m}-1\right)/\left(\sqrt{1+ZT_m}+\right)\right] \quad (3)$$

ZT_m denotes the merit figure, typically between 0.2 and 1.6 up to the construction [28], and is taken as 1 for the temperature difference ΔT in this study.

The Carnot efficiency is denoted as follows:

$$\eta_C = 1 - (T_l/T_h) \quad (4)$$

The following is another functional formula:

$$\eta_{TEG} = 1 - \left(\dot{W}_{TEG}/\dot{Q}_{ELEGANT}\right) \quad (5)$$

where $\dot{Q}_{ELEGANT}$ is an effective electricity production apparatus for liquid bases bases and is used for thermos electrics.

$$\dot{Q}_{ELEGANT} = \dot{m}_{cooling}\left(h_{cold,in} - h_{cold,out}\right) \quad (6)$$

In other respects, the hot and cold side temperatures can be calculated by an admissible approximation as [28]:

$$T_l = \frac{1}{2}\left(T_{cold,in} + T_{cold,out}\right) \quad (7)$$

$$T_h = \frac{1}{2}\left(T_{hot,in} + T_{hot,out}\right) \quad (8)$$

where T_h and T_l are the mean temperatures of the fluids on a TEG's hot and cold sides, respectively; their numerical va

lues are given in Table 1. The conversion efficiency of the TEG sample can be reviewed for the difference between th ose temperature values (ΔT) in [26]. As can be calculated f rom Table 1, the temperature difference ΔT between the ho t and cold sides of one TEG is 40 °C. The conversion effici ency η_TEG can be taken as 2% from [26] at this temperat ure difference, besides Equations 3 and 5.

The main factors for the performance evaluation of the heat recovery system in this work are TEG unit output power, net output work, exergy destruction rate, and second law efficiency.

The total power output of the TEGs can be denoted as follows:

$$\dot{W}_{TEG,tot} = 12\ x\ \dot{W}_{TEG} \tag{9}$$

Besides Equation 5, $\dot{W}_{TEG}$ can be calculated using the conversion efficiency when a TEG's amount of acquired and released energy is known.

The net output power of the whole TEG system is denoted as follows:

$$\dot{W}_{net} = \dot{W}_{TEG,tot} - 6\ x\ \dot{W}_{pump} \tag{10}$$

$\dot{W}_{pump}$ is taken as 0.5 kW to provide power for the water fl ows on both sides of the TEG.

The overall energy and exergy efficiency of the TEGs can be denoted as follows [28]:

$$\eta_I = \dot{W}_{net}/\dot{Q}_{in} \tag{11}$$

$$\eta_{II} = \dot{W}_{net}/\dot{E}_{in} \tag{12}$$

3. Results and Discussion

The system in this paper is analyzed in two parts: In the first stage, an energy examination was conducted. To that end, the point energy and exergy values were first established. Then, the input and output energy amounts for the TEGs and the AT-TEG system were found for ΔT = 40 °C. As previously noted, the conversion efficiency for this temperature difference is estimated at 2%, according to [26]. The results for that conversion efficiency and point temperature values in the system were determined. The second portion of the study encompasses an exergy analysis. In this respect, the input and output exergy levels for each TEG and the AT-TEG system were calculated. The second law, efficiency, was established. Finally, the total results for all AT-TEG systems were computed. Table 2 displays the point energy and exergy data.

Table 2. Point thermodynamic values of an AT-TEG system in the current study.

Point	ṁ (kg/s)	T (°C)	h (kJ/kg)	s (kJ/kgK)	E (kW)	Ė (kW)
1	4	80	334.910	1.0753	1339.640	136.523
2	2	80	334.910	1.0753	669.820	68.261
3	2	80	334.910	1.0753	669.820	68.261
4	2	73.6	308	0.9982	616	57.584
5	2	73.6	308	0.9982	616	57.584
6	3.507	35	146.680	0.5053	514.406	19.323
7	3.507	38.6	161.720	0.5536	567.152	24.549
8	3.507	35	146.680	0.5053	514.406	19.323
9	3.507	38.6	161.720	0.5536	567.152	24.549
10	4	73.6	308	0.9982	1232	115.168

The energetic values of the TEGs and AT-TEG systems are represented in Table 3. According to this data, the amount of energy acquired by a TEG is 53.820 kW. So, the energy loss per TEG was calculated to be 1.074 kW by using the conversion efficiency of a TEG. Indeed, this energy loss is the amount of electrical power produced by a TEG. Then, the output of the AT-TEG system in terms of electrical power generation was found to be 2.148 kW. The first law efficiency of the AT-TEG system was found to be 1.531%, which is 0.469% lower than a TEG because the circulating pumps in the AT-TEG system consume 0.5 kW of electrical power. The total produced electrical power was 12.888 kW by multiplying the electricity generation of the AT-TEG system by 6. Since the AT-TEG systems are identical, the first law efficiency for all TEG systems was 1.531%, the same value as with only one AT-TEG system.

The results of the TEGs and systems in terms of exergy are presented in Table 4. The data shows that the exergy destruction rate per TEG is 5.451 kW, and for the AT-TEG system, it is 11.402 kW. The total exergy destruction rate is 68.412 kW. The second law efficiency is 10.06% per TEG, which is 8.06% higher than the first law

1 **Table 3.** Energetic results for the components and systems.

Components	E_{input} (kW)	E_{output} (kW)	E_{loss} (kW)	η_I (%)
TEG-1	53.820	52.746	1.074	2
TEG-2	53.820	52.746	1.074	2
Circulating Pump	1340.140	1339.640	0.5	99.5
One AT-TEG system	108.140	105.492	2.648	1.531
All AT-TEG systems	648.840	632.952	15.888	1.531

2

efficiency. This is because the input exergy is nearly 80% lower than the exergy input for a TEG. The second-law efficiency of the AT-TEG system is 7.717% and is 2.343% lower than the double-law efficiency of a TEG, which is attributed to the electrical work consumed by the circulating pumps in an AT-TEG system. All AT-TEG systems have the same second-law efficiency because they are identical.

Table 4. Exergetic results for the components and systems.

Components	$\dot{E}_{input}$ (kW)	$\dot{E}_{output}$ (kW)	$\dot{E}_{loss}$ (kW)	η_{II} (%)
TEG-1	10.677	5.226	5.451	10.06
TEG-2	10.677	5.226	5.451	10.06
Circulating Pump	137.023	136.523	0.5	99.635
One AT-TEG system	21.854	10.452	11.402	7.717
All AT-TEG systems	131.124	62.712	68.412	7.717

4. Conclusions

In this paper, a Bi-Te-based TEG, which has a relatively higher conversion efficiency than conventional TEGs, has been employed to recover the waste heat of the ATs of a natural gas-assisted central heating system. There were a total of six AT-TEG systems. In each AT-TG system, there were two TEGs linked to an AT. According to the results, one AT-TEG and the overall design have an energy efficiency of 1.531%. The comprehensive system and one AT-TEG system have an exergetic efficiency of 7.717%. The total system produced a net power output of 9.888 kW. This power can meet 61.262% of the electrical power required for the circulating pumps in the rest of the central heating system.

Declaration of Ethical Standards

The authors of this article declare that the materials and methods used in this study do not require ethical committee permission and/or legal-special permission.

Conflict of Interest

The authors declare that they have no known competing financial interests or personal relationships that could have appeared to influence the work reported in this paper.

References

[1] Zoui M.A., Bentouba S., Stocholm J.G., Bourouis M., 2020. A Review on Thermoelectric Generators: Progress and Applications, Energies,13,pp. 1-32.

[2] Lan S., Yang Z., Chen R., Stobart R., 2018. A Dynamic Model for Thermoelectric Generator Applied to Vehicle Waste Heat Recovery, Applied Energy, 210, pp. 327-338.

[3] Orr B., Akbarzadeh A., Mochizuki M., Singh R., 2016. A Review of Car Waste Heat Recovery Systems Utilising Thermoelectric Generators and Heat Pipes, Applied Thermal Engineering, 101, pp. 90-95.

[4] Luo D., Wang R., Yu W., Zhou W., 2020. A Numerical Study on the Performance of a Converging Thermoelectric Generator System Used for Waste Heat Recovery, Applied Energy, 270, 115181.

[5] Ziolkowski P., Zabrocki K., Müller E., 2018. TEG Design for Waste Heat Recovery at an Aviation Jet Engine Nozzle, Applied Sciences, 8(12), 2637.

[6] Kousksou T., Bédécarrats J.-P., Champier D., Pignolet P., Brillet C., 2011. Numerical Study of Thermoelectric Power Generation for a Helicopter Conical Nozzle, Journal of Power Sources, 196(8), pp. 4026–4032.

[7] Nour Eddine A., Chalet D., Faure X., Aixala L., Chessé P., 2018. Optimization and Characterization of a Thermoelectric Generator Prototype for Marine Engine Application, Energy, 143, pp. 682–695.

[8] Olaniyi E.O., Prause G., 2018. Investment Analysis of Waste Heat Recovery System Installations on Ships' Engines, Journal of Marine Science and Engineering, 8(10), 811.

[9] Dai D., Zhou Y., Liu J., 2011. Liquid Metal Based Thermoelectric Generation System for Waste Heat Recovery, Renewable Energy, 36(12), pp. 3530–3536.

[10] Wang C., Tang S., Liu X., Su G.H., Tian W., Qiu S., 2020. Experimental Study on Heat Pipe Thermoelectric Generator for Industrial High Temperature Waste Heat Recovery, Applied Thermal Engineering, 175, pp. 1-11.

[11] Meng F., Chen L., Feng Y., Xiong B., 2017. Thermoelectric Generator for Industrial Gas Phase Waste Heat Recovery, Energy, 135, pp. 83–90.

[12] Araiz M., Casi Á., Catalán L., Martínez Á., Astrain D., 2020. Prospects of Waste-Heat Recovery from a Real Industry Using Thermoelectric Generators: Economic and Power Output Analysis, Energy Conversion and Management, 205, 112376.

[13] Zou S., Kanimba E., Diller T.E., Tian Z., He Z., 2018. Modeling Assisted Evaluation of Direct Electricity Generation from Waste Heat of Wastewater via a Thermoelectric Generator, Science of the Total Environment, 635, pp. 1215–1224.

[14] Meng F., Chen L., Feng Y., Xiong B., 2017. Thermoelectric Generator for Industrial Gas Phase Waste Heat Recovery, Energy, 135, pp. 83–90.

[15] El Hage H., Ramadan M., Jaber H., Khaled M., Olabi A.G., 2016. A Short Review on the Techniques of Waste Heat Recovery from DomesticApplications, Energy Sources, 42, pp. 1-16.

[16] Khaled M., Ramadan M., 2017. Study of the Thermal Behavior of Multi Tube Tank in Heat Recovery from Chimney—Analysis and Optimization, Heat Transfer Engineering, 39(5), pp. 399–409.

[17] Panwar N., Kumar H., 2019. Waste Heat Recovery from Improved Cookstove through Thermoelectric Generator, International Journal of Ambient Energy, 43(1), pp. 1–17.

[18] Sakdanuphab R., Sakulkalavek A., 2017. Design, Empirical Modelling and Analysis of a Waste-Heat Recovery System Coupled to a Traditional Cooking Stove, Energy Conversion and Management, 139, pp. 182–193.

[19] Montecucco A., Siviter J., Knox A.R., 2017. Combined Heat and Power System for Stoves with Thermoelectric Generators, Applied Energy, 185, pp. 1336–1342.

[20] Jaber H., Khaled M., Lemenand T., Faraj J., Bazzi H., Ramadan M., 2017. Effect of Exhaust Gases Temperature on the Performance of a Hybrid Heat Recovery System,Energy Procedia, 119, pp. 775–782.

[21] Indira S.S., Vaithilingam C.A., Chong K.-K., Saidur R., Faizal M., Abubakar S., Paiman S., 2020. A Review on Various Configurations of Hybrid Concentrator Photovoltaic and Thermoelectric Generator System. Solar Energy, 201, pp. 122–148.

[22] Faddouli A., Labrim H., Fadili S., Habchi A., Hartiti B., Benaissa M., Benyoussef A., 2019. Numerical Analysis and Performance Investigation of New Hybrid System Integrating Concentrated Solar Flat Plate Collector with a Thermoelectric Generator System, Renewable Energy, pp. 1-38.

[23] Sun T., Zhou B., Zheng Q., Wang L., Jiang W., Snyder G.J., 2020. Stretchable Fabric Generates Electric Power from Woven Thermoelectric Fibers, Nature Communications, 11(1).

[24] Xu Q., Qu S., Ming C., QiuP., Yao Q., Zhu C., Wei T.-R., He J., Shi X., 2020. Conformal Organic-Inorganic Semiconductor Composites for Flexible Thermoelectrics, Energy &Environmental Science, 13, pp. 511-521.

[25] Yamankaradeniz N., Sahmerdan O., 2021. Energy, Exergy and Thermoeconomic Analysis of a Natural Gas Assissted Geothermal Central Heating System, Uludag University Journal of The Faculty of Engineering, 26, pp. 757-776.

[26] Nozariasbmarz A., Poudel B., Li W., Kang H.B., Zhu H., Priya S., 2020. Bismuth Telluride Thermoelectrics with 8% Module Efficiency for Waste Heat Recovery Application, iScience, 23(7), 101340.

[27] Hadjiat M.M, Mraoui A., Ouali S., Kuzgunkaya E.H., Salhi K., Ait Ouali A., Benaouda N., Imessad K., 2021. Assessment of geothermal energy use with thermoelectric generator for hydrogen production, ScienceDirect, pp. 1-11.

[28] Aliahmadi M., Moosavi A., Sadrhosseini H., 2021. Multi-Objective Optimization of Regenerative ORC System Integrated with Thermoelectric Generators for Low-Temperature Waste Heat Recovery. Energy Reports, 7, pp. 300–313.

Koc. J. Sci. Eng., 7(1): (2024) 30-41 https://doi.org/10.34088/kojose.1278657

Kocaeli University

Kocaeli Journal of Science and Engineering

http://dergipark.org.tr/kojose

Controlling a Single Tank Liquid Level System with Classical Control Methods and Reinforcement Learning Methods

Murat Erhan ÇİMEN [1], Zeynep GARİP [2, *]

[1] *Department of Electric Electronic Engineering, Sakarya University of Applied Sciences, Sakarya, 54050, Turkey,* ***ORCID:*** *0000-0002-1793-485X*
[2] *Department of Computer Engineering, Sakarya University of Applied Sciences, Sakarya, 54050, Turkey,* ***ORCID:*** *0000-0002-0420-8541*

Article Info

Research paper

Received : *April 6, 2023*
Accepted : *August 19, 2023*

Keywords

Tank System
Classical Controllers
Reinforcement learning

Abstract

In this study, the control of the single tank liquid level system used in control systems has been carried out. The control of the single tank liquid level system has been performed with the classic PI, modified PI, state feedback with integrator action, and Q learning algorithm and SARSA algorithms, one of the artificial intelligence methods. The tank system to be modelled was carried out using classical physics, namely Newton's laws. Then, the mathematical model obtained of the system that are continuous model in time is acquired. The originality of the study; the non-linear liquid tank system is controlled by classical controllers and reinforcement methods. For this purpose, the system was firstly designed to model the system, then the system has been linearized at a specific point in order to design classic PI, modified PI, and state feedback with integral. After that, agents of the Q Learning algorithm and SARSA algorithms were trained for the system. Then the agents have controlled the single-level tank system. The results of the classic controllers and supervised controllers are contrasted with regard to performance criteria such as rising time, settling time, overshoot and integral square error. Consequently, Q learning method has produced 0.0804-sec rising time, 0.943 sec settling time and 0.574 integral square errors. So, Q learning algorithm has produced and exhibited more thriving and successful results for controlling single liquid tank system than PI, Modified PI, state feedback controllers and SARSA.

1. Introduction

Machine learning is used in artificial intelligence, with the development of today's computer technology, artificial intelligence has entered many different application areas from health [1–3], and logistics [4, 5] to chemistry, finance [6], [7] to education [8] to computer game [9, 10] and industry [11– 13]. The main cause is that machine learning methods can evaluate and interpret data faster and more accurately today and make the most appropriate and correct decisions. However, according to the place of use, machine learning can be divided into branches such as supervised, unsupervised and reinforcement learning. But reinforcement learning has gained in significance since it can adapt to changing environmental conditions. An agent can interact with the environment, then it can learn what to do, depending on a specific reward. its application to many different fields has begun to be developed [13, 14]. Reinforcement learning, which has the capacity to learn its environment, could also be implemented to control nonlinear systems and industrial processes [12].

Reinforcement learning could be traced back to Bellman's work on optimal control theory in the 1950s [15]. Bellman, working on optimal control theory, developed dynamic programming, which is an approach to optimally control dynamic systems over time. In this method, a function value of a state for the system is specified by calculating the control signal. According to this value and according to the function value of the next state, iteratively discrete optimal control signal was tried to be calculated. This approach can be expressed with the Bellman Equation. Therefore, the approach that enables the calculation of the control signal using the Bellman Equation can be called dynamic programming [16]. This method can be implemented to randomly run Markovnian decision processes and systems can be controlled via MDP without knowing the model of the system. MDP generally

* Corresponding Author: zbatik@subu.edu.tr

refers to processes that depend on the current and next state. It can control MDPs with optimal control methods using dynamic programming, but it requires a processing load [17]. In addition, they have the problem of "the curse of dimensionality" as they operate for every situation [18]. In their study, Farley and Clark proposed a trial-and-error method as well as dynamic programs that evaluate each situation. They have proposed artificial neural networks that learn by trial and error. Later, Farley and Clark implemented the trial-and-error method to pattern recognition [15, 16]. Michie has used the trial-error learning system for tic tac toe game [19]. The temporal difference learning method has also been applied in playing the tic tac toe game. In fact, the basis of temporal difference learning is based on the learning psychology of animals. Minsk first noticed this in 1954 and predicted that it could be significant for learning methods [20, 21]. In the same period, Samuel developed the temporal difference method independently, influenced by chess games [22]. However, when we look at the 1980s, the trial error method, which was transferred into the temporal difference method, is mostly known as actor-critic architecture. Different versions of the temporal difference method have been developed. Later, Chris Watkins developed the Q learning method in 1989 by using the temporal difference learning method with optimal control [23, 24]. In the 1990s Tesauro developed a backgammon playing program [25]. In this method, training has been conducted using a version of the Temporal difference method and artificial intelligence [26]. In fact, the Q learning method has methods such as dynamic programming, temporal difference, and Monte Carlo [10, 27, 28]. Today we live through the information age, especially the use of reinforcement learning with methods such as deep learning [13, 28–30], which continues to be up-to-date. Moreover, it is open to development and open to application in many different fields.

The tank system has been used since Hellenistic times [31]. In particular, there are studies carried out to measure time by keeping the water level constant in the tank. In the 17th century, applications such as pressure, temperature, or speed control of the rotor were carried out in tanks. Examples of these are mechanical applications such as temperature control for furnaces or speed control for windmills. However, the development of the real industry was realized with the invention of steam engines and the industrial revolution took place. The widespread use of variables such as pressure, temperature, mixing, amount, flow rate and level in tank systems used in industrial processes, especially in sectors such as drink, beverage, chemistry, pharmaceutical and petroleum, has made it important to control. Many studies on this topic have been undertaken in recent years [32, 33]. Mizumoto et al. have proposed employing a PID controller design to control the tank liquid system [34]. Taler et al. have put forward and applied a method to control the hot fluid with PID [35]. Samin et al. realized the control of the liquid tank system with PID with PLC. At the conclusion of the research, the values for different parameters were compared and interpreted [36]. Fatih et al. have used to genetic algorithm to determine PID and LQR for controlling of level of the liquid tank system [37]. Selamet et al. have implemented the control of the liquid tank system with the most optimal controller parameters by using the PSO algorithm to specify the parameters of the PID and LQR methods [38]. Sastry et al. have performed the control of the single tank system using a nonlinear PID controller [39]. Kum et al. have carried out the tank system with a sliding mode controller. Wei et al. have realized the control of the liquid tank system with the back-stepping method [40]. Xiao et al. have used fuzzy logic in the control of the tank system in their study. In their study, fuzzy logic can adapt the PID controller. They have obtained successful results [41]. Esakkiappan, on the other hand, has performed the control of the liquid tank system with the PI controller they designed with cuckoo optimization [42]. Then, Son performed the control of the tank system using an adaptive inverse evolutionary algorithm [43]. Urrea et al. Again, using the liquid tank system with PID, Gain Scheduling, Internal Mode Control and fuzzy logic, they have implemented the control of the system comparatively and presented the results [44].

Essentially, in this study, a nonlinear system is controlled using classical controllers and reinforcement learning techniques. In particular, the single-level tank system was controlled using a modified PI controller as well as the classic PI controller. In addition, using the linearized model, the design and control of the State feedback controller with an integrator has been carried out. Finally, the control of the liquid tank system was carried out using SARSA (State-action-reward-state-action) and Q learning methods. The obtained results have been compared with respect to ISE (Integral square error) performance value and overshoot and settling time. In addition, learning-based SARSA and Q learning methods have been compared with regard to performance criteria and control signals. It has seen that Q learning algorithm produced better results.

The main contributions of this paper are as follows:

- PI, Modified PI and State Feedback with integral action controller have been designed to control the single tank liquid system.
- SARSA and Q Learning Methods are applied to control the single tank liquid system.

In this study, the first part of the content is the

introduction and information about artificial intelligence, reinforcement learning, tank system and control, and a literature review have been given. In Section 2, there is the Material and Method section, the methods realized in the study have been explained and the designs for the system have been made. Section 3 is the result and the control of the single-level tank system and the results obtained are demonstrated by comparing them in tables and graphics. Chapter 4 is the conclusion and the results are evaluated.

2. Materials and Methods

In reinforcement learning, there are two main system blocks seen in Figure 1. One of these blocks is an agent and the other is an environment. The agent's learning and recognition of the environment via interactions with it, and the experiences that have been obtained as a result of these interactions with the environment, recognizes the environment and begins to respond in a way that achieves the maximum reward it aims [7, 10, 15, 27, 30]. In this method, the agent constantly tries to learn the environment and thus develops the next step.

$$Q(s_t, a_t) = Q(s_t, a_t) + \alpha \left[R(s_t, a_t) + \gamma \max_a Q(s_{t+1}, a) - Q(s_t, a_t) \right] \quad (1)$$

In addition, the epsilon greedy method is applied to determine the q values [45]. This method allows the agent to visit all possible states during learning. Thus, the agent acquires better knowledge of the environment and determines the q values that can maximize the reward. The pseudocode of Q learning has been presented in Algorithm 1. This is an off-policy strategy in which the learning agent learns the value function depending on the current action obtained from the policy currently in use [28].

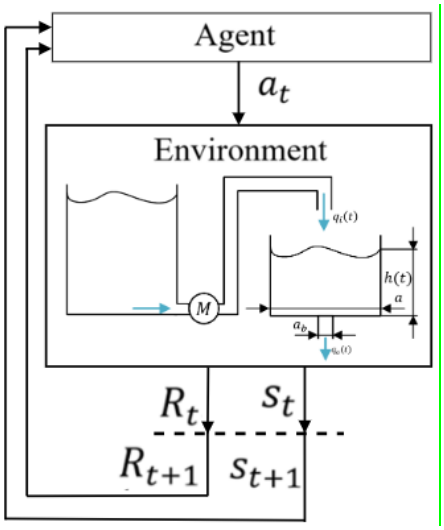

Figure 1. Interaction between Agent and Single Level Tank System Environment.

Algorithm 1 . Q learning Pseudo code.

Input:
State (s)
Action (a_t)
Learning rate (α)
Discount factor (γ)
Reward $R(s_t, a_t)$
Updated table $Q(s_t, a_t)$
Output:
Selected action according to updating table $Q(s_t, a_t)$
For episode 1, $Iter_{max}$ **do**
Initialise state s_t
$done = FALSE$
While $done == FALSE$
Choose a_t with ϵ greedy probability
Execute a_t and observe state s_{t+1}, reward r_t and $done$
Update table using Equation 1
End While
End For

2.1. Q learning Algorithm

Q learning method and SARSA methods are model-independent or model-free reinforcement learning methods. Reinforcement learning also has a feature that learns more from behavior. This occurs during an agent's interaction with the environment. Agent, which is being learned, interacts with environment and evaluates the outputs of the environment to produce an output called a reward [31-32, 50–52]. The agent learns the environment and begins to operate in a way that receives a better reward at each step based on the agent's current state, interaction with environment, and agent's next state. It can be preferred in applications that are difficult to model, especially since they can learn by experiencing the results of actions rather than the model. Especially with the Bellman equation that Richard Bellman recommends, and Watkin uses in reinforcement learning, it is provided to learn the actions and outputs performed depending on the situations. In this learning method, the system is learned in terms of situations and action and reward value rather than a specific model. The simplest version of the Bellman equation used in Q learning is given in Equation 1. Equation 1 used s_t, state at time t, action a_t at time t, s_{t+1} state at time t+1, $R(s_t, a_t)$ reward value at s_t and a_t, $Q(s_t, a_t)$ state of being value at s_t and a_t, α learning factor, and γ discount factor. $\max_{\alpha}\left(Q(s_{t+1}, a_{t+1})\right)$ is the value at which the maximum q value is produced according to the action α in the case of s_{t+1}. In each iteration, this operation is performed, and the q values are updated

2.2. SARSA Algorithm

SARSA, which is a method used in learning Markovinian processes, is a method used in reinforcement learning in machine learning. This method was proposed by Rumble and Niranjan as an alternative to the Q learning algorithm [46]. This method is an on-policy and the learning agent tries to learn the value function depending on the action derived from another policy [28]. That is, it does not need to be a value generated from within itself. The equation used in SARSA is given in Equation 2. The notations s_t, a_t, s_{t+1}, $R(s_t, a_t)$, $Q(s_t, a_t)$, α, γ, which has been used in Equation 1, is the same as the Q learning algorithm. There is only a single difference: the value of $Q(s_{t+1}, a_{t+1})$ represents the Q value obtained when the action a_{t+1} is applied in the case of s_{t+1}. For this value to be produced, the algorithm's action must be applied once, and the Q value produced by this applied action must be determined. In the SARSA algorithm, each action is applied to the a_t system, and $R(s_t, a_t)$ and $Q(s_{t+1}, a_{t+1})$ are determined and $Q(s_t, a_t)$ values are updated. The psoudecode of the SARSA algorithm is given in Algorithm 2.

$$Q(s_t, a_t) = Q(s_t, a_t) + \alpha[R(s_t, a_t) + \gamma Q(s_{t+1}, a_{t+1}) - Q(s_t, a_t)] \quad (2)$$

Algorithm 2. SARSA Pseudo code.

Input:
State (s)
Action (a_t)
Learning rate (α)
Discount factor (γ)
Reward $R(s_t, a_t)$
Updated table $Q(s_t, a_t)$
Output:
Selected action according to updating table $Q(s_t, a_t)$
For episode 1, $Iter_{max}$ **do**
Initialise state s_t
$done = FALSE$
While $done == FALSE$
Choose a_t with ϵ greedy probability
Execute a_t and observe state s_{t+1}, reward r_t and $done$
Choose a_{t+1} with ϵ greedy probability using state s_{t+1} from Q
Update table using Equation 2
End While
End For

2.3. Single Tank Liquid Level System

Single tank liquid level system, which is a very common system in the industry, is widely used in process control [37, 49]. It is mostly encountered in places where liquid filling and discharge are made such as medicine, food, and agriculture. In Figure 1, the structure of the tank level system is demonstrated. There is a main tank, motor and discharge tank in the system in Figure 1. Liquid level in the discharge tank is tried to be controlled by controlling a motor connected to the main tank. So, a single tank liquid level system has a single input which is the motor and a single output that is liquid level. There are parameters used in the single tank liquid level system, surface area of the tank a, the surface area of the outlet of the discharge tank a_b, and the velocity coefficient c_{db}, which differs due to the outlet structure for fluid [50]. The modeling of the single liquid tank system is presented in equation 3 $q_i(t)$ is the fluid's flow rate sent by the engine into the discharge tank, $q_o(t)$ is fluid's flow rate leaving the discharge tank, and $h(t)$ is the liquid's height in the discharge of tank. Consequently, the fluid supplied by the engine is the system's input, and the fluid's height in the discharge tank is the system's output.

$$q_i(t) - q_o(t) = a\frac{dh(t)}{dt} \quad (3)$$

$$q_o(t) = c_{db}a_b\sqrt{2gh(t)} \quad (4)$$

In Table 1, the parameters of the Single Tank Liquid Level System have been displayed.

Table 1. Parameters of Single Tank Liquid Level System.

Parameters	Unit	Value
c_{db}	-	0.62
a_b	m^2	0.00314
a	m^2	0.00314
g	m/s^2	9.81

After the values of the parameter of the system have been substituted in their place, the nonlinear model becomes like as in Equation 5. Then, Equation 6 is obtained by editing Equation 5. After that, Equation 7 is obtained when the $x(t)$ control sign is written instead of $h(t)$ height variable and the $u(t)$ control signal is written instead of $q_i(t)$. Controller design will be realized by linearizing this equation at a certain point.

$$\frac{dh(t)}{dt} = 31.847q_i(t) - 0{,}62\sqrt{2 \times 9.81 \times h(t)} \quad (5)$$

$$\dot{h}(t) = -2.746\sqrt{h(t)} + 31.847q_i(t) \quad (6)$$

$$\dot{x}(t) = -2.746\sqrt{x(t)} + 31.847u(t)$$
$$y = x(t) \quad (7)$$

For linearization, by making $\dot{x}(t) = f(x, u)$ the linear model for a single tank liquid level system has been

calculated according to the equilibrium point $x_0 = 1, u_0 = 1$. For this, in the linearization of the state, Equation 8 is first made and linearization is performed around the equilibrium point. Then the values of x_0 and u_0 are written in place to get Equation 9. Equation 10 is obtained when the mathematical operations in Equation 9 are performed. Equation 11 is obtained when this expression in the time dimension is moved to the Laplace dimension. After that, by using the output-to-input ratio to determine the system's transfer function, Equation 12 is obtained.

$$\begin{aligned}\Delta\dot{x}(t) &= \frac{df(x,u)}{dx}\Big|_{x=x_0}\Delta x(t) \\ &\quad + \frac{df(x,u)}{du}\Big|_{u=u_0}\Delta u(t) \\ y &= \Delta x(t) + x(t)\end{aligned} \tag{8}$$

$$\begin{aligned}\Delta\dot{x}(t) &= -2.746\left(\frac{1}{2}(x_0)^{-0.5}\right)\Delta x(t) \\ &\quad + 31.847\Delta u(t) \\ y &= \Delta x(t) + x(t)\end{aligned} \tag{9}$$

$$\begin{aligned}\Delta\dot{x}(t) &= -1.373\Delta x(t) + 31.847\Delta u(t) \\ y &= \Delta x(t) + x(t)\end{aligned} \tag{10}$$

$$s\Delta x(s) = -1.373\Delta x(s) + 31.847\Delta u(s) \tag{11}$$

$$G(s) = \frac{\Delta x(s)}{\Delta u(s)} = \frac{31.847}{s + 1.373} \tag{12}$$

2.4. PI and Modified PI

The transfer function of a single tank liquid level system has been obtained in Equation 12. When the PI controller has been designed according to Zeigler Nichol's step response for this system, the obtained controller has is given in Equation 13.

$$PI(s) = K_p + K_i\frac{1}{s} = 0.3887 + 2.9905\frac{1}{s} \tag{13}$$

Since this tank system has been controlled in discrete time, the controller has to be discretized for the system to be implemented. The discrete structure of the discretized controller at T=0.05 sec has been obtained as $PI(z) = \frac{19{,}82z - 7.43}{z-1}$. Then by using this controller, controlling of single-level tank system has been conducted by using PI as in Figure 2 and modified PI as in Figure 3.

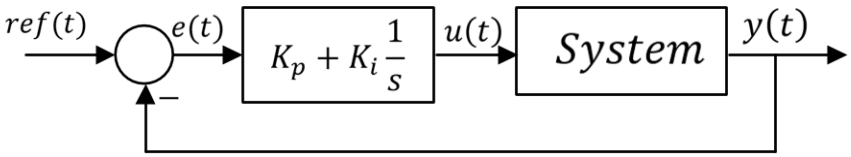

Figure 2. Control Structure with Single Tank Liquid Level System with PI.

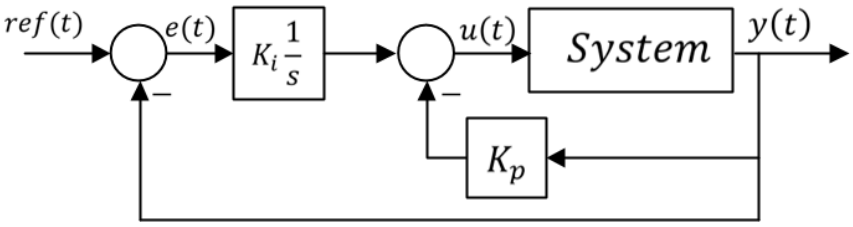

Figure 3. Single Tank Liquid Level System Control Structure with Modified PI.

2.5. State Feedback Controller Design

State feedback controllers with integral action have been designed for tank system control, and the tank system has been controlled. The structure of state feedback with integral action has been demonstrated in Figure 4. The controller has been realized by adding an integral action to a system in the structure designed in the state space. By adding an integrator to controller, steady state error between reference and system response would be eliminated. In Figure 4, each signal namely error $(e(t))$, control signal $(u(t))$, and state of the system $(\dot{x}(t))$ is designed step by step as in Equation 14. As a result, and augmented state space containing the state of the system $(\dot{x}(t))$ and integral of the error $(\dot{x}_i(t))$ is obtained in Equation 15. In Equation 15, the Control signal of the system has become $ref(t)$ in the augmented state. After the parameters of the tank system are substituted in their place, the structure of the system's model to be utilized in the design has been obtained in Equation 16.

$$e(t) = r(t) - y(t) = r(t) - Cx(t)$$
$$e(t) = \dot{x}_i = e(t) = r(t) - y(t) = r(t) - Cx(t)$$
$$u(t) = x_i - Kx(t)$$
$$\dot{x}(t) = Ax(t) + Bu(t) \quad (14)$$
$$\dot{x}(t) = Ax(t) + B\big(x_i - Kx(t)\big)$$
$$\dot{x}(t) = (A - BK)x(t) + Bx_i$$

$$\begin{bmatrix}\dot{x}(t)\\ \dot{x}_i(t)\end{bmatrix} = \begin{bmatrix}A - BK & B\\ -C & 0\end{bmatrix}\begin{bmatrix}x(t)\\ x_i(t)\end{bmatrix} + \begin{bmatrix}0\\ 1\end{bmatrix} ref(t) \quad (15)$$

$$\begin{bmatrix}\Delta\dot{x}(t)\\ \dot{x}_i(t)\end{bmatrix} = \underbrace{\begin{bmatrix}-1{,}373 - 31{,}847K & 31{,}847\\ -1 & 0\end{bmatrix}}_{A_{cl}}\begin{bmatrix}\Delta x(t)\\ x_i(t)\end{bmatrix} + \begin{bmatrix}0\\ 1\end{bmatrix} ref(t) \quad (16)$$

The system matrix of the system in which pole placement will be made is $A = -\frac{\sqrt{2\times 9.81}}{2}$. B=1 is taken as C=1. The pole's place of the tank system will be determined with respect to the K parameter. But the value of K parameter will be determined with respect to places of the poles of the tank system. Then, the closed loop characteristic equation is obtained as $det(Is - A_{cl}) = \big(s - (A - BK)\big)(s) + BC = \big(s - (-1{,}373 - 31{,}847K)\big)(s) + 31{,}847$. When this equation is expanded, it is arranged as $det(Is - A_{cl}) = s^2 + (s + 1{,}373 + 31{,}847K)s + 31{,}847$. Normally the characteristic equation of the second order system is $s^2 + 2\zeta w_n s + w_n^2 = 0$. When these equations are equalized, the natural frequency of the system becomes $w_n = 5{,}643$. For the design, the $T_{settling}$ value was chosen as 1 sec, 20 times the sampling time. For this design, the damping coefficient of the system becomes $T_{settling} = \frac{4}{\zeta w_n} = 1sec \rightarrow \zeta w_n = 4$. In the characteristic equation, $\zeta = 0{,}708$ is obtained from the equation $1{,}373 + 31{,}847K = 2\zeta w_n = 8 \rightarrow K = 0.208$ =2. Since $0 < \zeta < 1$, the system will be controlled as oscillating damped.

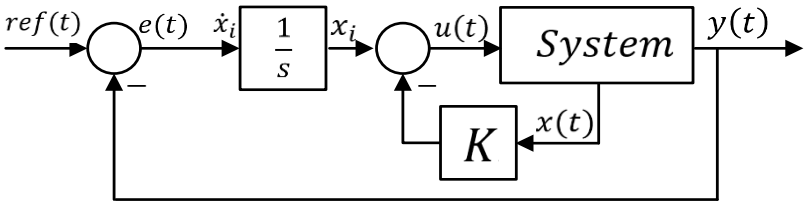

Figure 4. Control Structure with Single Tank Liquid Level System integrator with state feedback.

2.6. Adaptation of Single Tank Liquid Level System to Q Learning and SARSA Controller

When the single-tank system is considered an environment for reinforcement learning, expressions or symbols could be matched each other. For instance, action a(t) applied to the system, that is control signal u(t) or states s_t of Q learning and SARSA might be matched to the states of the system to be controlled. Therefore, the states are given in Equation 17 so that the method can be applied to algorithms. In addition, the reward function obtained from the environment is specified in Equation 18. Nevertheless, it is useful to know that these states and reward functions could be changed as to designer.

$$s(t) = \big(ref, x(t)\big) \quad (17)$$

$$reward = \begin{cases} 15 - 200 \times |ref - x(t)| - a(t)^2 & |ref - x(t)| \\ 5 - 200 \times |ref - x(t)| - a(t)^2 & other \end{cases} \quad (18)$$

Due to the controller running on the Q table, the Q table of the system was created according to the actions and states. The reference range was chosen between [0,5] and increased in steps at certain step lengths. $x(t)$ state is selected between [0,2] and increased with a certain step length and the q table is created. A small part of the created table is presented in Table 2. At first, before the learning process, a 0 value was assigned to all variables of the Q table. As seen in Table 2, some values are still 0 as seen in the Q table of the agent trained for 200000 steps. Therefore, the agent recognizing the environment shows that it does not undergo every state, that is, not every state occurs in the environment. In addition, in Table 3, common parameters for SARSA and Q learning have been presented. Also, the maximum number of iterations ($Iter_{max}$) for which the algorithms are run is. The parameters of the ε variable used in the epsilon greedy algorithm are presented in Table 3 as the initial value (ε_{start}), the decreased value ($\varepsilon_{decrement}$) and the minimum value (ε_{min}). In addition, the minimum($ref_{min}, x(t)_{min}$), maximum ($ref_{max}, x(t)_{max}$) and step lengths $\big(ref_{step\ size}, x(t)_{step\ size}\big)$ of discretized $ref(t)$ and $x(t)$ state values have been presented in Table 3. Reward values of Q learning and SARSA algorithm trained to control the single-level tank system are given in Figure 5 by plotting according to iterations. In the beginning, it could be seen that the reward value fluctuated and then increased due to the epsilon decreased in the greedy algorithm during iteration. At last, reward values have been fixed in both algorithms.

Table 2. A sample Q table with Q learning trained over 200000 iterations for controlling the Single Tank Liquid Level System.

State		Action				
$ref(t), x(t)$		0	0.05	0.1	7.95	8
Real	Discrete					
$0, -0.1$	$0, 0$	0	0	0	0	0
$0, -0.079$	$0, 1$	0	0	0	0	0
0.1,0.005	$0, 5$	-115.91	74.56	97.84	-550165.34	-539846.01
0.1,0.026	$1, 6$	0	0	0	0	0
0.1,0.047	1,7	0	0	0	0	0
0.3,0.383	3,23	349.43	-0.13	-0.31	-3215.11	-3184.24
0.3,0.425	3,24	345.86	-0.58	-0.57	-3223.79	-3268.76
0.8,0.782	8,42	13.13	18.39	23.42	-3653.06	-2483.30
0.8,0.782	8,43	-0.56	-0.39	-0.32	0	0
0.9,0.782	9,43	0	0	0	0	0
0.9,0.782	8,43	-0.56	-0.39	-0.32	0	0

Table 3. Parameters for SARSA and Q learning.

Parameters	Value
$Iter_{max}$	195000
ε_{start}	1.0
ε_{min}	0.001
$\varepsilon_{decrement}$	$\varepsilon_{start}/Iter_{max}$
ref_{min}	0.
ref_{max}	5
$ref_{step\ size}$	0.1
x_{min}	-0.1
x_{max}	2.0
$x_{step\ size}$	0.0209

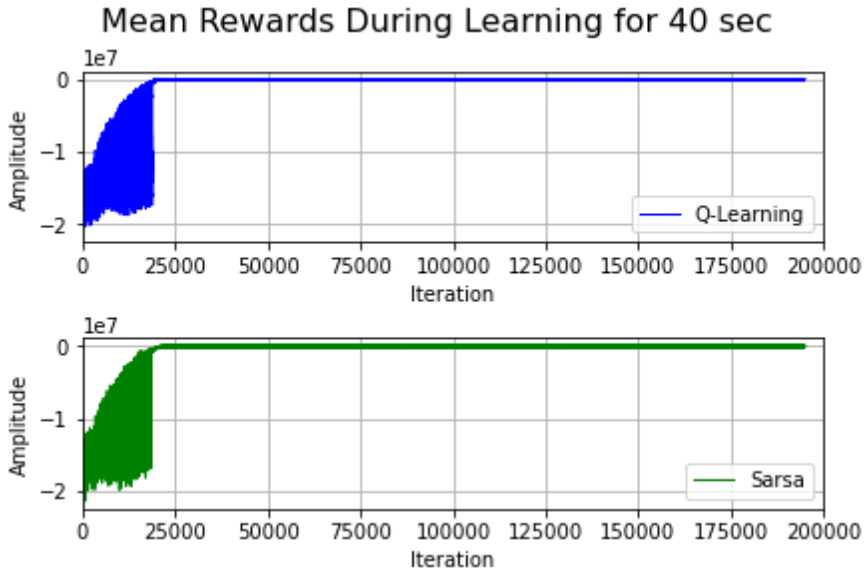

Figure 5. Reward values of Single Tank Liquid Level System by PI, modified PI, state feedback with integral action, Q Learning and SARSA.

3. Simulation Results

The simulation studies carried out in this study have been conducted on a computer with Intel(R) Core (TM) i5-9400 CPU @ 2.90GHz, 64-bit, 8GB RAM. The software language in which the study is carried out is Python and the interface is the Anaconda program. The single-level tank system to be controlled has been built as an environment in this program. Then, the designs were made to control the system with PI, modified PI, state feedback with integral action, Q learning and SARSA. After that system cosntrol has been carried out, and then the results have been obtained. The results obtained have been presented in the table in terms of performance values. In addition, the results obtained in terms of system response and control responses have been given in graphics.

The results of the single-level liquid tank system controlled by PI, modified PI, state feedback, Q learning and SARSA methods were evaluated in terms of T_{rising}, $T_{settling}$, overshoot and ISE performance criteria. The numerical results, in Table 4, for single-level liquid tank system have been demonstrated. The best results among methods are written in bold. When the results are examined, the Q learning algorithm has produced better results than the others with regard to T_{rising}, $T_{settling}$ and ISE. However, when examined in terms of overshoot, it can be seen that SARSA algorithm indicated better results than classical controllers and the Q learning methods. In addition, the step response graph, control signal and reward values of the controlled system have been depicted in graphics. In Figure 6, system responses of the single-level tank system to the step reference input have been depicted. When the responses of the Q learning and SARSA methods have been examined, it can be noticed that although the system has reached the desired reference value faster, it has not remained at the desired reference value or have fluctuated in its responses compared to the classical control methods, that is, it has deviated and come back again. The prime cause for this is that the system is continuous and the controller that controls the system is discretized according to certain step lengths. In addition, control signs have been depicted in Figure 7. Fluctuating in the control signal could be seen more easily. Another reason could be that there is epsilon greedy in the structure that controls the system in Q learning and SARSA algorithms. This method, which is used for discovery, could sometimes lead to the selection of a different control signal within the solution pool. On the other hand, the reward values, that have been obtained after the single tank liquid level system have been controlled, have been indicated in Figure 8 according to time.

Table 4. Performance results of controlling Single Tank Liquid Level System

	T_{rising} (sec)	$T_{settling}$ (sec)	$Overshoot$	ISE
PI	0.0875	0.4283	%25,40	0,1968
Modifiye PI	0.1676	0.5035	%11.36	0.1168
State Feedback	0,4167	0.8180	%6,10	0.2893
Q learning	**0.0804**	**0,0943**	%1,2	**0.0574**
Sarsa	0.0874	0.0943	**%0,7**	0,0590

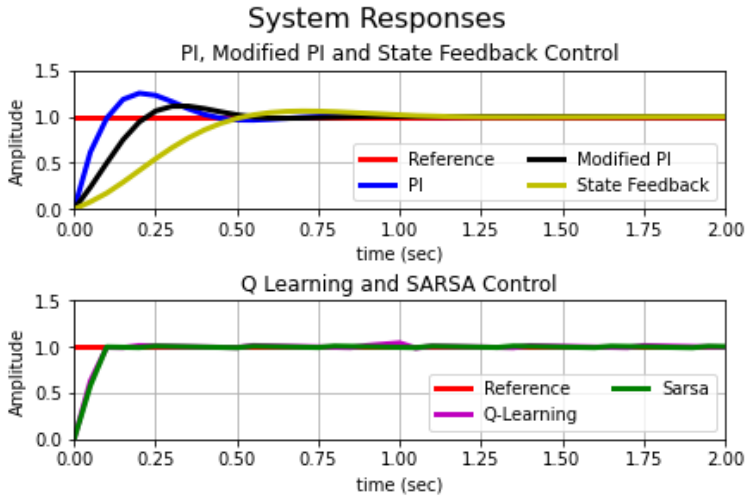

Figure 6. System responses of single tank liquid level System by PI, modified PI, state feedback with integral action, Q Learning and SARSA.

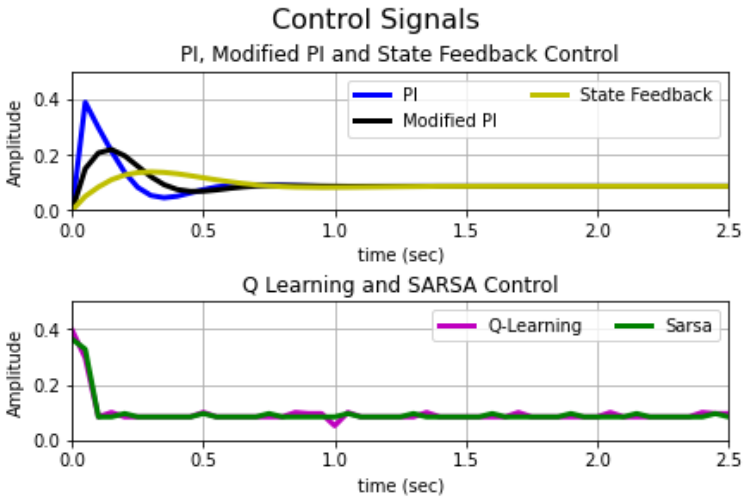

Figure 7. Control signals of Single Tank Liquid Level System by PI, modified PI, state feedback with integral action, Q Learning and SARSA.

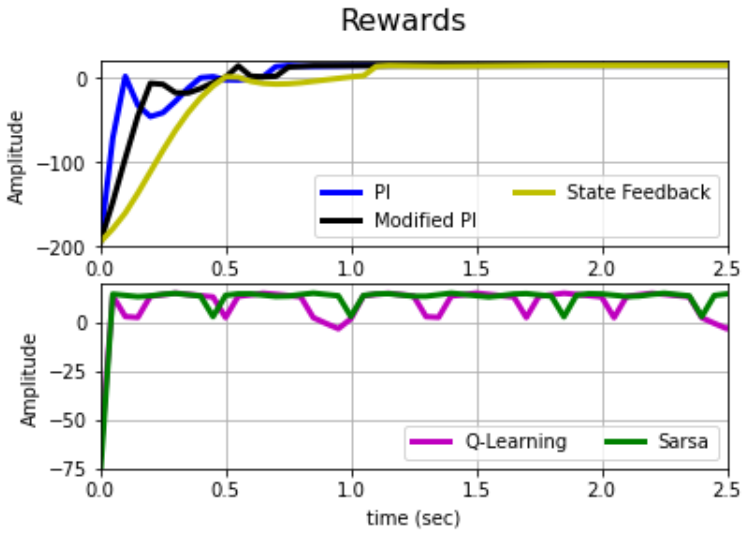

Figure 8. Reward values of Single Tank Liquid Level System by PI, modified PI, state feedback with integral action, Q Learning and SARSA.

The system has been controlled at several reference values in order to better see the performances of controllers for the Single Tank Liquid Level System. As can be seen, Q learning and SARSA methods have generally produced faster results than PI, Modified PI and State Feedback with integral action. However, looking at results for SARSA, it can be noticed that there are chattering or fluctuations when the reference value is 0.5. To prevent this, agents could be trained more or the size of Q table would be increased by reducing the step lengths of the states while creating the Q table. However, the decrease in step length is a tradeoff that increases memory and processing load. In this study, since the Q learning and SARSA methods work discrete, system response and control signal can be aggressive when step length is large. In addition, since it is operated discretely, the performances of the controllers may vary at reference signals at different points. The biggest constraint at this point is memory and processing time. However, in future studies, soft actor-critic, deep q learning, double deep q learning methods that work continuously with artificial neural networks will be used to overcome memory size constraints.

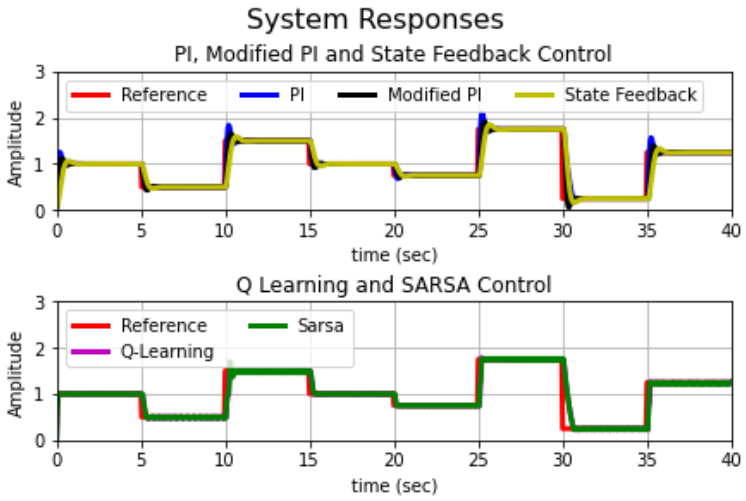

Figure 9. System responses of Single Tank Liquid Level System by PI, modified PI, state feedback with integral action, Q Learning and SARSA for different reference signals.

4. Conclusions

In this study, classical and reinforcement learning-based controllers have been designed to control the nonlinear single-level tank system. First, the system has been linearized and the PI controller has been designed with the classical Ziegler Nichols method. Then, Modified PI has been applied and state feedback with integral action controllers were designed with pole assignment. Then, agents have been trained for SARSA and Q learning algorithms on the Single Tank Liquid Level System which is an environment and also this is a nonlinear system. After that, trained agents have applied to the system to be controlled. The results of the nonlinear single-level liquid tank system controlled by these methods have been assessed about rising time (T_{rising}), settling time ($T_{settling}$), overshoot and ISE performance indexes. When the results have been examined, it can be noticed that the Q learning algorithm has produced better results with regard to rise time (T_{rising}), settling time ($T_{settling}$) and ISE. Furthermore, it has been noticed and concluded that, due to SARSA and the Q learning used in the study being discrete, there might be memory size difficulty that caused chattering or fluctuating problems of system responses in this method. In future studies, softened control signals could be improved in transitions between states, and deep learning-based reinforcement learning methods, which are popular topics, are going to be used.

Declaration of Ethical Standards

If the study does not require an Ethics Approval, the following declaration can be used:

"The author(s) of this article declare that the materials and methods used in this study do not require ethical committee permission and/or legal-special permission."

Otherwise, please declare the board name granting ethics approval, approval date and approval number.

Conflict of Interest

All conflicts of interest should be declared. If there is not any conflict of interest, the content of this section can be arranged as follows.

"The authors declare that they have no known competing financial interests or personal relationships that could have appeared to influence the work reported in this paper."

Acknowledgements

Acknowledgements should be expressed in a separate section before the references.

References

[1] M. A. Pala, M. E. Çimen, Ö. F. Boyraz, M. Z. Yildiz, and A. Boz, 2019. Meme Kanserinin Teşhis Edilmesinde Karar Ağacı Ve KNN Algoritmalarının Karşılaştırmalı Başarım Analizi. *Acad. Perspect. Procedia*, **2**(3). doi: 10.33793/acperpro.02.03.47.

[2] S. Tajjour, S. Garg, S. S. Chandel, and D. Sharma, 2023. A novel hybrid artificial neural network technique for the early skin cancer diagnosis using color space conversions of original images. *Int. J. Imaging Syst. Technol.*, **33**(1), pp. 276–286.

[3] D. Şengür, 2021. EEG, EMG and ECG based determination of psychosocial risk levels in teachers

based on wavelet extreme learning machine autoencoders. *Politek. Derg.*, **25**(3), pp. 85–989, 2021, doi: 10.2339/politeknik.886593.

[4] F. Bayram, 2020. "Derin öğrenme tabanlı otomatik plaka tanıma," *Politek. Derg.*, **23**(4), pp. 955–960.

[5] J. Lisowski, 2023. Artificial Intelligence Methods in Safe Ship Control Based on Marine Environment Remote Sensing. *Remote Sens.*, **15**(1), p. 203. doi: https://doi.org/10.3390/rs15010203.

[6] A. Kurani, P. Doshi, A. Vakharia, and M. Shah, "A comprehensive comparative study of artificial neural network (ANN) and support vector machines (SVM) on stock forecasting," *Ann. Data Sci.*, vol. 10, no. 1, pp. 183–208, 2023, doi: https://doi.org/10.1007/s40745-021-00344-x.

[7] M. S. Ünlü, "Teknik Analiz Ve Derin Pekiştirmeli Öğrenme İle Kriptopara Alım-Satımı," Okan Üniversitesi, 2019.

[8] X. Huang, D. Zou, G. Cheng, X. Chen, and H. Xie, "Trends, research issues and applications of artificial intelligence in language education," *Educ. Technol. Soc.*, vol. 26, no. 1, pp. 112–131, 2023, doi: 10.30191/ETS.202301_26(1).0009.

[9] K. Souchleris and G. A. Sidiropoulos, G. K. Papakostas, "Reinforcement Learning in Game Industry—Review, Prospects and Challenges," *Appl. Sci.*, vol. 13, no. 4, p. 2443, 2023, doi: 10.3390/app13042443.

[10] F. Candan, S. Emir, M. Doğan, and T. Kumbasar, "Takviyeli Q-Öğrenme Yöntemiyle Labirent Problemi Çözümü Labyrinth Problem Solution with Reinforcement Q-Learning Method," in *TOK2018 Otomatik Kontrol Ulusal Toplantısı*, 2048.

[11] G. Mbuwir, B., Ruelens, F., Spiessens, F., & Deconinck, "Reinforcement learning-based battery energy management in a solar microgrid," *Energy-Open*, vol. 2, no. 4, p. 36, 2017.

[12] M. Harmon and S. Harmon, "Reinforcement Learning: A Tutorial," 1997. [Online]. Available: https://apps.dtic.mil/sti/pdfs/ADA323194.pdf

[13] S. A. Ğ. Reyhan and Z. H. Tuğcu, "Akıllı Şebeke Uygulamalarında Derin Öğrenme Tekniklerinin Kullanımına İlişkin Kısa Bir İnceleme," *EMO Bilim. Dergi*, vol. 13, no. 1, pp. 41–61, 2022, [Online]. Available: https://dergipark.org.tr/en/pub/emobd/issue/75563/1196333

[14] I. Tunc and M. T. Soylemez, "Fuzzy logic and deep Q learning based control for traffic lights," *Alexandria Eng. J.*, vol. 67, pp. 343–359, 2023, doi: 10.1016/j.aej.2022.12.028.

[15] A. Leite, M. Candadai, and E. J. Izquierdo, "Reinforcement learning beyond the Bellman equation: Exploring critic objectives using evolution," in *Artificial Life Conference Proceedings 32*, 2020, pp. 441–449.

[16] I. C. Dolcetta and M. Falcone, "Discrete dynamic programming and viscosity solutions of the Bellman equation," in *In Annales de l'Institut Henri Poincaré C, Analyse non linéaire*, 1989, pp. 161–183.

[17] C. Boutilier, R. Reiter, and B. Price, "Symbolic dynamic programming for first-order MDPs," in *IJCAI International Joint Conference on Artificial Intelligence*, 2001, vol. 1, pp. 690–697. doi: 10.1609/aaai.v24i1.7747.

[18] W. B. Powell, *Approximate Dynamic Programming: Solving the curses of dimensionality*. John Wiley, 2007.

[19] D. Michie, "Experiments on the mechanization of game-learning Part I. Characterization of the model and its parameters," *Comput. J.*, vol. 6, no. 3, pp. 232–236, 1963.

[20] M. L. Minsky, *Theory of neural-analog reinforcement systems and its application to the brain-model problem*. Princeton University, 1954.

[21] J. Karlsson, "Learning to solve multiple goals," University of Rochester, 1997.

[22] A. L. Samuel, "Some studies in machine learning using the game of checkers. II—Recent progress," *Annu. Rev. Autom. Program.*, vol. 6, pp. 1–36, 1969.

[23] C. J. C. H. Watkins, "Learning from delayed rewards," King's College UK, 1989.

[24] C. J. Watkins and P. Dayan, "Q-learning," *Mach. Learn.*, vol. 8, pp. 279–292, 1992.

[25] G. Tesauro, "Neurogammon: A neural-network backgammon program," in *JCNN international joint conference on neural networks IEE*, 1990, pp. 33–39. doi: 10.1109/IJCNN.1990.137821.

[26] G. Tesauro, "Practical issues in temporal difference learning," *Adv. neural Inf. Process. Syst.*, vol. 4, 1991.

[27] C. Ozan, "İyileştirilmiş pekiştirmeli öğrenme yöntemi ve dinamik yükleme ile kentiçi ulaşım ağlarının tasarımı," Pamukkale Üniversitesi, 2012.

[28] M. K. Çalışır, S., & Pehlivanoğlu, "Model-free

reinforcement learning algorithms: A survey," in *27th Signal Processing and Communications Applications Conference (SIU)*, 2019, pp. 1–4.

[29] A. O. Köroğlu, A. E. Edem, S. N. Akmeşe, Ö. Elmas, I. Tunc, and M. T. Soylemez, "Agent-Based Route Planning with Deep Q Learning," in *13th International Conference on Electrical and Electronics Engineering (ELECO)*, 2021, pp. 403–407.

[30] Y. Li, "Deep reinforcement learning: An overview," *arXiv Prepr. arXiv1701.07274*, 2017, doi: https://doi.org/10.48550/arXiv.1701.07274.

[31] A. Bir and M. Kacar, *Pioneers of Automatic Control Systems*. 2006.

[32] M. E. Çimen, Z. Garip, M. Emekl, and A. F. Boz, "Fuzzy Logic PID Design using Genetic Algorithm under Overshoot Constrained Conditions for Heat Exchanger Control," *J. Inst. Sci. Technol.*, vol. 12, no. 1, pp. 164–181, 2022, doi: 10.21597/jist.980726.

[33] ME, Cimen, and Y. Yalçın, "A novel hybrid firefly–whale optimization algorithm and its application to optimization of MPC parameters," *Soft Comput.*, vol. 26, no. 4, pp. 1845–1872, 2022, doi: 10.1007/s00500-021-06441-6.

[34] Z. Mizumoto, I., Ikeda, D., Hirahata, T., & Iwai, "Design of discrete time adaptive PID control systems with parallel feedforward compensator," *Control Eng. Pract.*, vol. 18, no. 2, 2010, doi: https://doi.org/10.1016/j.conengprac.2009.09.003.

[35] D. Taler, T. Sobota, M. Jaremkiewicz, and J. Taler, "Control of the temperature in the hot liquid tank by using a digital PID controller considering the random errors of the thermometer indications," *Energy*, 2022, doi: https://doi.org/10.1016/j.energy.2021.122771.

[36] R. E. Samin, L. M. Jie, and M. A. Zawawi, "PID implementation of heating tank in mini automation plant using Programmable Logic Controller (PLC)," in *International Conference on Electrical, Control and Computer Engineering 2011 (InECCE)*, 2011.

[37] G. Yüksek, A. N. Mete, and A. Alkaya, "PID parametrelerinin LQR ve GA tabanlı optimizasyonu: sıvı seviye kontrol uygulaması," *Politek. Derg.*, vol. 23, no. 4, pp. 1111–1119, 2020, doi: 10.2339/politeknik.603344.

[38] N. A. Selamat, F. S. Daud, H. I. Jaafar, and N. H. Shamsudin, "Comparison of LQR and PID Controller Tuning Using PSO for Coupled Tank System," in *11th International Colloquium on Signal Processing & Its Applications (CSPA)*, 2015.

[39] D. Sastry, K. Mohan, M. Naidu, and N. M. Rao, "An Implementation of Different Non Linear PID Controllers on a Single Tank level Control using Matlab," *Int. J. Comput. Appl. (*, vol. 54, no. 1, 2012.

[40] and Y. S. Wei, Le, Fang Fang, "Adaptive backstepping-based composite nonlinear feedback water level control for the nuclear U-tube steam generator.," *IEEE Trans. Control Syst. Technol.*, vol. 22, no. 1, 2013, doi: 10.1109/TCST.2013.2250504.

[41] Q. Xiao, D. Zou, and P. Wei, "Fuzzy Adaptive PID Control Tank Level," in *International Conference on Multimedia Communications*, 2010. doi: 10.1109/MEDIACOM.2010.10.

[42] C. Esakkiappan, "Soft Computing Based Tuning of PI Controller With Cuckoo Search Optimization For Level Control of Hopper Tank System," *Res. Sq.*, 2021, doi: https://doi.org/10.21203/rs.3.rs-920228/v1.

[43] N. N. Son, "Level Control of Quadruple Tank System Based on Adaptive Inverse Evolutionary Neural Controller," *Int. J. Control. Autom. Syst.*, vol. 18, no. 9, 2020, doi: 10.1007/s12555-019-0504-8.

[44] C. Urrea and F. Páez, "Design and Comparison of Strategies for Level Control in a Nonlinear Tank," *Processes*, vol. 9, 2021, doi: 10.3390/pr9050735.

[45] R. S. Sutton and G. A. Barto, *Reinforcement Learning: An Introduction*. Cambridge: MIT Press, 1998.

[46] M. Rummery, G. A., & Niranjan, *On-line Q-learning using connectionist systems*. Cambridge, UK: University of Cambridge, 1994.

[47] C. J. Watkins and P. Dayan, "Q-Learning," *Mach. Learn.*, vol. 8, pp. 279–292, 1992, doi: 10.1007/BF00992698.

[48] A. Wang, H., Emmerich, M., & Plaat, "Monte Carlo Q-learning for General Game Playing," *arXiv Prepr. arXiv1802.05944.*, doi: 10.48550/arXiv.1802.05944.

[49] K. L., R. Bars, J. Hetthéssy, and C. Bányász, *Control Engineering*. Springer, 2019. doi: 10.1007/978-981-10-8297-9.

[50] J. Cimbala and Y. Cengel, *Fluid mechanics: fundamentals and applications*. McGraw-Hill Higher Education, 2006.

Koc. J. Sci. Eng., 7(1): (2024) 42-51 https://doi.org/10.34088/kojose.1295098

Kocaeli University

Kocaeli Journal of Science and Engineering

http://dergipark.org.tr/kojose

Topology Optimization of Structural Drive-Train Component of an Electric-Driven Vehicle for Additive Manufacturing

Ahmet Erkan KILIÇ [1], Atilla SAVAŞ [2,*], Yavuz YÜCESOY [3]

[1] *Department of Mechanical Engineering, Piri Reis University, İstanbul, 34940, Turkey,* ***ORCID:*** *0000-0002-5782-6132*
[2] *Department of Mechanical Engineering, Piri Reis University, İstanbul, 34940, Turkey,* ***ORCID:*** *0000-0001-6900-3259*
[3] *Department of Mechanical Engineering, Piri Reis University, İstanbul, 34940, Turkey,* ***ORCID:*** *0000-0002-9556-7872*

Article Info

Research paper

Received : *May 10, 2023*
Accepted : *October 10, 2023*

Keywords

Additive Manufacturing
Finite Element Analysis
Manufacturing
Topology Optimization

Abstract

Additive Manufacturing (AM) is an emerging technology and an important alternative to conventional manufacturing methods as it enables the production of lighter parts that are potentially more durable. In this context, the design for additive manufacturing (DFAM) has been drawing a considerable amount of attention mainly in the aerospace, and automotive industries as well as in academia. On the other hand, the ability of additive manufacturing to manufacture complex topology is often the outcome of topology optimization, which makes topology optimization a good design tool for additive manufacturing. The main objective of the present work is to redesign a structural component of the drivetrain of the Shell Eco-Marathon vehicle, with the use of Altair Inspire™, an industrial generative design tool, by application of Topology Optimization for Additive Manufacturing aiming mass reduction and does not cover the print process.

1. Introduction

Additive Manufacturing (AM) is a state-of-the-art method that brings a transformative approach to industrial production enabling the creation of lighter, potentially stronger parts. The design of lightweight structures via AM methods has been attracting a considerable amount of consideration in academia and industries for a wide range of applications.

However, the capability to additively manufacture complicated parts is the result of topology optimization (TO), which makes TO an excellent instrument for AM.
The additive behavior is opposed to material removal processes such as milling, cutting, drilling, etc. which start with a bulk of material and step by step remove the material to reach the final part" [1].

According to the American Society for Testing and Materials [1], AM is *"the process of joining materials to make objects from 3D model data, usually layer upon layer, as opposed to subtractive manufacturing methodologies."*

Different materials can be used in different AM technologies. AM machines and 3D printers can be easily used in the production of polymers, metals, ceramic materials, paper, wood, cork, foam, and rubber, including in layered manufacturing.

As AM technology develops further and the costs of 3D printed parts begin to decrease, AM and 3D printing will become the more widely used method. To make full use of this technology, ways to take advantage of one of its various advantages, the Topology Optimization technology, will be sought.[2].

When used together with machining methods, AM provides more flexibility to the designer, and the cost differences in producing complex parts are eliminated.

Thanks to the studies in Metallic AM in recent years, functional products have started to be used instead of prototypes. Industrialists seem very willing to take advantage of this. It does not seem logical to produce the existing design with the AM method. It is necessary to redesign the part to be produced and take advantage of TO.

* Corresponding Author: asavas@pirireis.edu.tr

The targets in production have led to the use of different optimization methods. Three types of optimization methods have been developed for production via the AM method:

Size optimization -

Shape optimization -

Topology optimization -

TO is an essential element in making the most of the features AM enables for design.

TO can roughly be separated into the management of two different types of domains: continuum and distinct structures. Distinct structures often refer to large constructions like bridges, cranes, and other truss structures, while continuum structures often refer to smaller, single-piece parts and components [3]

The most widely used software density-based TO method is also called SIMP (Solid Isotropic Material with Penalization method).

Plosher and Panesar made studies about design for Additive Manufacturing [4]. These authors stated that although AM design methods are widely used today, the numerical methods used for many engineering problems are still not widely used in the market.

Liu et al. He gave information about how to use the TO methods used before 3D printers and AM methods.[5].

Langelaar's work discusses the key features of an additive manufacturing process and a filter that can be used in density-based TO procedures.[6].

In the study carried out by Atzeni and Salmi, it is evaluated that the parts produced by the additive manufacturing method compete with the parts produced by machining and this causes production increases.[7].

Christiansen et al. stated that the optimized part uses only 20% of the material compared to machining.[8]. They utilized the DSC method (Deformable Simplicial Complex method). TO has proven to be a good technique for designing bone replacements [9]. Mezzadri et al. formulated the creation of support structures for AM as a TO problem [10]. Chu et al. utilized a SIMP-based method to cope with the TO of multi-material structures with cascading interfaces [11]. Zheng et al. suggested an orderly method to design robust multi-material parts under gap loading uncertainty [12].

The work presented by Xu et al. can be seen as a useful step towards a more realistic and comprehensive framework for integrating stress-constrained stiffness design and the topological design of geometrically nonlinear structures [13].

Liu et al. aimed to create a reliable topological design by considering local material uncertainties in their work [14]. Li et al. presented a meshless method that was developed for the TO problem of structures under multiple loading conditions [15]. Bi et al. presented a new method that can effectively address protruding features in the bi-directional evolutionary structural optimization framework [16].

A kind of derivative respirator was developed based on FDM (Fused Deposition Modeling) by Aydın et al. [17]. Çelebi and Tosun utilized the FDM method to produce a router and managed to save 60 percent of the volume and mass [18].

Shell Eco-Marathon is a worldwide competition for student teams which they participate with their vehicles. The competition aims to encourage students to design and manufacture their vehicles through high-tech and energy-efficient solutions.

The objective of Shell Eco-Marathon is to build the most energy-efficient car. Therefore, the weight of the car components is of critical importance.

In this present study, the electric motor bracket of an all-electric Shell Eco marathon vehicle has been redesigned for additive manufacturing with the use of Altair Inspire™, an industrial generative design tool, by application of Topology Optimization for Additive Manufacturing aiming mass reduction. The scope of the study is limited to the redesigning and does not cover the print process.

The results of finite element analysis that have been performed on the redesigned part show that the redesigned part is capable of withstanding applied loads while the part is in operation.

Moreover, a significant mass reduction is achieved with the redesigned model in comparison to the original model.

The method used by Christiansen et al. made only 20 percent of the material be used for production [8]. In our case, 89 percent scrap reduction is achieved which is a good result compared to the mentioned case.

2. Materials and Methods

2.1. Topology Optimization and Structural Modeling of The Part

The part considered for this work is an electric motor holder. For TO, Altair Inspire™ software was used.

The electric motor holder of an electric vehicle to be used in this study is shown in Figure 1.

The current, voltage, and similar values of the electric motor are given in Table 1. The torque and speed relations for the motor are depicted in Figure 2.

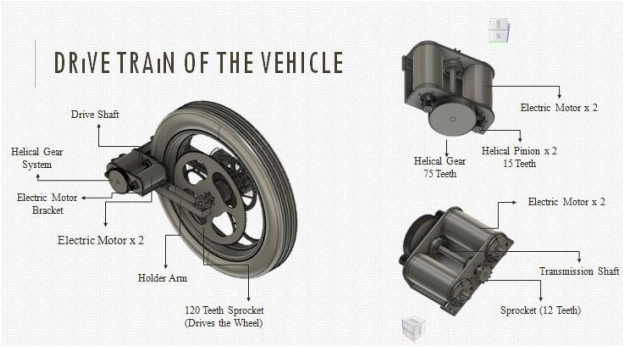

Figure 1. Electric motor, gearbox, transmission shaft, and electric motor holder [19]

Table 1. Technical data and specifications of the Direct Current Motor

Data	Value
Nominal Voltage	24 VDC
Nominal Current	10.8 A
Maximum Speed	9500 RPM (No Load)
Nominal Speed	5680 RPM
Maximum Efficiency	94%
Maximum Torque	8920 mN-m (Stall Torque)

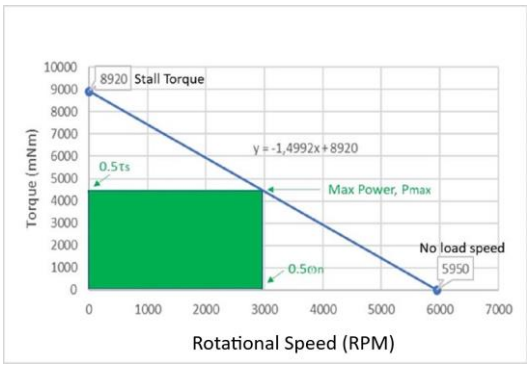

Figure 2. D.C. Motor Torque Speed Curve

2.2. Torque–Power Calculations

The Maximum Power is obtained at the mid-speed of the motor, 2975 RPM. The Torque at that speed is 4460 mNm.

Power is defined as:

$$P = T\omega \text{ [20]} \quad (1)$$

where P represents power in watts, T represents torque in N.m and ω represents the rotational speed in rad/s.

2.3. Transmission Specifications and Gear Force Analysis

The schematic diagram of the Gear Train (Transmission) is given in Figure 3.

Two pinions one for each Electric Motor drive the Gear. Data for the pinions and the gear are as follows:

Pinions: 15 teeth (Z_1) helical gears with 20° normal pressure angle (Φ_n), 1 mm normal module (m_n), and a helix angle of 20° (Ψ)

Gear: 75 teeth (Z_2) helical gear with 20° normal pressure angle (Φ_n), 1 mm normal module (m_n), and a helix angle of 20° (Ψ)

The formula given below can be utilized to compute the transverse pressure angle of a helical gear:

$$\tan\Phi_n = \tan\Phi\cos\Psi \quad (2)$$

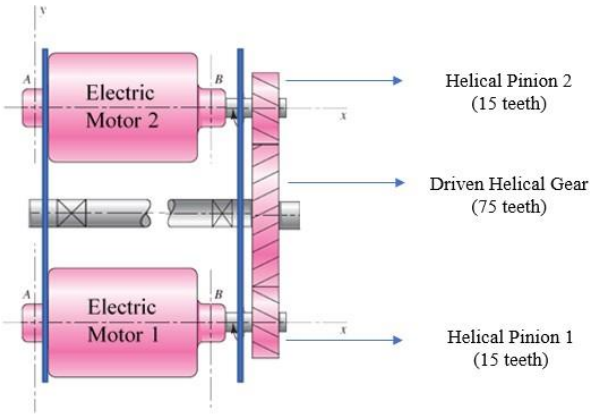

Figure 3. D.C. Motors and Gear Train [19]

The module for a helical gear is defined as:

$$m = m_n/\cos\Psi \quad (3)$$

The pitch diameter for helical gears is defined as:

$$d_1 = mZ_1 \quad \text{[20]} \quad (4)$$

Pitch line velocity for a helical gear is defined as:

$$V = \pi d_1 n_1/60 \quad [20] \tag{5}$$

As depicted in Figure 4, at the pitch point C of the pinion, the force Fr acts in the y-axis, Fa acts in the x-axis, and Ft acts in the z-axis.

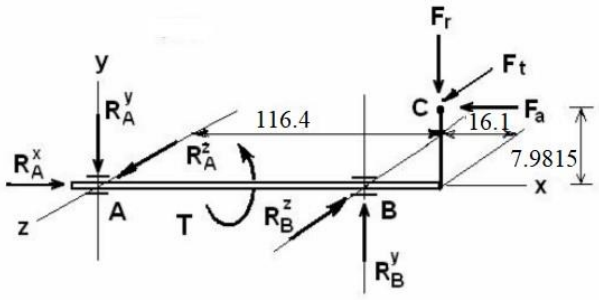

Figure 4. Diagram indicating the forces in action at the pitch point C of the pinion. [19]

Figure 5 illustrates the applied forces and the directions in which they act on Pinion-1 and the Driven Helical Gear, while Figure 6 presents the applied forces and their respective directions for Pinion-2 and the Driven Helical Gear.

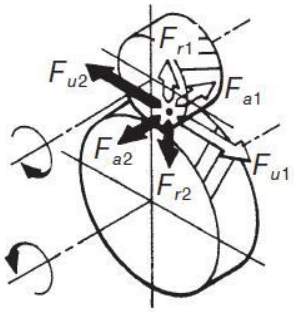

Figure 5. Pinion 1 and Driven Gear. [19]

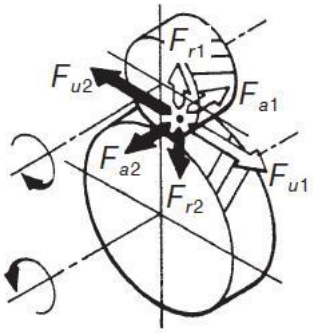

Figure 6. The second pinion and the gear that is being driven by it. [19]

Now both the torque and rotational speed values of the shaft that is being driven by the gear can be computed.
The gear ratio is defined as:

$$Gear\ Ratio = Z_2/Z_1 \quad [20] \tag{6}$$

Therefore, the gear ratio is 5
So, at P_{max}, the speed at which the shaft that is being driven will be;
n_2 = 595 *RPM.*
Also;

$$Gear\ Ratio = \text{Torque out}/\text{Torque in} \quad [20] \tag{7}$$

Torque out / Torque in = 5;
Then; Torque out = 4.46 x 5 = 22.3 *Nm* = 22300 *mNm*.

2.4. The Bracket Design

In the first stage, it is necessary to mark the places of the motor holder part is to be optimized and the places that will not be optimized. It will be possible to save material in the areas marked as areas to be optimized. The places that will not be optimized are usually close to the bearings and there will be no opportunity to save material in these places. [21].

The spaces that are going to be optimized are depicted in brown color and the spaces that are not going to be optimized are shown in grey color. The fixed support is also shown in the figure below (Figure 7.).

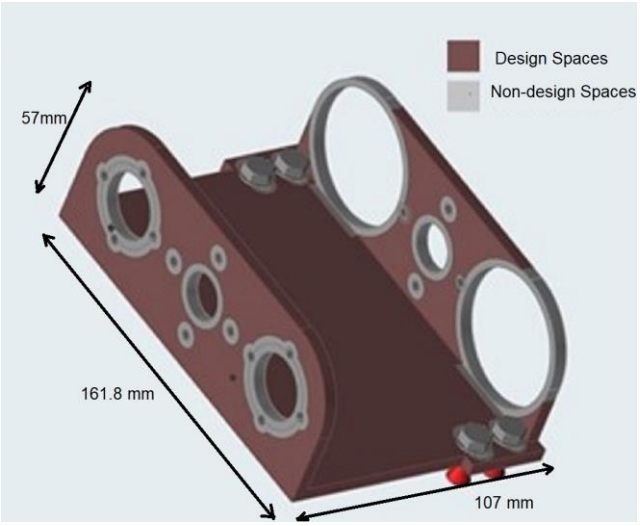

Figure 7. Design and Non-Design Spaces of the Bracket, fixed supports

Material selection is also an important parameter. The basic material of the Electric Motor holder is 7075 Al alloy. However, 7075 Al alloy is an underused material for AM technology. Considering this fact, AlSi10Mg, the closest material to this one and is widely used in AM technology, has been chosen.

Mechanical and thermal expansion information for AlSi10Mg material [5], [22] tabulated in Table 2. These

values are considered in the Altair Inspire™ commercial code. The structural analysis is performed via these tabulated values.

Table 2. Material data for *AlSi10Mg*

Material	**E** (*GPa*)	**Poisson's Ratio**	**Density** (*g/cm³*)	**Yield Stress** (*MPa*)	**Tensile Strength** (*MPa*)	**CTE** (*μm/m °K*)
AlSi10Mg	70	0.33	2.67	215	335	20

2.4.1. Shape Control Application

There are two different ways to control geometry in Inspire™. These are called symmetry and drawing directions. The simultaneous utilization of them is not appropriate and only one is allowed. [23]

Apart from the drawing direction tools in Inspire™, only the protrusion tool is suitable with AM method. The protrusion tool aims to create self-supporting parts. In processes such as casting and extrusion, draw direction tools other than the protrusion tool can be used. [23]

In this study, both the protrusion tool and the symmetry tool were used. Figures 8. a and 8. b show the multiple complex loading states, constraints, protrusion tool, and symmetry tool applied to the part under study.

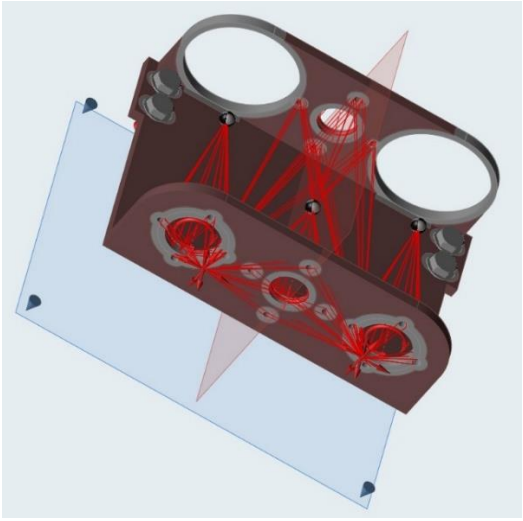

Figure 8.a Various loads, and limitations applied to the original electric motor bracket model.

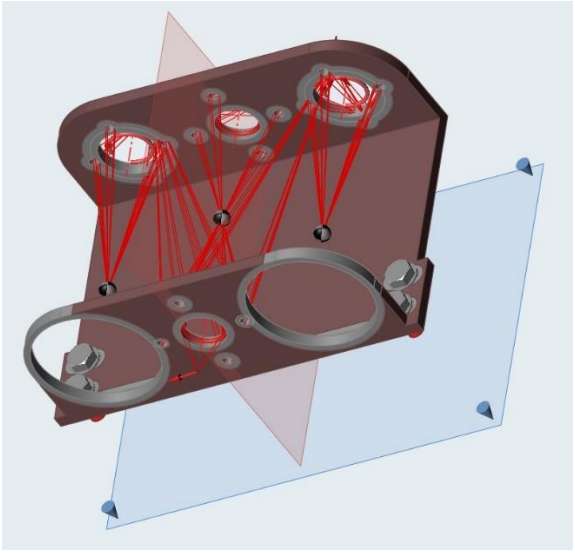

Figure 8.b An alternative perspective of various loads and limitations applied to the original electric motor bracket model.

2.5. Topology Optimization Run

In the next step, the TO process will be run using the previously defined material properties, constraints, and geometry properties.

In TO processes, material saving is only applied in the brown areas shown in Figure 7. The aim is to remove as much material as possible from the part without reducing the strength of the material. In TO operation, the Altair Inspire™ allows the installer to maximize strength or minimize mass.

Once these goals are set, the design constraints on the part need to be applied. If the designer chooses the goal of the study to be strength maximization, a mass target for TO has to be set and entered into the Inspire program. [7].

If the designer sets a wall thickness limit, the TO cycle time can be extended. The Inspire software has the ability to determine the minimum wall thickness by taking into account the average size of the elements in the part [4].

2.6. Redesign of the Part with Inspire PolyNURBS

The PolyNURBS application is part of the Inspire programme. With this application, the irregularly shaped part obtained as a result of the TO application is given a smooth geometry. The part obtained with this method is shown in Figure 9.

Figure 9. Redesigned Model with the Use of PolyNURBS

3. Results and Discussion

3.1. Calculations

For the topology optimization to be performed, we will be based on the Pmax condition of the D.C. motor in order to be more on the conservative side for the final design.

Per this, taking equation 1 and electric motor technical data given in Figure 4 into consideration, P_{max} as well as torque and rotational speed at P_{max} were calculated as below.

Table 3. Pmax, torque and rotational speed at Pmax

P_{max}	1.39 kW
T (at P_{max})	4.46 Nm
Rotational Speed	2975 RPM

Based on the calculations provided in Table-3 and given the

Ψ=20^o (helical angle)

Φ_n= 20^o (normal pressure angle)

m_n= 1 mm (normal module)

Z_1 = 15 (number of teeth on the pinion)

Z_2 = 75 (number of teeth on the helical gear)

results provided in Table-2 were calculated.

Table 4. calculations relating to Gearbox for Pmax condition

ϕ (transverse pressure angle for helical gear)	21.17°
m (module for a helical gear)	1.0642 mm
d1 (pitch diameter of the pinion)	15.963 mm
V (pitch line velocity for helical gear)	2.487 m/sec
n2 (rotational speed of the driven shaft)	595 RPM
Torque Out (at Pmax)	22.3 Nm

Acting forces are calculated as shown below:

F_t = 1000 W / V = 1000 x 1.39 / 2.487 = 558.906 N

$F_r = F_t \tan \Phi$ = 558.906 x tan 21.17^o = 216.449 N

$F_a = F_t \tan \Psi$ = 558.906 x tan 20^o = 203.425 N

$F_n = F_t / \cos \Phi_n \cos \Psi$ = 558.906 / (cos 20^o x cos 20^o) = 635.963 N

3.2. Mass of the Redesigned Model

When comparing the mass of the initial design and the newly created design of the original bracket. under examination, the mass of the designed model as determined by the Altair Inspire™ analysis is 0.24 kg per bracket. While the manufacturing mass of the initial component is 0.35 kg; Based on topology optimization of the aforementioned bracket with additive manufacturing designed using Altair Inspire™, it was determined that the redesign reduced the mass of the part by 31% (0.11 kg).

3.3 The process of reducing waste through the use of the modified model.

Waste minimization emerges as another important advantage of the designed model and its fabrication using additive manufacturing according to the original design and original production technique. It has been calculated that 2.8 kg of AA7075 billet will be required in the production of the original design with known manufacturing techniques. Considering that the final production mass is 0.3 kg, unfortunately, 89% (2.8 kg) of the material is spent as scrap in the production of brackets made in this context.

In addition, as a result of the realization of the designed new model with the suggested additive manufacturing method, the benefit of discarding 2.8 kg of material in the classical method is also obtained. Considering that the amount of scrap in the part designed using the AM technique is 0.11 kg, when 2.5 kg of waste obtained in the classical method of the motor bracket is added, 2.6 kg of material will be saved between both methods and in favor of production with AM technology. According to Christiansen et al., only 20% of the material was utilized for manufacture [8]. Comparatively speaking, our case's 89 percent scrap reduction is a good outcome. The only purpose of this study is to use the additive manufacturing method as the boundary condition for the optimization study.

3.4 Finite Element Analysis of PolyNURBS Results

The Altair Inspire™ program was used for a Finite Element Analysis, which is the performance parameters of the model bracket designed with the help of AM technology, such as yield safety factor, von Misses stresses, and rupture

safety factor.

The yield stress comprehensive safety factor analysis results obtained from the aforementioned program are given in Figure 10 and Figure 11. The ultimate safety factor results obtained from the same program are given in Figure 12 and Figure 13. Besides, Figure 14 and Figure 15 show the von Misses Stress Analysis results.

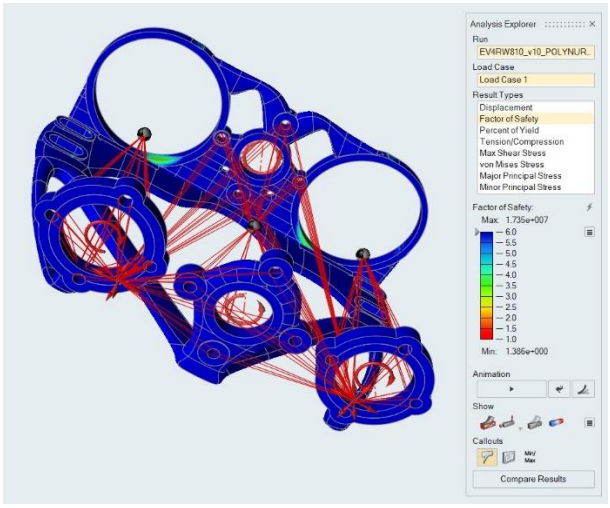

Figure 10. Analysis Results for Factor of Safety for Yielding

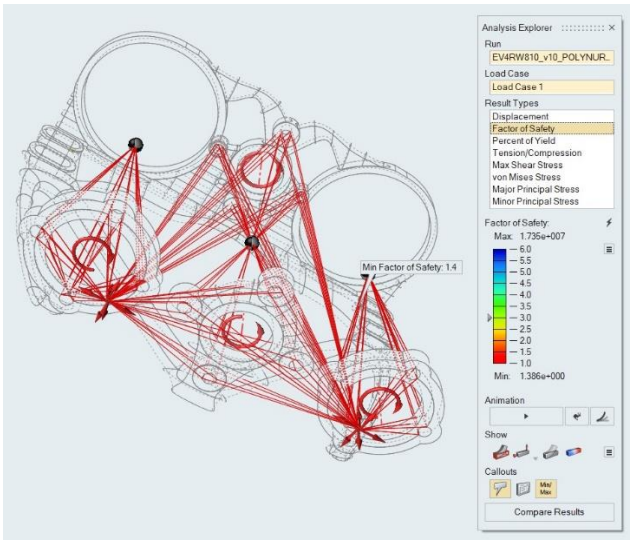

Figure 11. Analysis Results for Factor of Safety for Yielding Showing Minimum FOS Location

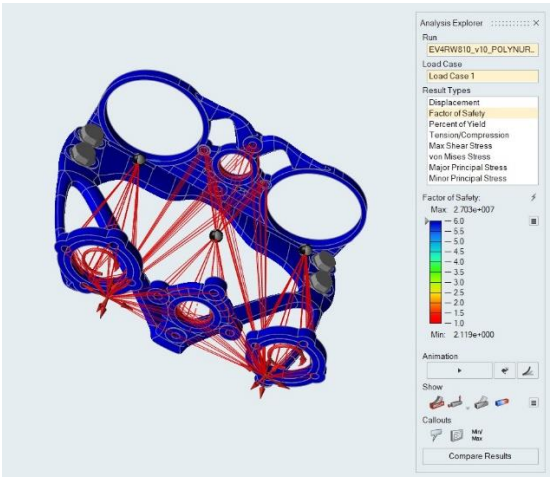

Figure 12. Analysis Results for Ultimate Factor of Safety

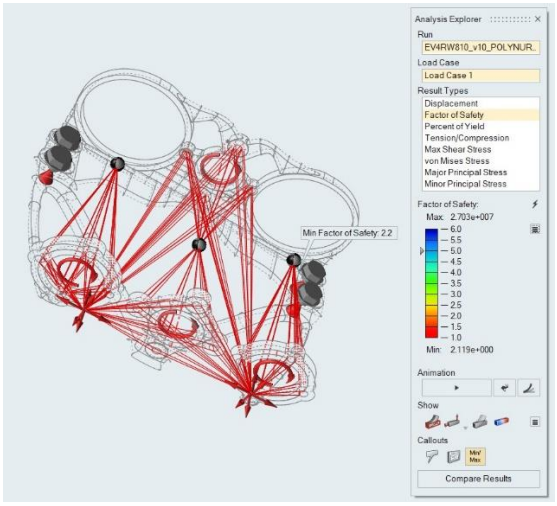

Figure 13. Analysis Results for Ultimate Factor of Safety showing the location where the factor of safety for the ultimate minimum value is achieved.

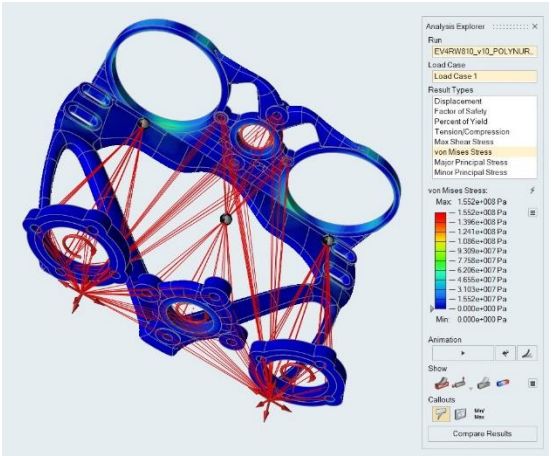

Figure 14. The findings of the examination of v. Mises stress.

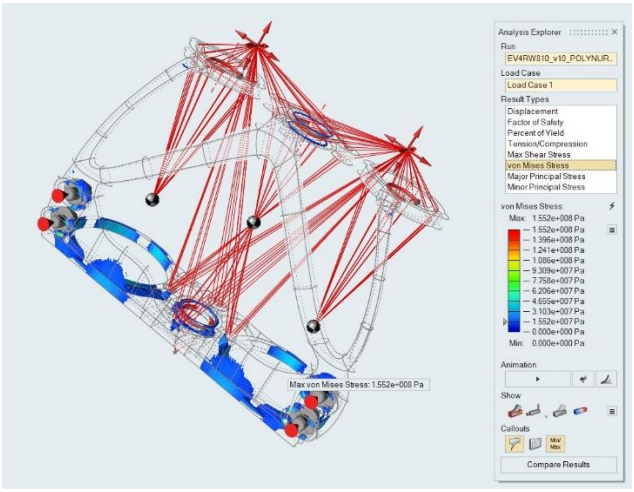

Figure 15. The results of the analysis of von Mises stress indicating the location where the highest stress is present.

3.5 Interpretation of FEA Results and Discussion

When looking at Figures 10 and 11, the minimum safety factor for yielding is determined to be 1.4 and is in the safe zone when the design criterion of 1.25 is taken into account. This result proves that the maximum load on the support remains within the elastic range of the stress-strain curve as intended under the operating conditions of the system in question.

Examination of the analysis results for the maximum factor of safety yielded the results shown in Figures 12 and 14 and showed that the factor in question is ~2.1. This value is considered safe as the maximum safety factor exceeds the aviation standard of 1.5.

In the final phase of the investigation, a stress analysis was performed according to the von Misses criterion and the stress distributions obtained are shown in Figures 14 and 15. As a result of the analysis, a maximum stress of 155.2 MPa was determined in the analyzed part. The yield stress of the material (AlSi10Mg) from which the part is made is 215 MPa. Therefore, the part in the redesigned geometry will be in the elastic range even at Pmax, where the force transmission elements are not exposed at all.

As a result of all these analyses of the redesigned model using the AM method, it has been shown that the part functions safely even under the worst working conditions without exceeding the elasticity limits.

4. Conclusions

In the summary of this study, the tested bracket to be manufactured from 7075 Al alloy was modeled using Altair Inspire™, without changing its original dimensions, as a basis for production by AM method.

The newly designed part was proposed to be manufactured from AlSi10Mg alloy, the most commonly used Al alloy for AM applications. The FEA of the newly molded part in the area of the maximum load of the DC motors resulted in a minimum safety factor of 1.25, which corresponds to the design requirements of 1.4.

The mass of the part which was re-shaped using topology optimization, was diminished by 37%, obtaining 229 grams, concerning the original mass of 364 grams while 89% scrap reduction was achieved compared to the original design via later machining methods.

When examining the results of this study, it was found that the newly designed model, when realized through additive manufacturing, met the strength criteria and would function without structural degradation. In addition, the structural mass was reduced and a significant gain in waste minimization was achieved.

Declaration of Ethical Standards

The authors of this article declare that the materials and methods used in this study do not require ethical committee permission and/or legal-special permission.

Conflict of Interest

The authors declare that they have no known competing financial interests or personal relationships that could have appeared to influence the work reported in this paper.

Abbreviations and Symbols

AM	Additive Manufacturing
CTE	Coefficient of Thermal Expansion
FDM	Fused Deposition Modeling
FEA	Finite Element Analysis
SIMP	Solid Isotropic Material with Penalization Method
TO	Topology Optimization
d_1	Pitch diameter of the pinion
F_a	Force in the x-direction
F_r	Force in the y-direction
F_t	Force in the z-direction
F_u	Force in the tangential axis
m	Module
m_n	Normal module
n_1	Rotational speed of helical gear 1 (RPM)
n_2	Rotational speed of helical gear 2 (RPM)
P	Power (W)
T	Torque (Nm)
V	Pitch line velocity
Z_1	15 teeth helical gear
Z_2	75 teeth helical gear

Φ Pressure angle
Φ_n Normal pressure angle
ω Rotational speed (rad/s)
Ψ Helix angle

References

[1] ASTM INTERNATIONAL, "ASTM F2792-12a," *Rapid Manufacturing Association*, pp. 1–3, 2013, doi: 10.1520/F2792-12A.2.

[2] Clausen, A., 2015. Topology Optimization for Additive Manufacturing,". doi: 10.1017/CBO9781107415324.004.

[3] Gornet T., 2017 "History of Additive Manufacturing,". doi: 10.4018/978-1-5225-2289-8.ch001.

[4] Plocher J. and Panesar A., 2019, Review on design and structural optimization in additive manufacturing: Towards next-generation lightweight structures, Mater Des, **183**, p. 108164, doi: 10.1016/j.matdes.2019.108164.

[5] Liu J. *et al.*, 2018, Current and future trends in topology optimization for additive manufacturing, Structural and Multidisciplinary Optimization, **57**, no. 6, pp. 2457–2483, 2018, doi: 10.1007/s00158-018-1994-3.

[6] Langelaar M., 2017, An additive manufacturing filter for topology optimization of print-ready designs, Structural and Multidisciplinary Optimization, **55**, no. 3, pp. 871–883, 2017, doi: 10.1007/s00158-016-1522-2.

[7] Atzeni E. and Salmi A., 2012, Economics of additive manufacturing for end-usable metal parts, International Journal of Advanced Manufacturing Technology, **62**, no. 9–12, pp. 1147–1155, 2012, doi: 10.1007/s00170-011-3878-1.

[8] Christiansen A.N., Bærentzen J.A., Nobel-Jørgensen M., Aage N., and Sigmund O., 2015. Combined shape and topology optimization of 3D structures, *Computers* and Graphics (Pergamon), **46**, pp. 25–35, 2015, doi: 10.1016/j.cag.2014.09.021.

[9] J. Park J., A. Sutradhar A., Shah J. J., and Paulino G. H., 2018. Design of complex bone internal structure using topology optimization with perimeter control, Comput Biol Med, **94**, pp. 74–84, Mar. 2018, doi: 10.1016/j.compbiomed.2018.01.001.

[10] Mezzadri F., Bouriakov V., and Qian X., 2018. Topology optimization of self-supporting support structures for additive manufacturing, Addit Manuf, **21**, pp. 666–682, May 2018, doi: 10.1016/j.addma.2018.04.016.

[11] Chu S. , Xiao M., Gao L., Li H., Zhang J., and Zhang X., 2019. Topology optimization of multi-material structures with graded interfaces, Computer Methods Appl Mech Eng, **346**, pp. 1096–1117, Apr. 2019, doi 10.1016/j.cma.2018.09.040.

[12] Zheng Y, Da D., Li H., Xiao M., and Gao L., 2020. Robust topology optimization for multi-material structures under interval uncertainty, Appl Math Model, **78**, pp. 627–647, Feb. 2020, doi: 10.1016/j.apm.2019.10.019.

[13] Xu B., Han Y., and Zhao L., 2019. Bi-directional evolutionary topology optimization of geometrically nonlinear continuum structures with stress constraints," Appl Math Model, **80**, pp. 771–791, Apr. 2020, doi: 10.1016/j.apm.2019.12.009.

[14] Liu B., Jiang C., Li G., and Huang X., 2020. Topology optimization of structures considering local material uncertainties in additive manufacturing, Computer Methods Appl Mech Eng, **360**, Mar. 2020, doi: 10.1016/j.cma.2019.112786.

[15] Li J., Guan Y., Wang G., Wang G., Zhang H., and Lin J., 2020. A meshless method for topology optimization of structures under multiple load cases, Structures, **25**, pp. 173–179, Jun. 2020, doi: 10.1016/j.istruc.2020.03.005.

[16] Bi M., Tran P., and Xie Y.M., 2020. Topology optimization of 3D continuum structures under geometric self-supporting constraint, Addit Manuf, **36**, Dec. 2020, doi 10.1016/j.addma.2020.101422.

[17] Aydın L. *et al.*, 2021. Development of Personal Protective Respirator Based on Additive Manufacturing Technologies in Fighting Against Pandemic, Kocaeli Journal of Science and Engineering, **4**, no. 1, pp. 24–38, May 2021, doi: 10.34088/kojose.833205.

[18] Çelebi A. and Tosun A., 2021. Application and Comparison Of Topology Optimization For Additive Manufacturing And Machining Methods, Int. J. of 3D Printing Tech. Dig. Ind, **5**, no. 3, pp. 676–691, 2021, doi: 10.46519/ij3dptdi.

[19] Sakarya University Advanced Technologies Application Center (SAITEM), www.saitem.org.

[20] Budynas R.G., Nisbett J.K., 2011. Shigley's Mechanical Engineering Design, 9th edition, Macgraw Hill, New York.

[21] Diegel O., Nordin A., and Motte D., 2019. A Practical Guide to Design for Additive Manufacturing. 2019. doi: 10.1007/978-981-13-8281-9.

[22] Verbart A., 2015. Topology Optimization with Stress Constraints. 2015. doi: 10.4233/uuid: ee24b186-5db6-4c57-aa50-3b736110ff2a.

[23] Altair Inspire: Generate Structurally Efficient Concepts Quickly and Easily. https://altair.com/inspire

Koc. J. Sci. Eng., 7(1): (2024) 52-61 https://doi.org/10.34088/kojose.1267986

Kocaeli University

Kocaeli Journal of Science and Engineering

http://dergipark.org.tr/kojose

Development of a New Method to Optimize Operations of an Existing Crude Unit

Ziya GÜRÜN [1, *] , Osman BOZDAĞ [2]

[1] *Department of Chemical Engineering, Kocaeli University, Kocaeli,041001, Turkey,* ***ORCID:*** *0000-0003-2971-3816*
[2] *Department of Chemical Engineering, Kocaeli University, Kocaeli,041001, Turkey,* ***ORCID:*** *0000-0002-9734-6555*

Article Info

Research paper

Received : *March 20, 2023*
Accepted : *October 23, 2023*

Keywords

Optimization,
Crude distillation units,
Simplex Algorithm,
Aspen Hysys
Refinery
Test-run
Gasoline
Diesel

Abstract

A nonlinear optimization method working with the Simplex Method was developed to find optimum operating conditions of a crude oil distillation unit subject to defined process constraints, product specifications and prevailing market conditions. Then the method was applied to a commercial crude unit. This crude unit was modeled using Aspen Hysys V12.1 process simulation software. Two sets of market scenarios designated as the maximum gasoline scenario and minimum gasoline scenario were applied to the simulation model. It was found that the model minimized naphtha production and maximized kerosene production for minimum gasoline scenarios where the price of kerosene and diesel products were higher than naphtha products. Similarly, the model maximized the naphtha product yield for the maximum gasoline scenario where the naphtha price exceeds the mid-distillate product price. The iterative procedure developed for the study monotonically converged to optimum operating conditions for both market scenarios. It was observed that the optimization scheme developed in this study could generate a significant profit increase in the conventional crude unit investigated in this study without and capital investment.

1. Introduction

The crude oil distillation unit is one of the most important refinery process units that influence the profitability of refineries. A significant amount of energy consumption occurs in crude distillation units. Consequently, it is essential that crude oil distillation units must be designed correctly and operated efficiently to produce oil products meeting the final product specifications, to operate downstream conversion units efficiently and to maximize the conversion of any given crude oil to valuable products.

The objective of this study is to develop a nonlinear method that systematically optimizes the operating conditions of a crude distillation unit and to apply the method to an existing conventional crude unit. The new method finds the optimum operating conditions of any crude distillation unit corresponding to any set of market conditions, product specifications and process constraints. It is found that optimization can generate a significant amount of savings in crude distillation unit operations, which, in turn, enhances the profitability of refinery operations under stringent economic conditions prevailing throughout the world.

In this study, a conventional crude oil distillation unit is modeled using the Aspen Hysys V12.1 process simulation program. Then the unit is optimized using a nonlinear optimization method working together with the Simplex Algorithm to determine the operating conditions.

The technical details related to design guidelines, operating conditions, and operation principles for crude oil distillation units have been given by Parkash [1], Meyers [2], Gary et al [3], Fahim et al [4], Steven et al [5], and Nelson [6] in great details. The details of the Simplex Algorithm have been explained in detail by Perry et al [7] and Peters et al [8]. Gürün et al. [9, 10] have applied the optimization method presented in this article to power stations composed of steam boilers,

[1] Corresponding Author: ziyagurun@gmail.com

steam turbines, and gas turbines and supplying electrical power and steam at various pressures to refinery units. Similarly, Gürün et al. [11] have applied this optimization model to crude unit feed heaters. These references illustrate the application of the method to power stations and refinery process heaters. Kamışlı et al [14] have modeled a crude distillation unit in Hysys and investigated the effect of kerosene draw temperature, tower overhead vapor temperature, stripping steam flow rate and tower overhead pressure on kerosene yield. Yang et. al [15] have addressed a few references in literature discussing different methods of crude unit optimizations. Some of these references focus on heat exchanger network optimization using pinch technology. Others use surrogate methods to simulate crude units. Many applications concentrate on new unit optimization, revamp work, and heat integration improvement. The current work presented here differs from the previous work in that it optimizes the operating conditions of an existing unit without any capital investment subject to a set of process constraints, an objective function and current market data

2. Materials and Method

In this study, a commercial crude oil distillation unit with 100,000 bbl/day (662.4 m^3/h) crude processing capacity has been modeled by Aspen Hysys V12.1 process simulation software and optimized using the method summarized in Appendix B. A simplified process flow diagram for the unit is given in Figure A.1. Main equipment design data for the unit are given in Table A.1. Process description is given in Appendix A. Delawary [12] has published a test run data for this commercial unit for Kerkuk crude oil feed. The product flow rates and laboratory data were used to construct the crude oil feed to model the unit for test run and optimization calculations. The API of the crude feed used for this study is 34.1.

2.1. Fixed Process Parameters

The main process parameters assumed to be fixed in this study are listed in Table 1. Although some of these variables are controlled and can be included in the list of independent variables for optimisation purposes, these variables were assumed to be fixed here to simplify the example. The fixed variables were taken from the test run data presented by Delawary [12] to compare the optimisation results with the test run conditions.

2.2. Dependent Variable Definitions

Product specifications are given in Table 2. These are also the selected dependent variables used for the optimization. Other process variables in the units, such as temperatures in specific locations, heat duties of some heat transfer equipment, flow rates, and other product specifications can also be selected as dependent variables. However, only the product specifications listed in Table 2 have been selected as dependent variables for simplicity in this study.

2.3. Independent Variable Definitions

The process parameters that are independently controlled by a process control scheme are listed in Table 3. These are defined as independent variables in this study. There can be other process variables that are normally controlled by a process control system such as column pressures, overhead temperatures, flow distributions in in heat exchanger network systems of the units. However, 15 independent variables listed in Table 3 have been defined for each unit to illustrate the optimization method developed in this study for simplicity reasons.

Table 1. Major Process Parameters that are Assumed to be Fixed in Process Simulations

Process Variable	Units	Value
Atmospheric tower overhead temperature	^{0}C	92
Atmospheric tower overhead dram pressure	atm	1.4
Atmospheric tower bottoms pressure	atm	2
Light kero pumparound return temperature	^{0}C	67.8
Heavy kero pumparound return temperature	^{0}C	165.7
Diesel pumparound return temperature	^{0}C	268.2
Feed heater inlet temperature	^{0}C	279
Light kero pumparound rate	m^3/h	429.2
Heavy kero pumparound rate	m^3/h	240.9
Diesel pumparound rate	m^3/h	140.5
Atmospheric tower O/H cold drum temp	^{0}C	30
Atmospheric tower cold overhead drum pres	atm	1.11
Naphtha splitter feed temperature	^{0}C	143
Naphtha splitter overhead pressure	atm	5
Naphtha splitter overhead drum temperature	^{0}C	28
Stabilizer feed temperature	^{0}C	72
Stabilizer overhead pressure	atm	12
Stabilizer overhead drum temperature	^{0}C	39.5

2.4. Objective Function Definition

The objective function defines the parameter that is maximized or minimized in an optimization study. The optimization process tries to find the values of the

independent variables so that the objective function is maximum or minimum while meeting predefined constraints imposed on dependent and independent variables. The objective function can be defined in different ways such as profit maximization, loss minimization, cost minimization, mid-distillate product maximization, and so on. Profit maximization has been selected as the objective function in this study.

A crude distillation unit receives crude oil as feed and produces LPG, naphtha, kerosene, diesel and fuel oil as products. Fuel and steam are consumed as energy sources to sustain the operations. Electrical power is also consumed in the process to run the process pumps. In this study, the total cost of electrical power is assumed to be constant and not to affect the optimization of the objective function. The profit is defined as the difference between the total revenues from the products and the total cost from crude oil, steam and fuel. Then the objective function can be written as given in Eqn 1.

Table 2. Product Specifications Used for the Optimizations

Product Specification	Units	Min	Max
LPG Sp. Gr.			0.56
Full Range Naphtha Sp. Gr.		0.71	0.74
LSRN Sp. Gr.		0.65	0.70
HSRN Sp.Gr			0.77
Light Kerosene Sp.Gr		0.78	0.81
Heavy Kerosene Sp.Gr		0.81	0.83
Diesel Sp. Gr.		0.84	0.87
Naphtha ASTM D 86 EP	^{0}C	150	195
LSRN ASTM D 86 %95 Point	^{0}C		120
HSRN ASTM D 86 %5 Point	^{0}C	95	120
Light Kero ASTM D 86 End Point	^{0}C		235
Heavy Kero ASTM D 86 End Point	^{0}C	255	290
Diesel ASTM D 86 End Point	^{0}C	355	400
Overhead naphtha product rate	m^3/h	80	200
Atmospheric tower bottoms temp.	^{0}C		370
LSRN product rate	m^3/h		50
HSRN product rate	m^3/h		150
LPG Product rate	m^3/h	4	20

$$\theta = \sum C_{prd}Q_{prd} - \sum C_{crd}Q_{crd} - \sum C_{stm}Q_{stm} - \sum C_{fuel}Q_{fuel} \quad (1)$$

2.5. Calculation Procedure

An iterative procedure has been used to find the optimum operating condition of the conventional crude unit. Constraints used in the calculations are given in Table 4. Test run data was used as the initial data to start iterations.

Table 3. Independent Variables

Process Variable	Units	Constraints used in simulation	
		Min	Max
Feed heater outlet temperature	^{0}C	340	380
Atm tower O/H reflux rate	m^3/h	80	150
Light kero stripper steam rate	kg/h	300	500
Light kero stripper steam rate	kg/h	200	400
Diesel stripper steam rate	kg/h	250	450
Main column stripping steam rate	kg/h	4000	6500
Light kero product rate	m^3/h	30	70
Heavy kero product rate	m^3/h	40	90
Diesel product rate	m^3/h	60	150
Light fuel oil product rate	m^3/h	200	400
Naphtha splitter overhead reflux rate	m^3/h	15	30
Naphtha splitter reboiler feed rate	m^3/h	100	250
Naphtha splitter reboiler temperature	^{0}C	200	240
Stabilizer overhead reflux rate	m^3/h	20	40
Stabilizer reboiler temperature	^{0}C	120	170

3. Results and Discussion

The initial and final values of the independent variables for the two market scenarios can be found in Table 4. The corresponding product characteristics and product flow rates are listed in Tables 5 and 6 for these scenarios. The results presented in this section apply only to the commercial crude facility considered in this study, to the market scenarios shown in Table-C.1, to the product specifications shown in Table-2, and to the independent process variables tabulated in Table-4 for illustrative purposes. The optimisation method is a general method that could be applied to any other crude distillation unit for any other set of valid market, design and product specification data. Consequently, the results of the optimisation may vary under different conditions.

The optimization calculations resulted in higher objective function values for both the minimum and maximum gasoline scenarios in relation to the test run conditions as shown in Table-6. The minimum gasoline and maximum gasoline scenarios provided a profit increase of $19.2 million/year and $11.7 million/year profit increase respectively. In general, the products of the crude distillation units are not final refinery products that meet the product specifications. As a result, crude unit product prices for crude oil products are normally lower than prices for the final products and crude oil products alone usually do not usually generate positive profit [13]. The value of objective function based on net profit turns out to be a negative number. Maximizing the objective function in this study actually means minimizing the negative value of the objective function.

Although the value of the objective function turns out to be negative, the difference between the optimal operating conditions and the test run conditions is positive for both market scenarios. The absolute values of the objective function for both scenarios do not mean that one scenario offers a higher profit than the other as the price basis for both scenarios is different.

Table 4. Initial and Final Values of Independent Variables Calculated for each Optimization Scenario

Process Variable	Units	Minimum Gasoline		Maximum Gasoline	
		Test Run	Optimum	Test Run	Optimum
Feed heater outlet temperature	^{0}C	374.0	367.2	374.0	368.6
Atm tower overhead reflux rate	m^3/h	122.9	112.4	122.9	125.6
Light kero stripper steam rate	kg/h	453.8	464.6	453.8	339.8
Heavy kero stripper steam rate	kg/h	359.5	279.6	359.5	259.9
Diesel stripper steam rate	kg/h	413.2	331.4	413.2	308.6
Main column st. stm rate	kg/h	5,977.0	5,697.5	5,977.0	4,761.0
Light kero product rate	m^3/h	45.7	54.3	45.7	47.1
Heavy kero product rate	m^3/h	62.6	66.9	62.6	58.0
Diesel product rate	m^3/h	122.2	122.5	122.2	124.8
Light fuel oil product rate	m^3/h	251.4	250.5	251.4	249.9
NS overhead reflux rate	m^3/h	24.4	27.0	24.4	23.9
NS reboiler feed rate	m^3/h	204.0	173.9	204.0	186.4
NS splitter reboiler temperature	^{0}C	224.0	223.0	224.0	226.6
Stabilizer overhead reflux rate	m^3/h	32.1	28.8	32.1	31.3
Stabilizer reboiler temperature	^{0}C	153.7	143.2	153.7	139.3
Objective Function (1000 $/h)		-35.7	-33.5	-12.3	-10.9
Annual Savings (Mil $/Year)		19.2		11.7	

The model adjusted the plant operating conditions for minimum gasoline operation such that the total flow rate of light kerosene and heavy kerosene increased from 108.3 m3/h for the test run conditions to 121.2 m3/h for the optimum conditions, while the sum of the flow rates of light naphtha and heavy naphtha decreased from 169.5 m3/h to 160.8 m3/h, as shown in Table-6. The switch from naphtha products to kerosene products resulted in a decrease in the specific gravity of naphtha products, the specific gravity of kerosene products and the specific gravity of naphtha across the range, as shown in Table 5. Similarly, the ASTM D-86 naphtha product endpoint decreased from 170.8 0C under the test run conditions to 164.9 0C under the optimum conditions, as shown in Table 5. The model also optimised the plant energy consumption compared to the test run conditions by reducing the feed heater outlet temperature, stripping steam rates, naphtha splitter reboiler output and stabiliser reboiler output as indicated in Table 3, provided the product specifications defined in Table 2 are still met. The model adjusted the process conditions of the plant in minimum gasoline mode to maximise the flow rates for light and heavy kerosene and minimise the flow rates for naphtha, as the naphtha price was set to a lower value than the diesel and kerosene price. This result in turn maximises the value of the objective function for the minimum gasoline scenario.

Table 5. Initial and Final Values of Product Properties for each Optimization Scenario

Process Variable	Units	Minimum Gasoline		Maximum Gasoline	
		Test Run	Optimum	Test Run	Optimum
LPG Sp. Gr.		0.5480	0.5400	0.5480	0.5360
Full Range Naphtha Sp. Gr.		0.7196	0.7164	0.7196	0.7202
LSRN Sp. Gr.		0.6691	0.6598	0.6691	0.6564
HSRN Sp.Gr		0.7385	0.7369	0.7385	0.7394
Light Kerosene Sp.Gr		0.7886	0.7827	0.7886	0.7905
Heavy Kerosene Sp.Gr		0.8162	0.8154	0.8162	0.8167
Diesel Sp. Gr.		0.8582	0.8586	0.8582	0.8589
Full Range Naphtha ASTM D 86 EP	^{0}C	170.8	164.9	170.8	171.6
LSRN ASTM D 86 %95 Point	^{0}C	97.7	96.9	97.7	98.7
HSRN ASTM D 86 %5 Point	^{0}C	111.7	111.4	111.7	112.9
Light Kero ASTM D 86 End Point	^{0}C	221.5	219.5	221.5	225.5
Heavy Kero ASTM D 86 End Point	^{0}C	281.5	283.1	281.5	281.2
Diesel ASTM D 86 End Point	^{0}C	394.0	400.0	394.0	400.0
Overhead naphtha product rate	m^3/h	180.7	168.3	180.7	182.7
Atmospheric tower bottoms tem.	^{0}C	354.4	350.2	354.4	353.7
LSRN product rate	m^3/h	20.2	26.1	20.2	27.5
HSRN product rate	m^3/h	149.2	134.6	149.2	149.0
LPG Product rate	m^3/h	11.1	6.5	11.1	4.4

Table 6. Initial and Final Product Flows for each Optimization Scenario

Product Flow Rate	Units	Minimum Gasoline		Maximum Gasoline	
		Test Run	Optimum	Test Run	Optimum
LPG	m^3/h	11.1	6.5	11.1	4.4
Light Naphtha	m^3/h	20.2	26.1	20.2	27.5
Heavy Naphtha	m^3/h	149.2	134.6	149.2	149.0
Light Kerosene	m^3/h	45.7	54.3	45.7	47.1
Heavy Kerosene	m^3/h	62.6	66.9	62.6	58.0
Diesel	m^3/h	122.2	122.5	122.2	124.8
Light Fuel Oil	m^3/h	251.4	250.5	251.4	249.9

The model shifted the plant operating conditions for the maximum gasoline mode so that the total flow of light naphtha and heavy naphtha increased from 169.5 m3/h for the test run conditions to 176.5 m3/h for the optimum conditions, while the sum of the flows of light kerosene and heavy kerosene decreased from 108.3 m3/h to 105.1 m3/h, as shown in Table-6. In addition, the total naphtha production increased from 160.8 m3/h in minimum gasoline mode to 176.5 m3/h in maximum gasoline mode, while the total kerosene production decreased from 121.2 m3/h to 105.1 m3/h under optimum conditions. As naphtha production increased from the minimum gasoline mode to the maximum gasoline mode, the specific gravities of light kerosene and heavy kerosene increased. The distillation endpoint according to ASTM D-86 for light kerosene also increased significantly.

Since the price of the kerosene products in Table 5 is slightly higher than that of the diesel products, the model produced more kerosene than diesel for both the minimum and maximum petrol modes. The model also adjusted the flow rates of diesel and light fuel oil for both market scenarios such that the end-point of the ASTM D-86 diesel product is shifted to the maximum limit of 400 0C defined in Table 5.

The convergence of the proposed calculation method is shown in Figure 1 and Figure 2 for both scenarios. These figures show that the values of the objective functions increase continuously up to a maximum value. These figures are given here to illustrate that optimising the operating conditions of a conventional crude oil distillation plant can lead to significant profit increases.

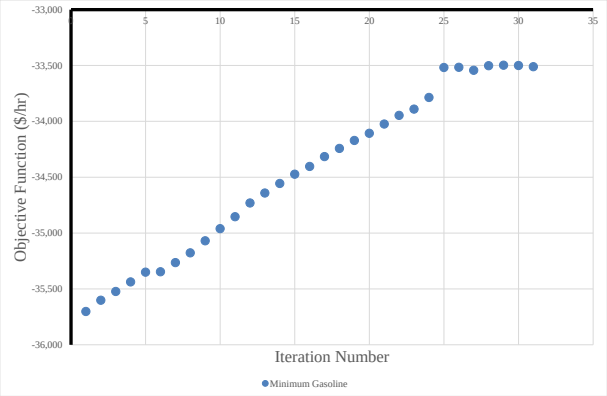

Figure 1. Convergence of the Calculation Procedure – Minimum Gasoline Scenario

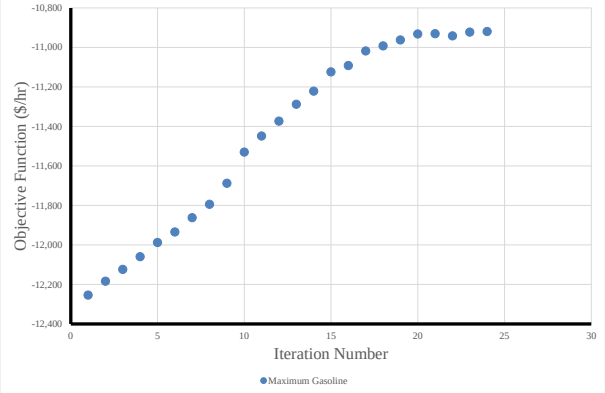

Figure 2. Convergence of the Calculation Procedure – Maximum Gasoline Scenario

4. Conclusions

A non-linear method was developed to optimise the operation of a crude oil plant depending on the prevailing market conditions, taking into account process constraints and product specifications. The method was applied to a conventional crude oil distillation plant for two different market scenarios. It was found that the iterative method converges monotonically to the optimal solution within a reasonable number of iterations.

The optimal operating conditions of the plants indicated that the profitability of the crude oil plant analysed in this study could be significantly increased for both scenarios. The optimisation calculations resulted in higher objective function values for both the minimum and maximum petrol scenarios in relation to the test run conditions. The minimum petrol and maximum petrol scenarios delivered a profit increase of $19.2 million/year and $11.7 million/year respectively.

Once a process unit, such as a crude distillation unit, has been designed and built, its mechanical configuration cannot be changed. However, due to changing market conditions, new product specifications and alternative strategic objectives, the unit may need to be operated within the permitted process limits under completely different operating conditions than the design conditions. This study proposes an optimisation method that can be applied to any existing process unit to determine alternative process conditions so that the unit can continue to operate under the strict economic conditions of a competitive market.

The commercial crude oil unit used in this study is just one example of a typical design. Many different configurations are possible. However, the optimisation method described in this study can be applied to any alternative configuration of the crude unit for any other optimisation criterion, such as minimum gasoline, maximum aviation gasoline and minimum middle distillate production.

Declaration of Ethical Standards

The author(s) of this article declare that the materials and methods used in this study do not require ethical committee permission and/or legal-special permission.

Conflict of Interest

The authors declare that they have no known competing financial interests or personal relationships that could have appeared to influence the work reported in this paper.

Acknowledgements

Authors would like to express sincere appreciations to Kocaeli University Scientific Research Projects

Department for their financial support (Project ID: 2243).

References

[1] Parkash, S., 2003, Refining Processes Handbook, Gulf Professional Publishing.

[2] Meyers, R. A., 1997 Handbook of Petroleum Refining Processes, 2nd ed., Mc-Graw Hill.

[3] Gary, J. H., Handwerk, G. E., Kaiser M. J., 2007, Petroleum Refining Technology and Economics, 5th ed., CRC Press.

[4] Fahim, M. A., Al-Sahhaf, T. A., Elkilani A. S., 2010, Fundamentals of Petroleum Refining, Elsevier, 1st ed.

[5] Steven, A. T., Pujado P. R., Jones D. S. J., 2015, Handbook of Petroleum Processing, Springer Reference, 2nd ed.

[6] Nelson, W. L., 1958, Petroleum Refinery Engineering, 4th ed., Mc.Graw Hill.

[7] Perry, R. H., Chilton C. H., Chemical Engineers' Handbook, 5th ed., Mc-Graw Hill.

[8] Peters, M. S., Timmerhaus K. D., 1980, Plant Design and Economics for Chemical Engineers, 3rd ed., Mc-Graw Hill.

[9] Gürün Z., Bozdağ O., 2017, Enerji Santrallerinin Modellenmesi ve Optimizasyonu, Paper presented at 4. Enerji Verimliliği Konferansı, 13-14 October, Kocaeli, Turkey.

[10] Gürün Z., Bozdağ O., 2018, A Case Study on Modeling and Optimization of Power Plants, Paper presented at Petrochemical and Refining Conference Europe, April 9-10, Moskov, Russia.

[11] Gürün Z., Bozdağ O., 2019, Ham petrol Şarj Fırınlarında Optimizasyon, Paper presented at 22. Isı Bilimi ve Tekniği Kongresi, 11-14 September, Kocaeli, Turkey.

[12] Delewary A. R., 2018, Aspen Hysys ile Ham Petrol Damıtma Ünitesinin Simülasyonu, Masters Thesis, Kocaeli University.

[13]https://tprstaticfilessa.blob.core.windows.net/assets/uploads/yatirimcisunumlari/tr/yatirimci_sunumu_tem_%2023.pdf

[14] Kamışlı F., Ahmed A. A., 2019, Simulation and Optimization of A Crude Oil Distillation Unit, Turkish Journal of Science and Technology, 14(2), 59-68.

[15] Yang K., Liu S., He C., Zhang B., Chen Q., Pan M., 2020, Improving energy saving of crude oil distillation units with optimal operations, Journal of Cleaner Production, Vol 263, 121340

Appendix A: Process Description

Figure A.1 shows a simplified process flow diagram of the conventional crude oil distillation plant.

The crude oil feed first enters the atmospheric column after passing through a series of heat exchangers. While the products in the atmospheric column cool down, the crude oil heats up in these heat exchangers. The crude oil then passes through the feed heater before entering the atmospheric column at a controlled temperature. The atmospheric column considered for this study is equipped with three side strippers and three circulation streams. Light kerosene, heavy kerosene and diesel products are extracted from these side strippers. Stripping vapour is fed to these strippers to recover all the light hydrocarbons in these products. Stripping vapour is also fed to the bottom of the atmospheric column to recover any light hydrocarbons remaining in the light fuel oil product. The vapour leaving the top of the column is condensed by an overhead condenser and collected in a vessel. All non-condensed gaseous hydrocarbons leave the system as fuel gas from the overhead tank. Some of the condensing liquid in the overhead vessel is returned to the column as overhead reflux and the remaining liquid is withdrawn from the column as overhead product. The bottom product is withdrawn from the column as light fuel oil product.

The liquid overhead product withdrawn from the atmospheric column is basically a mixture of heavy naphtha, light naphtha and LPG products separated in naphtha splitter and debutaniser columns. The liquid overhead product from the atmospheric column is first fed into the naphtha splitter column where heavy naphtha is separated from the feed stream according to the product specification. The naphtha splitter is a distillation column where the overhead product is a mixture of LPG and light naphtha and the bottom product is heavy naphtha. The debutaniser is also a distillation column in which LPG and light naphtha products are separated. The debutaniser column is fed with the liquid overhead from the naphtha splitter column.

The most important design data for the equipment used in the plant can be found in Table A.1.

Table A.1. Main Equipment Design Data

Atmospheric Column	Number of Stages	35
	Feed Tray	30
	Lt Kero PA Return Stg	6
	Lt Kero PA Draw Stg.	8
	Hv Kero PA Return Stg	18
	Hv Kero PA Darw Stg	19
	Diesel PA Return Stg	26
	Diesel PA Darw Stg	29
	Condenser	Air, Partial
Light Kero Stripper	Number of Stages	4
	Vapor Return Stg	10
	Light Kero Draw Stg	12
Heavy Kero Stripper	Number of Stages	4
	Vapor Return Stg.	18
	Heavy Kero Draw Stg	19
Diesel Stripper	Number of Stages	4
	Vapor Return Stg.	24
	Heavy Kero Draw Stg	25
Naphtha Splitter	Number of Stages	20
	Feed Tray	10
	Condenser	Partial
	Reboiler	Heater, Partial
Debutanizer Column	Number of Stages	20
	Feed Tray	10
	Condenser	Partial
	Reboiler	S/T, Partial

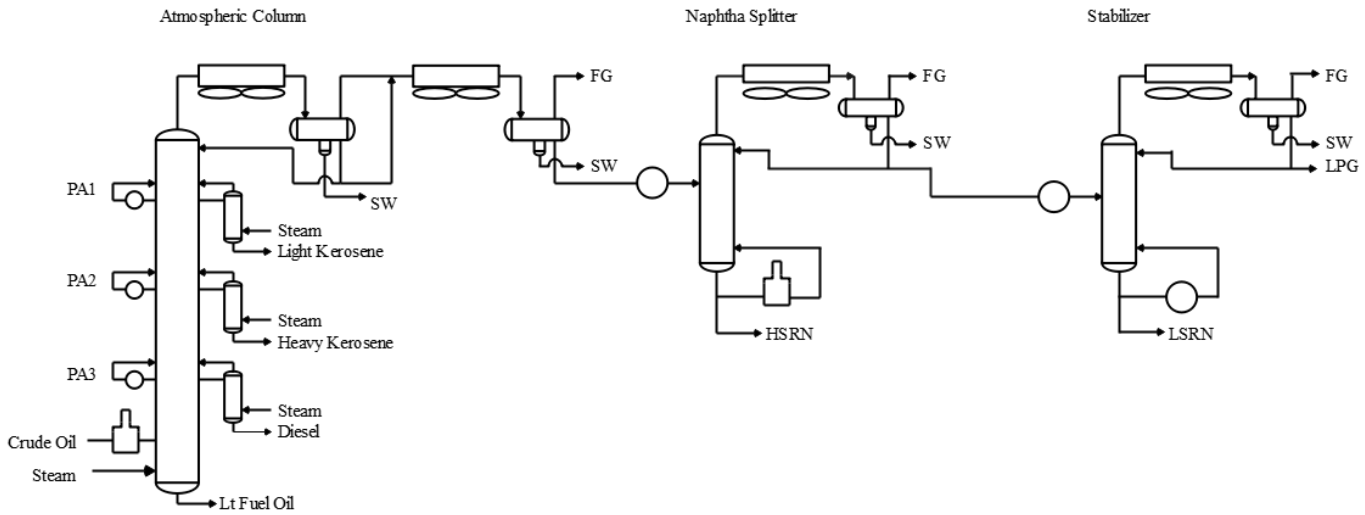

Fig A.1. Simplified Process Flow Diagram of a Conventional Crude Unit

Appendix B: Theoretical Background

When a crude oil plant operates in automatic mode with multiple process control loops under steady-state conditions, each of these process control variables can be changed independently. Each time a process control variable is changed, the process conditions in the entire plant change according to the change in the process control variable. These process control variables were defined as independent variables in this study. The outlet temperature of a heater, the pressure in a tower, the reflux rate in a column, the pumping rates in the column, the product withdrawal rates, the stripping vapour rates are just a few examples of these independent variables. When one of these variables is changed, there is a corresponding change in all process conditions and product characteristics in the plant. The variables that depend on the independent variables are defined as dependent variables in this study. The temperature at any point in a column, the specific gravity of a product, the distillation properties of a product can be given as examples of dependent variables, since any change in an independent variable causes a corresponding change in all dependent variables. The relationship between the independent and dependent variables is shown in Figure B.1.

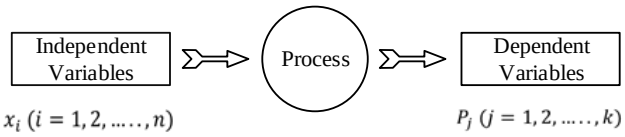

Figure B.1. Relations among Independent Variables, Process and Dependent Variables.

Let x_i be the value of any process variable that can be changed independently by the process control system operating the plant. There is n of these independent variables that are used for the operation of the plant or are included in the optimisation model of the plant. Therefore, i, the index of the independent variables, changes from 1 to n. Let P_j be any process variable that belongs to the plant. Any number of process variables can be defined for each raw plant or used as a dependent variable for the optimisation of the raw plant. Consequently, j, the index of the dependent variable, changes from 1 to k. All dependent variables change simultaneously when one of the independent variables in the plant changes. Therefore, each dependent variable is a function of all independent variables.

$$P_j = P_j(x_1, x_2, x_3, \ldots\ldots, x_n) \quad j = 1, 2, 3, \ldots\ldots, k \quad \text{(B.1)}$$

Differentiation of this expression yields the following equation.

$$dP_j = \frac{\partial P_j}{\partial x_1} dx_1 + \frac{\partial P_j}{\partial x_2} dx_2 + \frac{\partial P_j}{\partial x_3} dx_3 + \cdots + \frac{\partial P_j}{\partial x_n} dx_n \quad \text{(B.2)}$$

Each dependent variable shall be limited by a maximum and a minimum value. Therefore,

$$P_{j,min} \leq P_j \leq P_{j,max} \quad \text{(B.3)}$$

Furthermore, each independent variable is also limited by a maximum and a minimum value.

$$x_{i,min} \leq x_i \leq x_{i,max} \quad \text{(B.4)}$$

These equations can be expressed in dimensionless parameters defined as follows.

$$P_j^* = \frac{P_j - P_{j,min}}{P_{j,max} - P_{j,min}} \quad \text{(B.5)}$$

$$x_i^* = \frac{x_i - x_{i,min}}{x_{i,max} - x_{i,min}} \quad \text{(B.6)}$$

Then equations (3) and (4) can be written as follows.

$$0 \leq P_j^* \leq 1 \quad \text{(B.7)}$$

$$0 \leq x_i^* \leq 1 \quad \text{(B.8)}$$

The differential form of the dependent variable given in equation (2) can also be expressed in dimensionless form as follows.

$$dP_j^* = \frac{\partial P_j^*}{\partial x_1^*} dx_1^* + \frac{\partial P_j^*}{\partial x_2^*} dx_2^* + \frac{\partial P_j^*}{\partial x_3^*} dx_3^* + \cdots + \frac{\partial P_j^*}{\partial x_n^*} dx_n^* \quad \text{(B.9)}$$

An objective function must be defined. In this study to optimise the operating parameters of a system. In this study, the objective function for optimisation is defined as the net profit. The net profit is defined as the difference between the revenue from the unit's products and the expenditure on crude oil, energy and steam to produce these products. Each time an independent variable is changed, the parameters in the objective function also change. Therefore, the objective function is also a function of all independent variables that can be changed by a process control system.

$$\theta = \theta(x_1, x_2, x_3, \ldots\ldots, x_n) \quad \text{(B.10)}$$

Differentiation of the objective function yields the following expression.

$$d\theta = \frac{\partial \theta}{\partial x_1} dx_1 + \frac{\partial \theta}{\partial x_2} dx_2 + \frac{\partial \theta}{\partial x_3} dx_3 + \cdots + \frac{\partial \theta}{\partial x_n} dx_n \quad \text{(B.11)}$$

Using the dimensionless definition of the independent variables given in equation (6), the differential form of the objective function can be written as follows.

$$d\theta = \frac{\partial \theta}{\partial x_1^*} dx_1^* + \frac{\partial \theta}{\partial x_2^*} dx_2^* + \frac{\partial \theta}{\partial x_3^*} dx_3^* + \cdots + \frac{\partial \theta}{\partial x_n^*} dx_n^* \quad \text{(B.12)}$$

Optimising the operating conditions means finding a set of all independent variables that maximises the value of

the objective function while satisfying the constraints imposed on the independent and dependent variables defined by equations (7) and (8) in dimensionless form. Since the operation of a crude oil distillation unit involves many complex processes, the mathematical model of the unit also requires a solution for highly nonlinear sets of equations. Therefore, an iterative procedure is developed in this study to find the set of independent variables that optimises the objective function. The iterative procedure attempts to find at each step the change in the independent variable (dx^*_i) that leads to an optimal change in the value of the objective function defined in equation (12), while maintaining the constraints on the independent and dependent variables defined in equations (7) and (8), until no change in the value of the objective function is observed.

Based on this approach, values of dependent and independent variables can be written as follows.

$$dx^*_{i,t} = x^*_{i,t+1} - x^*_{i,t} \tag{B.13}$$

$$dP^*_{j,t} = P^*_{j,t+1} - P^*_{j,t} \tag{B.14}$$

The subscript t in the above equations stands for the number of steps in the iteration procedure. Equations (7), (8), (13) and (14) can be combined to obtain the following constraint equations which define the limits for the change of the dependent and independent variables at each step of the iteration.

$$-x^*_{i,t} \le dx^*_{i,t} \le 1 - x^*_{i,t} \tag{B.15}$$

$$-P^*_{j,t} \le dP^*_{j,t} \le 1 - P^*_{j,t} \tag{B.16}$$

The partial derivatives in equation (9) define the contribution of a change in the value of each independent variable to the change in the value of the dependent variable. Equation (16) defines the limit of the total allowable change in the values of the dependent variable at each iteration step. By combining equations (9) and (16), the limits for the change of each independent variable for each iteration step can be defined as follows.

$$-\frac{P^*_{j,t}}{\frac{\partial P^*_{j,t}}{\partial x^*_{i,t}}} \le dx^*_{i,t} \le \frac{1-P^*_{j,t}}{\frac{\partial P^*_{j,t}}{\partial x^*_{i,t}}} \tag{B.17}$$

This expression can be calculated k times for each independent variable at each iteration step. The limits with the minimum absolute values specify the permissible maximum and minimum values for the change in the value of the independent variable. Equations (15) and (17) together define the limits for the change in the value of each independent variable at each iteration step. These equations can be written as follows.

$$\varepsilon_{i,min,t} \le dx^*_{i,t} \le \varepsilon_{i,max,t} \tag{B.18}$$

The aim of the solution is to find a set of dx*i,t that satisfies the constraints defined by equations (18) and (16) and maximises the change in the objective function specified in equation (12). The simplex algorithm can be used to find the desired solution. The following transformation can be implemented to apply the simplex algorithm.

$$du_{i,t} = \frac{dx^*_{i,t} - \varepsilon_{i,min,t}}{\varepsilon_{i,max,t} - \varepsilon_{i,min,t}} \tag{B.19}$$

Then the limits of $du_{i,t}$ are defined as follows.

$$0 \le du_{i,t} \le 1 \tag{B.20}$$

Equations (9), (16) and (19) can be combined to express the dependent variable differentials as follows.

$$\begin{aligned} -P^*_{j,t} - \sum_{i=1}^{n} \frac{\partial P^*_{j,t}}{\partial x^*_{i,t}} \varepsilon_{i,min,t} \\ \le \sum_{i=1}^{n} \frac{\partial P^*_{j,t}}{\partial x^*_{i,t}} (\varepsilon_{i,max,t} - \varepsilon_{i,min,t}) du_{i,t} \\ \le 1 - P^*_{j,t} - \sum_{i=1}^{n} \frac{\partial P^*_{j,t}}{\partial x^*_{i,t}} \varepsilon_{i,min,t} \end{aligned} \tag{B.21}$$

Objective function differential given in equation (12) can be transformed into the following expression using equation (19).

$$d\theta - \sum_{i=1}^{n} \frac{\partial \theta}{\partial x^*_{i,t}} \varepsilon_{i,min,t} = \sum_{i=1}^{n} \frac{\partial \theta}{\partial x^*_{i,t}} \left(\varepsilon_{i,max,t} - \varepsilon_{i,min,t}\right) du_{i,t} \tag{B.22}$$

Simplex Algorithm is used to find a set of $du_{i,t}$ that maximizes the right hand side of equation (22) while meeting the constraints defined in equations (20) and (21) at each iteration step.

Appendix C. Market Data

Market data such as crude oil costs, product prices and energy costs are important factors that affect the profitability of a crude oil plant. These market data are constantly changing over time and lead to shifts in the optimal operating conditions of the plant. The data selected for this study are listed in Table C.1. As the market data changes over time, the optimisation calculations should be repeated to find a new optimal operating point that corresponds to the prevailing market conditions. In this study, the minimum petrol consumption scenario and the

maximum petrol consumption scenario were considered. The market data shown in Table C.1 reflect the average conditions in the first quarter of 2022.

Table C.1. Market Data Used for Optimization Study as of the first quarter of 2022

Market Parameter	Units	Minimum Gasoline	Maximum Gasoline
Steam Cost	$/Ton	38,46	38,46
Natural Gas	$/MM kcal	49,11	49,11
Dated Brent	$/bbl	100	100
Kerkuk Crude Oil Spread	$/bbl	-1	-1
Naphtha Crack	$/bbl	-6	16
Kerosene Crack	$/bbl	14,5	14,5
Diesel Crack	$/bbl	14	14
Fuel Oil Crack	$/bbl	-22	-22
LPG	$/Ton	778	778

The minimum petrol demand scenario reflects the market case in which diesel and kerosene products are in greater demand than petrol. Therefore, the naphtha price is lower than the diesel and kerosene price. The scenario with maximum petrol demand reflects the case in which market demand for petrol is high, which is why the naphtha price is higher than in the case with minimum petrol demand. The only difference between the two scenarios is therefore the high naphtha price in the scenario with maximum petrol demand.

Appendix D. Nomenclature

C_{crd} Purchase price of each crude oil feed stream ($/m^3)
C_{fuel} Fuel cost ($/kcal)
C_{prd} Sale price of each product item ($/m^3), for LPG product $/ton.
C_{stm} Cost of steam stream ($/kg)
$du_{i,t}$ Transformed independent variable differential defined by equation (19)
P_j Dependent variable j
P_j^* Dimensionless form of dependent variable P_j as defined in equation (5)
$P_{j,max}$ Maximum value of dependent variable P_j
$P_{j,min}$ Minimum value of dependent variable P_j
$P^*_{j,t}$ Dimensionless independent variable j at iteration step t
$P^*_{j,t+1}$ Dimensionless independent variable j at iteration step t+1
Q_{crd} Flow rate of each crude oil feed (m^3/h)
Q_{fuel} Fuel consumption (kcal/h)
Q_{prd} Flow rate of each product item (m3/h), for LPG product Ton/h.
Q_{stm} Flow rate of steam (kg/h)
x_i Independent variable i
x_i^* Dimensionless form of independent variable x_i as defined in equation (6)
$x_{i,max}$ Maximum value of independent variable x_i
$x^*_{i,t}$ Dimensionless dependent variable i at iteration step t
$x_{i,min}$ Minimum value of independent variable x_i
$x^*_{i,t+1}$ Dimensionless dependent variable i at iteration step t+1
i Independent variable index (i = 1, 2, 3, ……, n)
j Dependent variable index (j = 1, 2, 3, ……., k)
t Iteration step index
θ Objective function
$\varepsilon_{i,max,t}$ Maximum limit for $dx^*_{i,t}$ at iteration step t
$\varepsilon_{i,min,t}$ Minimum limit for $dx^*_{i,t}$ at iteration step t

Koc. J. Sci. Eng., 7(1): (2024) 62-70 https://doi.org/10.34088/kojose.1279222

Kocaeli University

Kocaeli Journal of Science and Engineering

http://dergipark.org.tr/kojose

Human Head Transcranial Magnetic Stimulation Using Finite Element Method

Enver SALKIM [1, 2, *], Tayfun ABUT [2]

[1] *Department of Electronics and Automation, Mus Alparslan University, Mus, Turkey,* ***ORCID:*** *0000-0002-7342-8126*
[2] *Department of Electronics and Electrical Engineering, University College London (UCL), London, UK,* ***ORCID:*** *0000-0002-7342-8126*
[3] *Department of Mechanical Engineering, Mus Alparslan University, Mus, Turkey,* ***ORCID:*** *0000-0003-4646-3345*

Article Info

Research paper

Received : *April 24, 2023*
Accepted : *December 13, 2023*

Keywords

coil current
coil heating
computational model
finite element simulation
transcranial magnetic stimulation

Abstract

Transcranial magnetic stimulation (TMS) is a wearable neuromodulation technique. It is approved for several therapies for various neurological disorders, including major depressive disorder, traumatic brain injury, Parkinson's disease, and post-traumatic stress disorder. This method became an alternative neuromodulation technique for such brain-related disorders. However, it has shown significant improvement in this alternative approach. Studies based on this technique have shown limited efficacy. They might be associated with current levels, poor coil locality, optimal coil size, and neuromodulator settings. It has been shown in this research that coil heating is related to higher levels of current. Thus, it is required to analyze the impact of the current levels on the induced magnetic distribution to define the optimal current range for the TMS coils. It is not feasible to investigate this research with experimental tests and analytic methods. Alternatively, using an advanced computational model of the coils and accounting for different human head anatomical layers, coil current capacity can be optimized based on finite element magnetic field distribution. This paper aims to investigate the impact of the coil current levels on the induced magnetic field distribution. The current capacity of the coils can be optimized based on the required magnetic field. In this way, the overheating may be reduced and may result in increased efficacy. As a proof-of-concept, a prototype coil and multi-layered geometrical human head models were generated using geometric shapes. The fundamental human head tissue layers were generated based on their average thickness. The model was simulated based on a finite element magnetic simulation using appropriate boundary conditions and neuromodulator settings. The various coil current levels were applied to analyze the outcome. The models were simulated, and the results were recorded based on these current levels. Results showed that there is a direct relation between applied current levels and induced magnetic flux density in the region of interest.

1. Introduction

There is a significant increase in alternative noninvasive brain stimulation methods and a growing domain of research and development for clinical neurophysiology. Thus, many applications have been generated for disease diagnosis and pathophysiologic investigation of cortical excitability changes, and mapping of cortical function (e.g., before brain surgery) [1]– [4]. Transcranial magnetic stimulation (TMS) is a noninvasive technique for neuromodulation that has a therapeutic effect on neurological disorders including major depressive disorder, traumatic brain injury, Parkinson's disease, and post-traumatic stress disorder [5]. TMS has become a promising, safe, and noninvasive alternative to medication for the treatment of brain-related disorders. It works based on the principle of electromagnetic induction. The current is applied through the copper coil wires (as shown in Fig.1) which in turn produces a magnetic field. The magnetic field pulse delivered by a stimulating coil applied on the scalp can pass through the skull bone to generate an electric field. After development of the first TMS [6], other studies have accompanied to improve and optimize the complex design of the TMS for specified purposes [7].

It has been shown that various parameters may influence the efficiency of the TMS. These parameters include the orientation and type of TMS coil [8], and the waveform of the magnetic pulse, which is usually

* Corresponding Author: e.salkim@alparslan.edu.tr

monophasic or biphasic [9]. More importantly, the features (shape and size) of the magnetic coils have an important role in determining the focality and depth of stimulation in the brain. Although the coil with type shape of a number eight (called figure-of-eight-coil (FoE)) is widely used, double-cone coil seems to provide a deeper, stronger, and wider electric field [8]. Targeting a wider area with a double-cone coil may be more appropriate for patients [10].

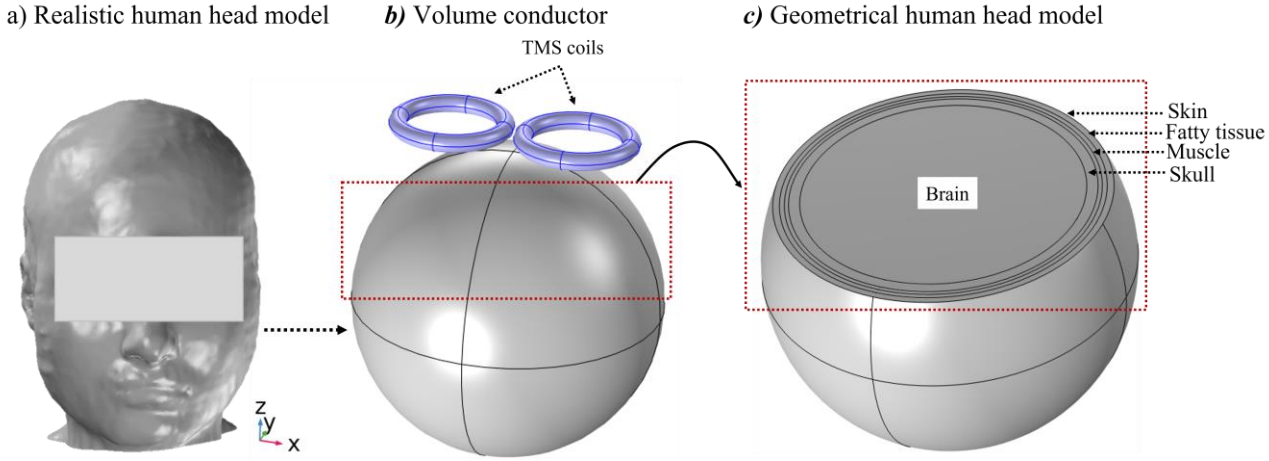

Figure 1. The computational model of the human head and TMS coils. (a) shows MRI-based human head model. (b) shows the spherical head model including the TMS neuromodulator. (c) shows human head tissue layers that are considered in this study. The human head was generated based on the average thickness of each tissue.

Although the importance of TMS has been further enhanced with the advent of new devices capable of repetitive stimulation, however, it has been shown that further improvements are required to have optimal TMS [11]. For example, the users are still complaining about poor focality, too rapid coil heating, and too large coil size [12], [13]. These are might be due to relatively applied higher levels of the current levels. Also, it is also shown that the high current levels heat the coil due to resistive losses and exert considerable mechanical forces in the coil windings, reducing their lifespan and causing a loud coil click [13]. In addition, the deeper structures of the human head can be simulated by applying a stronger electrical current to the coil, but this strategy invariably stimulates a larger brain volume which risks seizure in patients and is thus not allowed for safety considerations [13]. Thus, it is vital to investigate the impact of the magnetic field distribution within the human head layers using different levels of the coil current.

It may not be possible to parametrize TMS features (e.g. coil size and shape and current levels) to optimize TMS settings using experimental studies because of the lack of safety in testing them on human subjects. Alternatively, highly advanced computational methods can be used to optimize such parameters without inducing any risks [13], [14]. Such methods are implemented using finite elements (FE) and models (FEM). It consists of a volume conductor model that represents different structures and the electrodes according to their conductivities and appropriate boundary conditions [14]– [16]. Current commercial FEM software packages (e.g., COMSOL Multiphysics, ANSYS) allow calculating electrical magnetic induction in the computational models.

It has been shown that many coils were designed in the last two decades utilizing different geometrical layouts. The typical coil arrangement is figure-of-eight [1], [5], [17]. Other types of coil design may stimulate a wide region of the human head and this may affect neural populations whose simulation procedures have unwanted or interfering effects [13]. Thus, the typical coil arrangement was designed and used in this study as shown in Fig. 1(b). As proof of concept for TMS features optimization, the electrical magnetic distribution was simulated for two identical coil stimulation arrangements to analyze magnetic field distributions across the human head. It has also been shown that the human head can be represented by concentric geometrical shapes as shown in Fig. 1(b), (c) [8]. Thus, the computational model of the human head was generated based on five concentric geometrical shapes including the brain, skull, muscle, fatty tissue, and skin layers as shown in Fig. 1(c). After attaining the required electrical features of these layers and applying appropriate boundary conditions, the current was applied through the coils to calculate magnetic field distributions across the region of interest (e.g. brain). The results suggested that TMS neuromodulator settings (e.g. current level) may be parametrized and simulated by mimicking the anatomical volume conductor of the human head by applying commercially available TMS settings. It was shown that when the applied current was increased the induced magnetic flux density was also

increased approximately in the same ratio.

The paper is organized as follows; Section II presents the procedure that was used to design to the model; Section III gives the magnetic field induction on the region of interest based on chosen based on coil arrangement using various current levels, and the discussion and conclusion are given in Sections IV and V, respectively.

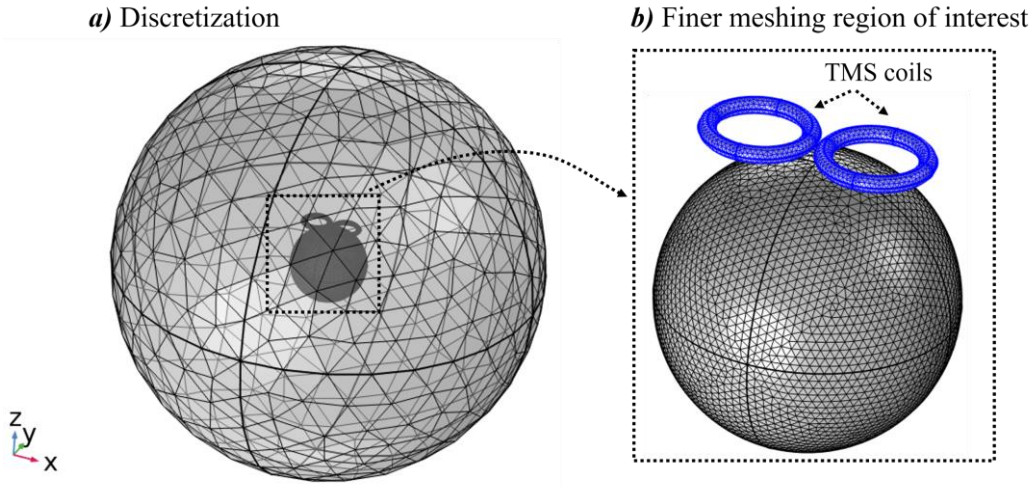

Figure 2. Numerical computation model of volume conductor. (a) Shows discretization of the whole model including air (ground) and fundamental anatomical human head layers. (b) Shows the region of interest meshing plot. The coils and anatomical layers are meshed with finer meshing settings to obtain accurate results. The coils are highlighted.

2. Materials and Methods

2.1. Volume Conductor Model

The computational model was generated using COMSOL Multiphysics (COMSOL, Ltd, Cambridge, UK) based on AC/DC module. The AC/DC module provides a unique environment for the simulation of electromagnetics in 2D and 3D. This module is a powerful tool for detailed analysis of the components of electromagnetism such as coil current and power dissipation. The human-head computational models can be constructed in a range of complexity from concentric sphere models to high-resolution models based on an individual's image data set depending on the clinical question [13]. The anatomically specific image-based head modelling may require extensive prior work on computational modelling. In the studies [12], [11], it has been shown that the geometrical human head (e.g. sphere) can be used instead of an MRI-based highly detailed human head model (as shown in Fig. 1(a)) to analyze the effect of model complexity on the simulation current with less computation cost but more sufficient accuracy. As the clinical question of this study is the same (current range), thus, human head tissue layers and TMS coil electrodes were constructed from geometric shapes in COMSOL Multiphysics (COMSOL, Ltd., Cambridge, U.K.). The head model consisted of five concentric spheres to represent skin, fatty tissue, muscle, skull, and brain as detailed in Fig 1(b). The human head volume conductor was generated based the anatomical layers' average thickness based on Table 1. The brain layer was designed based on the average human head brain diameter. The coils were represented by the relative diameter and merged with the volume conductor. It is noted that the distance between the coils was equal, and the coils were identical. Also, the coils are both rotationally symmetric and symmetric about the z = 0 planes.

Table 1. Anatomical layers properties, r: radius.

Tissue layer	Conductivity (S/m)	Thickness (mm)
Skin	$2e^{-4}$	2.8
Fatty tissue	$4.24e^{-2}$	2
Musle	$3.32e^{-1}$	1.7
Skull	$2e^{-2}$	4.5
Brain	$4.75e^{-2}$	r = 77.5
Coil	$5.998e^{7}$	r = 5

2.2. Simulation Set-up and Boundary Conditions

A large diameter-based sphere was generated to represent air. A boundary layer was defined around the air layer to mimic the infinite domain as shown in Fig.2(a). These boundaries were insulated during the simulation to obtain accurate results.

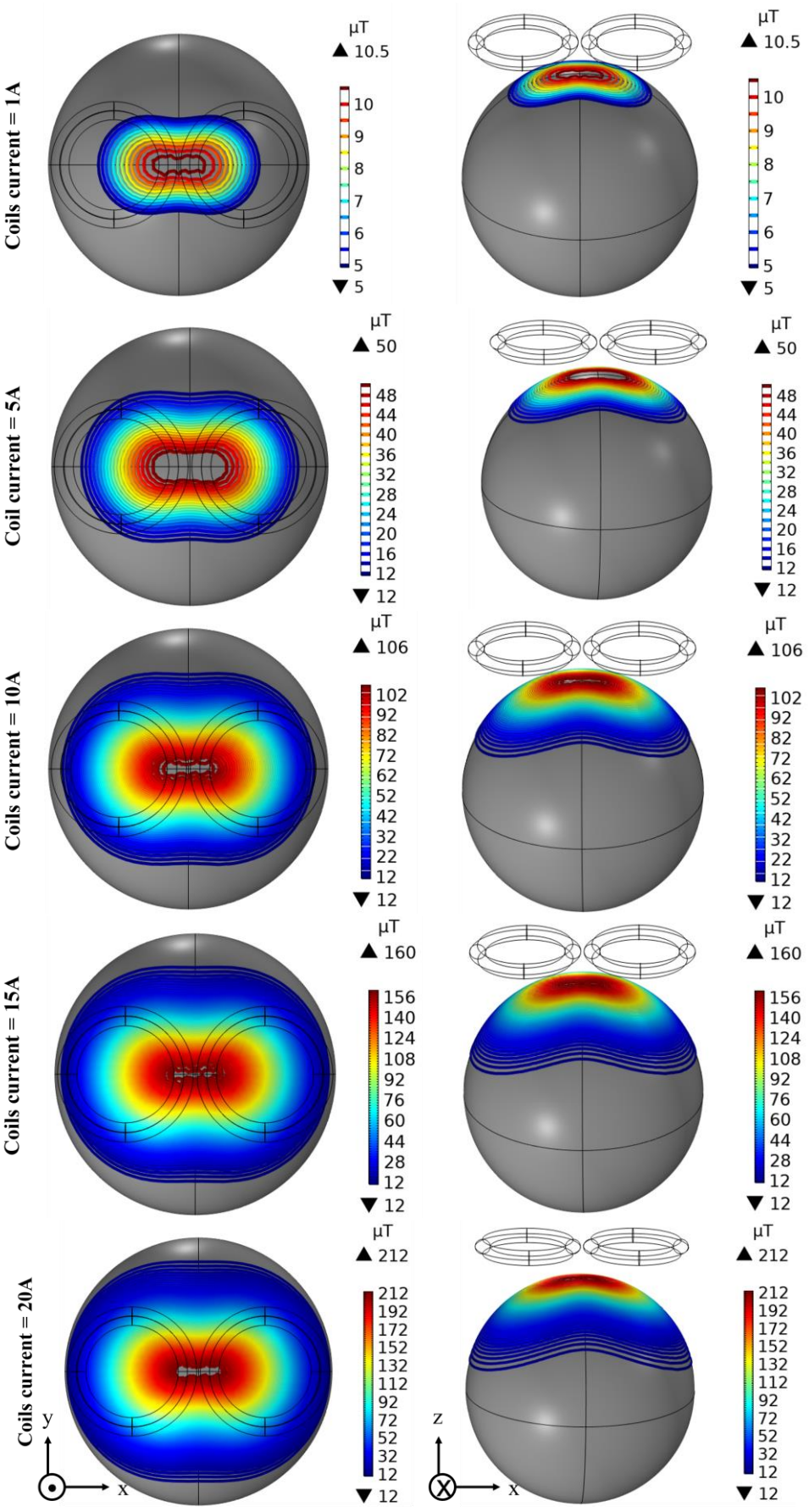

Figure 3. Magnetic flux distribution based on various coil current levels. The results are shown on the brain layer.

Since the TMS neuromodulator device works based on the low-frequency range, the dielectric properties of the anatomical layers were attained based on low frequency using Table 1. Since the results were calculated based on the quasi-static approximation, the tissue permittivity was neglected. After generating a volume conductor, the dielectric properties of each tissue layer were attained. Then, various current levels (1 A, 5 A, 10 A, 15 A, 20 A) were defined for coils. The volume conductor simulated each current level by defining the current direction in the coil in COMSOL. The magnetic flux density was calculated for each current level to examine the impact of the current levels on the magnetic flux distribution on the human head. It is noted that the direction of the coil current was defined for each coil to simulate magnetic simulation. The *coil domain* feature was added to the model to specify the direction of the current within the coil. The current flow direction was defined by including a *geometry analysis* sub-feature of the coil domain. The distance between the coils and the human head was set at a constant value to obtain a fair comparison. It is noted that the same coils were used for all current levels.

The magnetic field distributions on the brain layer's edges may provide useful guidance for neuromodulator design. Thus, the magnetic flux density on the edges of the brain layers was analyzed.

To investigate the impact of the coil vertical distance to the skin layer, the coil was placed at the different distance (*4d, 3d, 2d, d*) to the skin layer and the magnetic field distributions over the brain layers was measured. It was noted that the coil current was kept constant to solely analyze the effect of the coil distance to the anatomical layers based on magnetic field distributions.

2.3. Finite Element Magnetic Simulation

The FEM was used to solve the electrical magnetic distribution in each medium. Each completed head model was simulated by dividing the geometry between the model into a mesh of small elements and solving the underlying equation for each element separately but in relation to each other in the COMSOL Multiphysics modelling environment. The domains in the volume conductor were discretized using free tetrahedral meshing settings. The region of interest was more finely meshed, while the rest of the region was relatively coarsely meshed to obtain magnetic distributions on head tissue layers at a reasonable time. In particular, the outermost layer was coarsely meshed using *Normal* meshing settings. The remaining layers were meshed using *Finer* meshing setting by applying a minimum element size of 1 mm. This resulted in about 1 million degrees of freedom. All the simulations were carried out using COMSOL while considering the quasi-static approximation of Ampère's Law's equations (1-3) where H is the magnetic field strength, J represents current density, B is magnetic flux density and A shows magnetic vector potential. σ shows conductivity and E electrical field. It is required as a pre-process to include *coil geometry analysis* in the study to first compute the current direction through the structure. After successfully solving the model, the *Stationary* study method was applied to the volume conductor to extract magnetic flux density on the anatomical layer. Since the brain layer is the region of interest, the simulation results were recorded on this layer as shown in Fig. 3 and 4.

3. Results

The magnetic flux density variation on the brain layer based on various current levels is shown in Fig. 4. The variations are represented with contours.

There is a proportional relation between current levels and induced magnetic flux density. When the current level is increased, the induced magnetic flux density on the anatomical layer shows an identical trend. Also, an increment in the current levels resulted in widespread magnetic flux density over the anatomical layer. It is shown that the maximum magnetic flux density is induced using 20 A while the lowest value is recorded for 1 A. Also, this is valid for the current spreading area on the brain layer. When the distance between the coils and the anatomical layer is increased, the magnetic induction on the brain layer is reduced. Thus, the maximum induction is observed just beneath the coils.

The magnetic flux density on the brain edges is shown in Fig.4. The magnetic flux density is recorded based on arc length in the *xz* and *xz* directions. It is shown a proportional increment with current levels for both directions. The magnetic induction in the *x* direction relatively shows higher variation compared to the *y* direction. The maximum magnetic induction on a certain arc length is about the same for both directions. The magnetic flux density is reduced when it is recorded far away from the coil arrangement.

$$\nabla \times H = J \tag{1}$$

$$B = \nabla \times A \tag{2}$$

$$J = \sigma E \tag{3}$$

The results for the various coil distance to the anatomical layers are shown in Fig. 5. It is shown that when the vertical distance between the coils and the anatomical layers is reduced, the magnetic flux density on the brain layer is inverse-proportionally increased. Although the

induced value of the magnetic flux is increased, however, this is not spreaded to the large region of the brain.

The magnetic flux density variation on the target edges based on different directions is shown in Fig. 6. The magnetic flux density is recorded based on arc length in the xz and xz directions. It is shown that when the distance between the coils and skin layer is reduced, the magnetic flux density inversely increases.

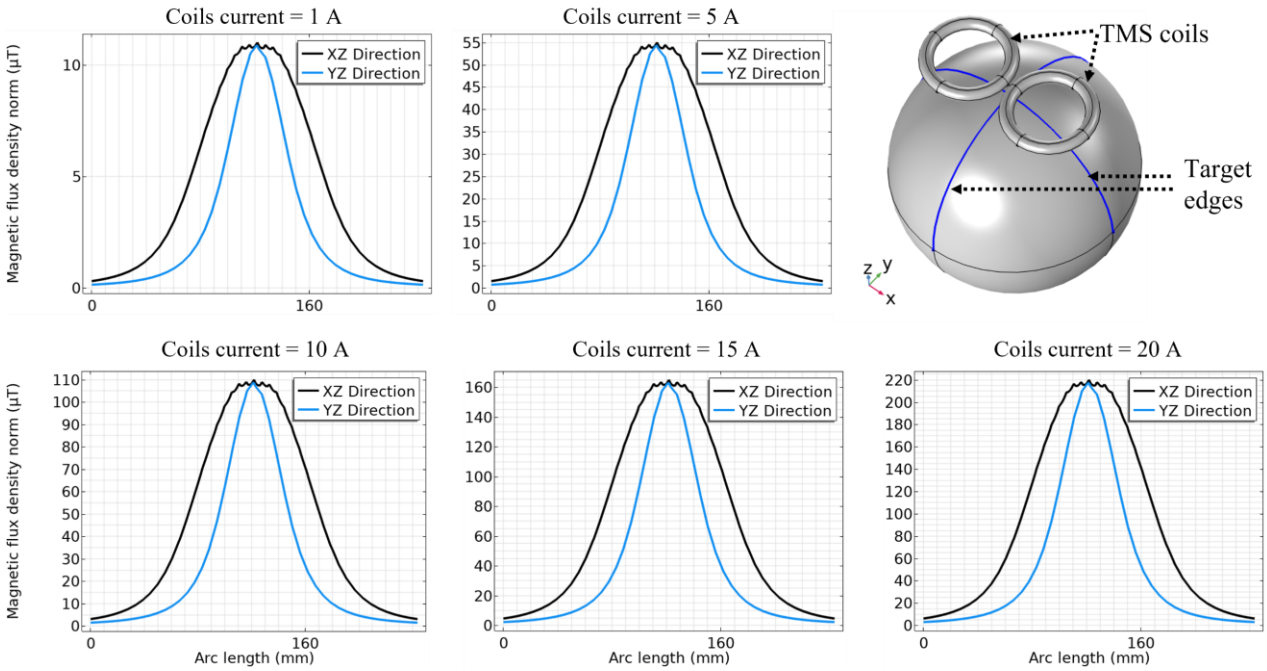

Figure 4. Magnetic flux density variation across target edges based on various current levels. Coil current levels are shown and target edges on the brain layer are highlighted. The edge length is highlighted.

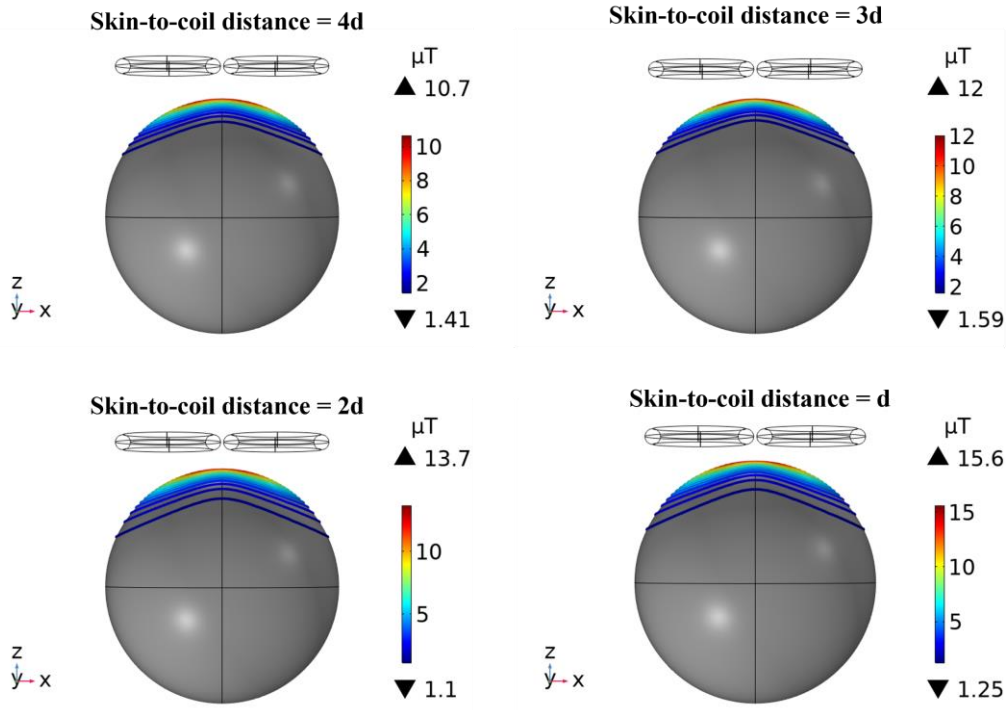

Figure 5. Magnetic flux density variation based on various coil vertical distance to the skin layer. The skin-to-coil distance represents with *d*.

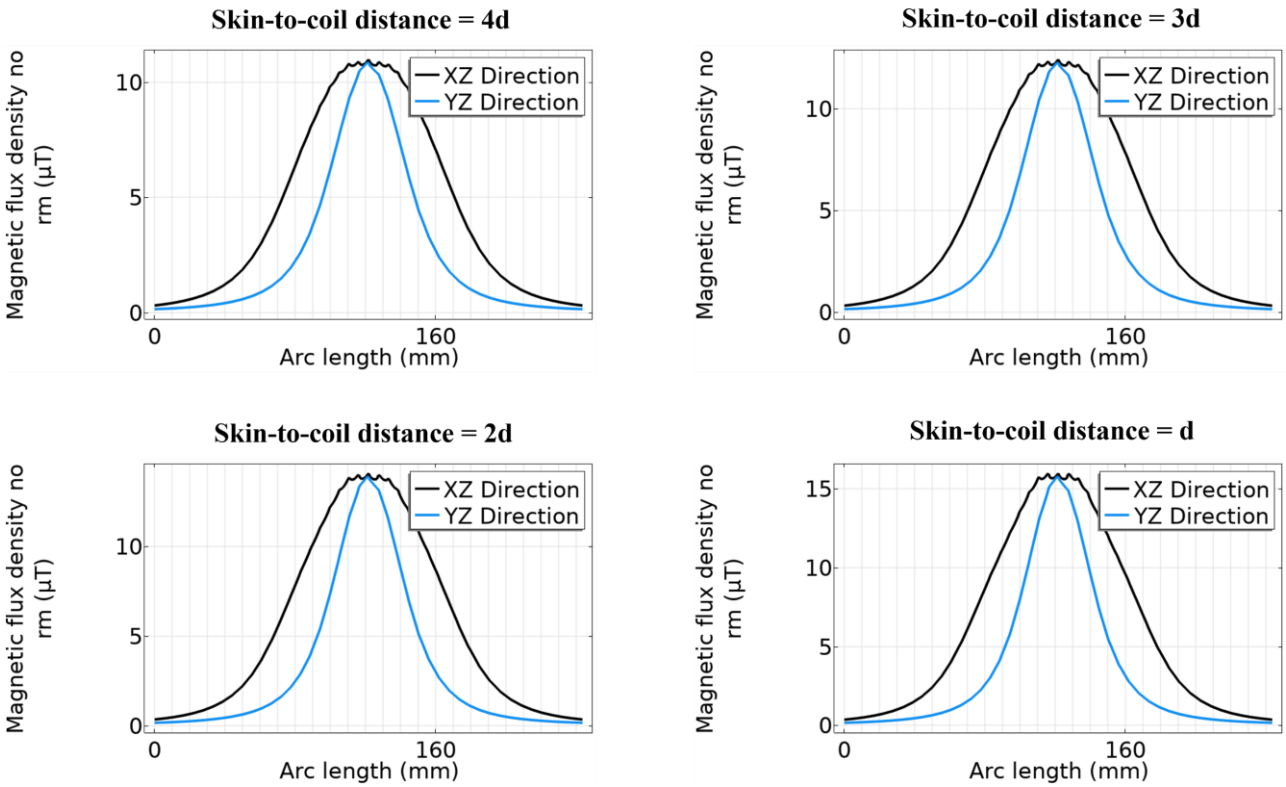

Figure 6. Magnetic flux density variation based on various coil vertical distance to the skin layer for target edges. The skin-to-coil distance represents with *d*.

4. Discussing

The development of neuromodulator therapy systems for neurological disorders has accelerated with improved technologies and with expanding understanding of the effect of electrical stimulation on neural tissue. Computational methods are widely used for advancing and optimizing electrode design, stimulation parameters, and understanding the mechanism of action of these neuromodulator devices. The optimization methods of the TMS are gradually improved [1], [18]–[20]. The results are mixed results. In particular, it has been shown that relatively higher current levels cause coil heating. The advanced computational modelling facilitates a depth and scale of the investigation that may not be possible in experimental tests. Numerical methods have been used as a tool to study electrical stimulation within the volume conductors. The neuromodulator can be designed and developed using these sophisticated computational methods [21].

In this study, the impact of the TMS coils current levels and their distance on the magnetic induction of the human head layers was investigated using such computational methods. The human head was generated based on concentric smooth shapes to examine the magnetic field distribution on the human brain layer. The various coil current levels were applied and the volume conductor was simulated and results were recorded for each current level. Then, the impact of the coils distance to the skin layer was also investigated.

The results suggested that there was a direct relation between current and induced magnetic flux density. When the current increased ten times, the induced magnetic flux density also approximately increased ten times as shown in Fig. 3 and 4. The same trend was observed for all the applied current levels. As shown in Fig. 4, the induced magnetic flux density was relatively higher in the *x* direction compared to the y direction. This is maybe associated with the coil design as coils occupied more area in the *y* direction.

Theoretically, it has been approved that the magnitude of the induced magnetic field was decayed far away from the coil. The computational study also concluded that the magnetic flux density was significantly reduced when it was recorded far away from the coil arrangements as shown in Fig. 3 and 4. It was shown in Fig. 5 that the spreading of the magnetic flux did not change after a certain distance (e.g., the spreading results are similar for *2d* and *d* distances)

Overall, the results of this study suggested two significant deductions. i) Since the current level is proportional to the induced magnetic flux density, coils should be designed based on higher current levels if the larger region of the brain is targeted. ii) Coils should be designed based on axes based on the region of interest. For example, if the region of interest is in the *x* direction, then the coils should be designed in the *x* direction, iii) It was shown that magnetic flux density was not change after a

certain coil distance to the skin layer.

This study investigated a range of current levels and impact of the coils distance to the anatomical layer. It may be required to analyze more current levels to conclude the results. Also, the distance between the volume conductor and coils and the diameter of the coils may have a significant impact on the results. The results of the associated parameters may have a significant impact on the neuromodulator design. Thus, the future of current study is to analyze the impact of these parameters on the optimization of the neuromodulator settings using computational modeling.

5. Conclusion

TMS is a non-invasive neuromodulator that has been approved for neuropsychiatric disorders. The therapeutic efficacy of TMS treatment has been modest, despite decades of research. Many potential reasons cause the limitation of these procedures. One prominent example is using relatively higher current levels that may cause discomfort or activate unwanted neuroanatomical structures. Thus, the human head model based on geometric shapes was generated and merged with the conventional coil arrangements to investigate the impact of the current levels on the region of interest. The result showed that the applied current levels and the distance between the simulating coils and the skin layer have a substantial impact on the outcomes.

More accurate results and detailed conclusions may be drawn by modelling the neuromodulator settings including coils size, different simulation frequency range and considering neuroanatomical layer variations. The results can in turn be used to design a more effective neuromodulator based on the specific effects of the variations.

Declaration of Ethical Standards

The authors of this article declare that the materials and methods used in this study do not require ethical committee permission and/or legal-special permission.

Conflict of Interest

The authors declare that they have no known competing financial interests or personal relationships that could have appeared to influence the work reported in this paper.

References

[1] L. M. Koponen, J. O. Nieminen, T. P. Mutanen, M. Stenroos, and R. J. Ilmoniemi, 2017. Coil optimisation for transcranial magnetic stimulation in realistic head geometry. Brain Stimulation, **4**, pp. 795–805.

[2] M. Ghannad-Rezaie, P. M. Eimon, Y. Wu, and M. F. Yanik, 2019. Engineering brain activity patterns by neuromodulator polytherapy for treatment of disorders. Nature Communications, **10**, pp. 1–13.

[3] J. J. Mahoney, C. A. Hanlon, P. J. Marshalek, A. R. Rezai, and L. Krinke, 2020. Transcranial magnetic stimulation, deep brain stimulation, and other forms of neuromodulation for substance use disorders: Review of modalities and implications for treatment. Journal of the neurological sciences, **418**, p. 117-149.

[4] T. Denison and M. J. Morrell, 2022. Neuromodulation in 2035. Neurology, **98**, pp. 65–72.

[5] P. Rastogi, E. G. Lee, R. L. Hadimani, and D. C. Jiles, 2017. Transcranial Magnetic Stimulation-coil design with improved focality. Aip Advances, **7**.

[6] Kraus, Karl H., et al., 1993. The use of a cap-shaped coil for transcranial magnetic stimulation of the motor cortex. Journal of Clinical Neurophysiology, **10.3**, pp. 353-362.

[7] Roth, Y., Zangen, A., & Hallett, M., 2002. A coil design for transcranial magnetic stimulation of deep brain regions. Journal of Clinical Neurophysiology, **19,** pp. 361-370.

[8] Lontis, E. R., Voigt, M., & Struijk, J. J., 2006. Focality assessment in transcranial magnetic stimulation with double and cone coils. Journal of Clinical Neurophysiology, **23**, pp. 463-472.

[9] Maeda, F., Keenan, J. P., Tormos, J. M., Topka, H., & Pascual-Leone, A., 2000. Interindividual variability of the modulatory effects of repetitive transcranial magnetic stimulation on cortical excitability. Experimental brain research, **133**, pp. 425-430.

[10] Kumru, H., Benito-Penalva, J., Valls-Sole, J., Murillo, N., Tormos, J. M., Flores, C., & Vidal, J., 2016. Placebo-controlled study of rTMS combined with Lokomat gait training for treatment in subjects with motor incomplete spinal cord injury. Experimental brain research, **234**, pp. 3447-3455.

[11] Mosayebi-Samani, M., Jamil, A., Salvador, R., Ruffini, G., Haueisen, J., & Nitsche, M. A., 2021. The impact of individual electrical fields and anatomical factors on the neurophysiological outcomes of tDCS: A TMS-MEP and MRI study. Brain stimulation, **14(2)**, pp. 316-326.

[12] Pascual-Leone, A., Rubio, B., Pallardó, F., & Catalá, M. D., 1996. Rapid-rate transcranial magnetic stimulation of left dorsolateral prefrontal cortex in drug-resistant depression. The Lancet, **348(9022)**, pp. 233-237.

[13] Lu, C., Deng, Z. D., & Choa, F. S., 2022. Augmenting Transcranial Magnetic Stimulation Coil with Magnetic Material: An Optimization Approach, **01**.

[14] Salkim, E., Shiraz, A., & Demosthenous, A., 2019. Impact of neuroanatomical variations and electrode orientation on stimulus current in a device for migraine: A computational study. Journal of neural engineering, **17(1)**, pp., 016006.

[15] Salkim, E., 2022. Analysis of tissue electrical properties on bio-impedance variation of upper limps. Turkish Journal of Electrical Engineering and Computer Sciences, **30(5)**, pp. 1839-1850.

[16] Salkim, E., Zamani, M., Jiang, D., Saeed, S. R., & Demosthenous, A., 2022. Insertion guidance based on impedance measurements of a cochlear electrode array. Frontiers in Computational Neuroscience, **16**, pp. 862126.

[17] Ruohonen, J., Virtanen, J., & Ilmoniemi, R. J., 1997. Coil optimization for magnetic brain stimulation. Annals of Biomedical Engineering, **25**, pp. 840-849.

[18] Gutierrez, M. I., Poblete-Naredo, I., Mercado-Gutierrez, J. A., Toledo-Peral, C. L., Quinzaños-Fresnedo, J., Yanez-Suarez, O., & Gutierrez-Martinez, J., 2022. Devices and Technology in Transcranial Magnetic Stimulation: A Systematic Review. Brain Sciences, **12(9),** pp. 1218.

[19] Xu, Y., Zhang, J., Xia, S., Qiu, J., Qiu, J., Yang, X., ... & Yu, Y., 2022. Optimal design of transcranial magnetic stimulation coil with iron core. Journal of Neural Engineering, **19(2)**, pp. 026046.

[20] Dannhauer, M., Huang, Z., Beynel, L., Wood, E., Bukhari-Parlakturk, N., & Peterchev, A. V., 2022. TAP: Targeting and analysis pipeline for optimization and verification of coil placement in transcranial magnetic stimulation. Journal of neural engineering, **19(2)**, pp. 026050.

[21] Salkim, E., Shiraz, A., & Demosthenous, A., 2018. Influence of cellular structures of skin on fiber activation thresholds and computation cost. Biomedical Physics & Engineering Express, **5(1)**, pp. 015015.

Koc. J. Sci. Eng., 7(1): (2024) 71-80 https://doi.org/10.34088/kojose.1095837

Kocaeli University

Kocaeli Journal of Science and Engineering

http://dergipark.org.tr/kojose

Energy Consumption at Accommodation Buildings: A Case Study of a Boutique Hotel-Abdera

Gildis TACHİR [1, *], Meryem ALTINÖZ [2], Esma MIHLAYANLAR [3]

[1] *Department of Arctitecture, Trakya University, Edirne, 22100, Turkey,* ***ORCID:*** *0000-0003-4863-4339*
[2] *Architect, Balıkesir, 10000, Turkey,* ***ORCID:*** *0000-0002-1452-4994*
[3] *Department of Arctitecture, Trakya University, Edirne, 22100, Turkey,* ***ORCID:*** *0000-0002-0020-2839*

Article Info

Research paper

Received : *March 30, 2022*
Accepted : *December 13, 2023*

Keywords

Accommodation buildings,
Boutique Hotel,
Energy consumption,
Active solar energy systems,
Carbon emission

Abstract

Global environmental problems such as decreasing biodiversity, natural disasters, climate change, and energy consumption are among the main concerns of the countries. Approximately 50% of the energy consumed worldwide is spent on architectural construction, use, and operation. The increase in energy consumption in buildings especially has taken the reduction of carbon footprint and the importance of energy efficiency to the fore. Physical environment, climate, orientation, envelope, and material properties are among the different factors in determining energy consumption in buildings. The share of tourism activities in total emissions is estimated to be 5%. However, it is also stated that tourism buildings have a share of 21 % of $C0_2$ emissions. This work aimed to research the energy consumption of a boutique hotel in Abdera, Greece. ArchiCAD, Graphisoft, and EcoDesigner software were used in the analysis of findings, and suggestions were put forward. Energy consumption and environmental effects were investigated when active solar systems (Solar Thermal Panel /STP (30 m^2), Photovoltaic Panel/PV (30 m^2)) were added to the roof surface (total 60 m^2 Panel) of the building. The analysis showed that the addition of active solar systems by 30% could reduce emissions. In Greece, which is located in a very favorable region in terms of geographical features, it is very important to use solar potential with integrated systems in buildings to provide energy needs.

1. Introduction

The growth of environmental problems on a global scale is indicated in the Brundtland Report published by the World Commission on Environment and Development (WCED) in 1987 [1]. The publication of the report entitled *"Our common future"* has ensured that worldwide environmental problems such as biodiversity, natural disasters, climate change, and energy consumption are at the top of the agenda of the world countries. In this regard, having respect for the right to life of the planet and future generations comes to the fore in the studies entitled "environment" in terms of adopting approaches to the effective use of living resources.

Energy supply is increasing on the scale of regions over the world day by day. As the primary energy supply approaches 15000 Mtoe, it is observed that non-renewable/fossil resources are used as the main resources [2], (Figure 1).

Currently, studies are being focused on the use of renewable energy resources such as solar, wind, etc., and integrating these resources into buildings to meet energy needs in buildings. Renewable resources are used as much as possible by passive and active methods, especially in regions with high solar energy potential [3-5].

It aims to create a low and zero-emission building stock by 2050 and to reduce greenhouse gas emissions by 80%-95% compared to 1990. Measurable milestones will be determined for 2030 and 2040 and national road maps will be created to ensure that buildings are decarbonized. Building energy efficiency becomes prominent in reducing energy losses and negative environmental impacts against an increasing building stock. At the COP 27 conference, which took place recently, solutions for achieving decarbonization were discussed.

* Corresponding Author: gildistahir@trakya.edu.tr

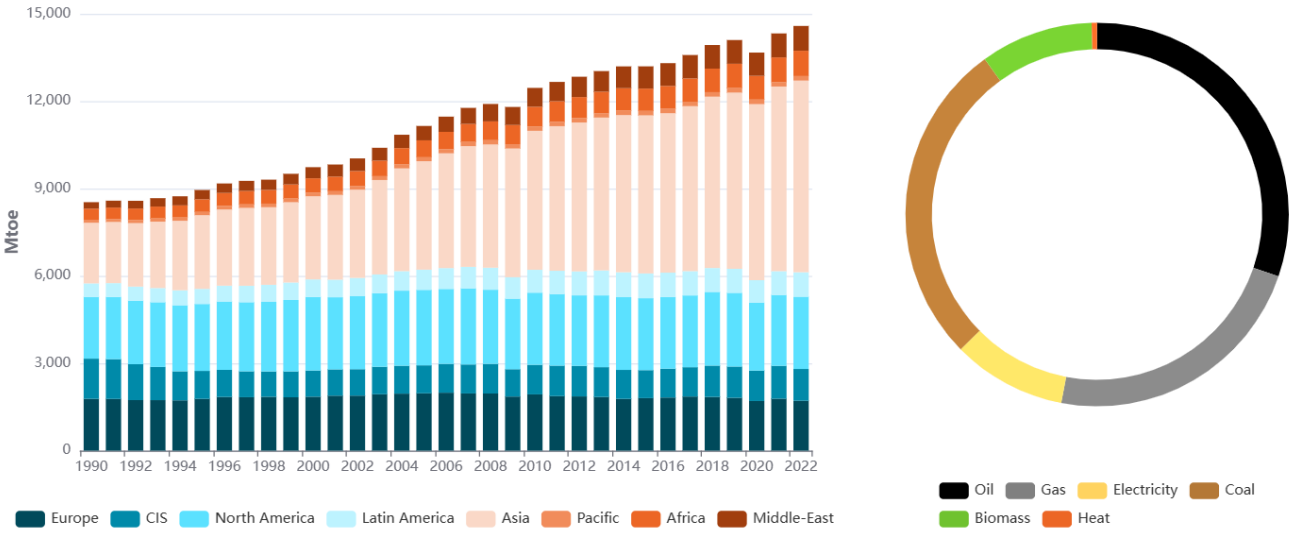

Figure 1. Primary energy supply and energy resource worldwide [2].

Although the science of ecology, which we can call environmental science, has emerged as a branch of biology, it has now transformed into an interdisciplinary field [6- 7]. At this point, the discipline of architecture, which is obliged to regulate the environment, spends about 50% of the energy consumed worldwide in the processes of building construction, use, and operation [8]. In this sense, it will be useful to research the life cycles and environmental effects of buildings designed by architects. Different building typologies serve different functions within the discipline of architecture. In particular, the tourism sector, which grew all over the world before the global pandemic, also led to a rapid increase in accommodation buildings [9-10]. Due to this fact, big accommodation buildings whose numbers increase rapidly consume energy and natural resources (use of materials), and produce waste, can have harmful effects on the natural environment. The share of tourism activities in total emissions is estimated to be 5% [11]. However, it is also stated that tourism buildings have a share of 21 % of $C0_2$ emissions. [5], [12]. High energy consumption is observed in hotels due to their operational characteristics, unlike other buildings [13]. This is mainly due to the need for air conditioning, cooking and a high rate of water use, etc [14]. With the energy consumption of these buildings, their environmental impact also increases [7].

This work aimed to examine the energy consumption of a boutique hotel in Greece. The energy efficiency and environmental effects to be achieved by integrating active solar systems into the building have also been calculated. The effect of active systems used in combination with passive methods in providing energy efficiency in settlements with high solar potential has been studied. Figure 2 also shows the stages followed in the study.

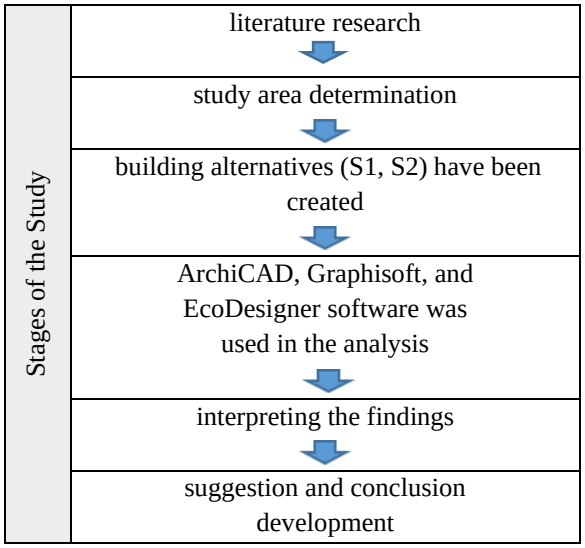

Figure 2. Stage of study

2. Literature Review: Accommodation Buildings

The activity of accommodation is a temporary stay at a place during a journey continuum. This static action is fulfilled by the discipline of architecture with *"accommodation buildings"*. Accommodation buildings have developed throughout history depending on changing environmental conditions. With the spread of railways in the 19th century, inns and caravanserais, which were accommodation buildings of previous centuries, were replaced by city hotels; while in the 21st century, they became boutique hotels, motels, star hotels, and resorts [15].

In the 21st century, with the consistent increase in environmental problems that began in the 1970s, it seems that the concept of energy consumption and comfort conditions of boutique hotels have started to be among the research topics [16]. In this century, where sensitivity to

environmental resources is at the forefront, the concept of *"boutique hotel"* should be evaluated with an understanding respectful to humanity, aiming to use existing materials and energies effectively with the idea of efficient energy consumption and providing comfort conditions, evaluating environmental data with a minimum waste understanding, and aiming to transfer natural resources to future generations without deterioration.

There is no clear definition of a boutique hotel. In general, the common interpretation of all definitions is that boutique hotel units are small and have a unique design. They also vary in scale depending on country and location [17]. When we look at the definitions of Boutique Hotels in recent years, it is seen that the definitions coincide with the tourism demands of the period. With the reflection on the concepts of sustainability and energy efficiency in the tourism literature, it is seen that studies on environmental sensitivity have increased after 1990 [18]. The environmentally sensitive tourism approach has brought with it an understanding of environmentally friendly buildings. In this sense, the concept of a boutique hotel, one of the accommodation typologies, has also changed in parallel with the expectations of the period. It is seen that the scale of the boutique hotel has been reduced and definitions have been made considering visitor habits. According to Nobles and Thompson (2001), "Boutique hotels are hotels with a maximum of 100 rooms, a friendly atmosphere, personalized service, friendly attitude of staff and management, and excellent service that knows what the customer wants at what time". Looking at the common features of the definitions in later years in the same context, it is defined as a type of accommodation with max. 100 rooms, where individuality is at the forefront, comfort is provided, and a sensitive approach to people and the environment is adopted [19-30].

From the general concept analysis, it is concluded that the future hotel typology will be a boutique hotel. It is expected that boutique hotels, which are among the hotel concepts that will be preferred in the future, will respond to worldwide problems in terms of energy consumption and comfort condition approaches. It is expected for the approach of minimizing energy consumption to be adopted, since the increase in energy consumption has taken the reduction of carbon footprint and energy efficiency to the fore, especially in buildings. In this sense, when looking at the factors that determine the energy consumption of a boutique hotel, it can be seen that there are many factors like material properties, climate, physical environmental data, building envelope, orientation, etc.

The Building Energy Performance Directive was published by the European Union (EU) in 2002 and its revision in 2018, with the aim of increasing the energy performance in buildings [31]. This Directive aims to improve the energy performance in new and existing buildings, evaluate the applicability of renewable energy sources, limit greenhouse gas emissions and calculate energy performance, use energy efficiently and effectively, and protect the environment [32]. In addition, buildings are certified on a global scale in terms of sustainability, energy efficiency, environmental effects, user health, and comfort (LEED, BREAM, Green Star, etc.). In this concept, to ensure this in our country in 2008, the accommodation establishments were planned and realized in an environmentally friendly manner along with the adaptation of the facility to the environment, ecological architecture, awareness of the environment, providing training, and cooperation. The relevant institutions and organizations were given "Environmentally Friendly Accommodation Facilities with Tourism Management Certificate". The Communiqué on Granting the Certificate was issued and the "Green Star" project was implemented [33], [34]. In the Green Star scoring system, energy and ecological architecture constitute half of the total score, and the most effective title was determined as energy [35]. Similarly, in a European Country – Greece -, the Building Energy Performance Directive was adapted and published in 2020 [36]. In Greece, energy-efficient building performances are adapted for existing or new building revisions. In this sense, passive and active methods are applied, which are among the necessary methods to increase the energy performance in accommodation buildings [37].

Passive solar systems (South orientation, greenhouse, Trombe wall, etc.) are the oldest method used to provide energy efficiency in buildings. Active solar systems, which are used to meet energy needs and make more use of solar energy, are also being gradually developed and widely used today [38]. Active solar systems such as Solar Thermal Panel (STP) and Photovoltaic Panel (Photovoltaic Panel-PV) are the systems used to provide the "hot water and electricity" needs of buildings [39].

3. Materials and Methods

Greece, a tourism country, visited intensively seasonally, was chosen as the study area. Greece is in a very favorable region in terms of geographical features, the study area. Therefore, it has a very rich potential for solar radiation (Figure 3), [40]. It is very important to use the solar potential with integrated systems in buildings and provide energy needs. Greece, as a tourism country, is also affected by environmental problems on a global scale. In the supply-demand relationship, the number of accommodation buildings that can meet the increasing tourist density is also increasing [41], [11].

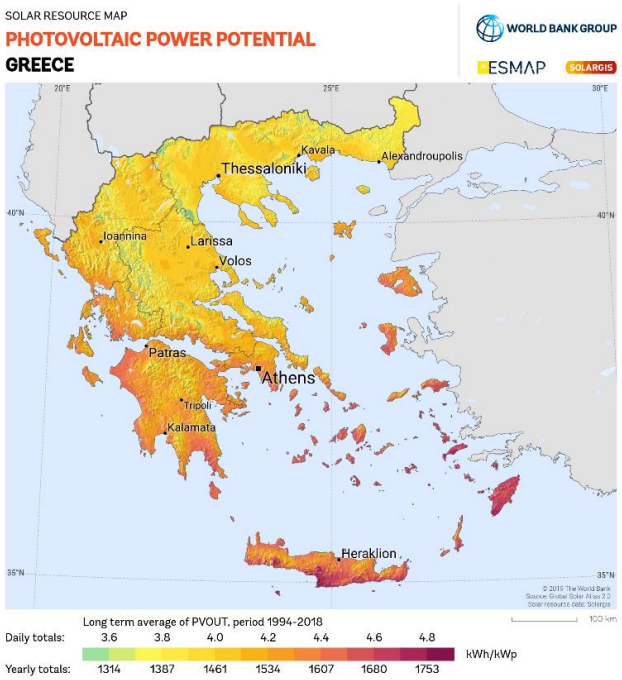

Figure 3. Solar Radiation Map of Greece [40].

The increase in accommodation buildings deteriorate the city's environmental resources [42]. Considering the capacity and characteristics of accommodation buildings, it is possible to exemplify hotels, pensions, boutique hotels, hostels, and chalets [43-45]. In Greece, where mass tourism is effective, with the understanding of improving energy consumption the tourist's interest in environmental tourism has increased, and in parallel, the tendency to small-scale accommodation buildings has increased. In this context, it is important to evaluate all data correctly within the physical environment data and to evaluate the necessary parameters in terms of user comfort by reviewing them in the design phase in boutique hotel buildings to ensure effective energy consumption and comfort. It is vital to take all these conditions into account and implement them at the design stage. It may not be possible for these problems to be solved later, both economically and with applicability.

It is very important to provide energy consumption at the design stage of the buildings within the framework of the efficient use of natural resources. With the decisions to ensure energy consumption and comfort conditions taken during the design phase, energy use will be minimized throughout this whole process, including the stages of design, construction, use/operation, and demolition. This study aimed to examine the energy consumption of a boutique hotel in Greece-Xanthi. According to the findings, it is aimed to identify the problems and develop suggestions for improvement. The data of the sample accommodation building was analyzed using the ArchiCAD Graphisoft EcoDesigner program and suggestions were developed for the findings. Graphisoft Archicad is one of the widely used BIM programs. Climate analysis, building energy model calibration, project-specific low-energy structure solution sets, architectural designs with low energy needs, and complete building energy optimization can be performed through the Eco Designer Star module in the Graphisoft ArchiCAD program. The environmental setting, climate data, and internal gain values of the buildings were introduced to the program. The properties of the building materials modelled in ArchiCAD can be selected from the building catalog. Also, in the program, renewable energy sources (wind, solar, etc.) can be defined for the buildings to evaluate their energy consumption [46]. The energy efficiency and environmental effects to be achieved by integrating active solar systems into the building have also been calculated.

4. Case Study: Abdera and sample building

The Abdera is a coastal city, located in Xanthi, Thrace in Eastern Macedonia, Greece. It is known as the old settlement area. The coastal City-Abdera lay 17 km east-northeast of the mouth of the Nestos River, almost directly opposite the island of Thasos. It was established due to its strategic location and was at the forefront throughout history. The coastal settlement of Abdera controls three passageways: one through the Nestos River, the other through the mountains north of Xanthi, as well as the sea route from its ports from Troas to Thrace and then to the coast of Macedonia [47]. In other words, it was located at the intersection of land, river, and sea passage. The Mediterranean region has a mild climate; summers are hot and dry, while winters are rainy and warm. The average temperature of the hottest months is 34-45 °C, and the average of the coldest months is 8-10 °C. The average annual temperature is 18 °C. Snowfall and frost are very rare. The boutique hotel, located in the coastal city of Abdera, is a two-story building with a basement. There are 3 identical blocks in separate rows in the layout plan. The load-bearing system of the boutique hotel is reinforced concrete, the construction area is 660 m^2 and the floor area is 220 m^2. As vertical mobility, the stairs are designed from the outside and consist of 7 rooms. The rooms are designed in the north and south directions, and each room and bathroom is approximately 20 m^2. On the ground floor, there is a reception desk and 4 rooms, while on the first floor, there are 3 rooms and two terraces opening towards both sides in east and west directions. Figure 4 includes the hotel building's location, plans, and cross-section.

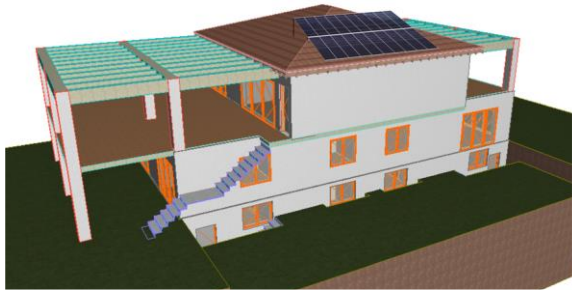

Model View

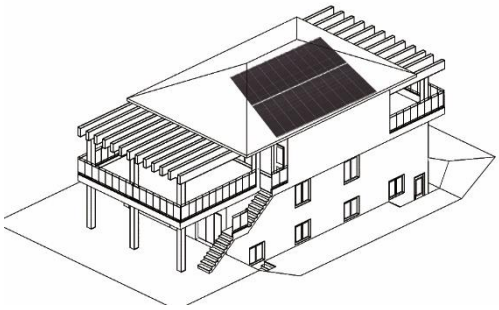

Current View

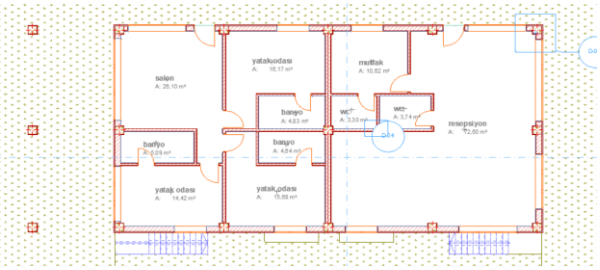

Ground Floor Plan

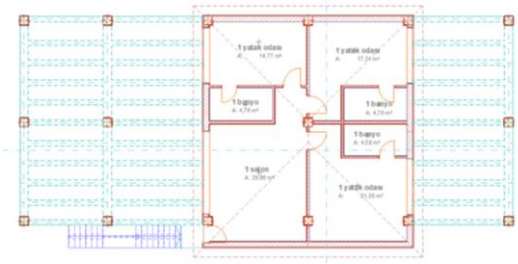

1st. Floor Plan

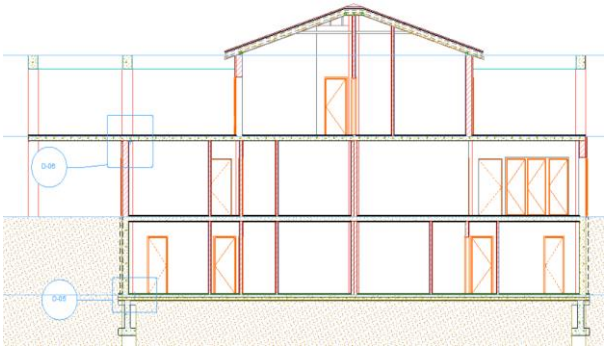

A-A Section

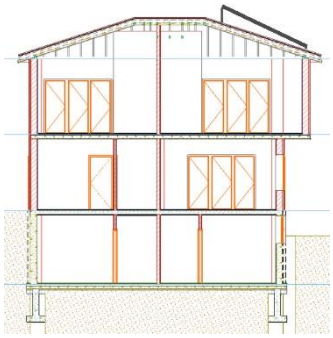

B-B Section

Figure 4. Boutique Hotel Building in Abdera

In the study, models of the building were created using the Graphisoft Archicad program. Afterward, with the Graphisoft Archicad Eco Designer Star module, the thermal transmittance of the building elements forming the building envelope has been calculated as thermally insulated. It is seen that the thermal transmittance / U values of the structural elements of the building are 0.57 W/m^{2}K on the walls, 0.28W/m^{2}K on the floors, 0.84 W/m^{2}K on the ceilings, 0.26 W/m^{2}K on the roof, and 1.7 W/m^{2}K on the windows (Table 1). Within the scope of the study, the annual energy requirement in the well-insulated building envelope (Insulation thicknesses of 5 cm on the wall, 10 cm on the flooring, 3 cm on the mezzanine flooring, and 10 cm on the ceiling) was calculated first in the sample boutique hotel building (S1). Then, as a result of adding a solar collector (Solar Thermal Panel-STP- 30 m^2) and photovoltaic panels (Photovoltaic Panel- PV- 30 m^2) used as active solar energy systems to the roof surface of this building, the energy need was calculated (S2) (Figure 5). Then, the change in energy consumption was evaluated by integrating Solar Thermal Panels and Photovoltaic panels from active solar systems on the roof of this building. It is observed that the active solar systems, used to fulfill the energy and hot water needs of the building, have decreased the energy need of the building.

The fossil-derived fuel oil, a type of fuel that is widely used in the region, was selected as the type of fuel in the building. The renewable solar energy systems to be used in the building after the specified insulation thicknesses are applied are determined as solar collectors (Solar Thermal Panel-STP) and photovoltaic solar panels (Photovoltaic Panel-PV). The solar collector is defined as a discharged tube with an angle of 32º to produce heating and hot water [48]. The photovoltaic solar panel has been preferred with a nominal peak power of 168W/m^2 and an efficiency of 17% in the multi-crystal type [49].

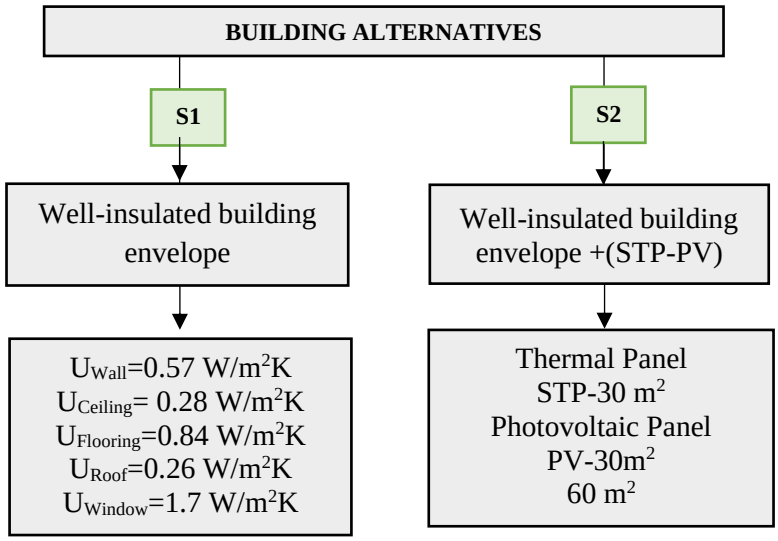

Figure 5. Building alternatives (S1,S2)

Table 1. Thermophysical properties of the building elements that make up the building of the boutique hotel

Building Elements	Material	Thermal Conductivity (W/mK)	Density (kg/m³)	Thermal transmittance U Value (W/m²K)
Wall	Gypsum Plaster	0.57	1300	0.57
	Brick	0.58	800	
	EPS	0.042	15	
	Insulation Plaster	0.3	800	
Ceiling	Tile	1.5	2000	0.28
	Screed Concrete	1.4	2000	
	EPS	0.036	25	
	Concrete	1.15	1800	0.84
	Blockade	0.121	648	
Flooring	Tile	1.5	2000	
	Screed Concrete	1.4	2000	
	EPS	0.036	25	
	Reinforced Concrete – Str.	2.5	2400	
	Gypsum Plaster	0.57	1300	
Roof	Roof Tile	1	2000	0.26
	Membrane	0.23	1100	
	EPS	0.036	25	
	Wood Roof Str.	0.18	700	
	Gypsum Plaster	0.57	1300	
Window	Heat Treated Glass	1	2500	1.7
	PVC Windows	0.17	1390	

Assessing the energy consumption, when 30 m^2 of STP and 30 m^2 PV panels (60 m^2) are added to the roof surface, it is seen that the primary energy consumption of the building was 19979 kWh, and the CO_2 emission corresponding to the energy consumption was reduced to 5448 kg/m^2. This is reflected in the costs in a similar way (Table 2).

Table 2. Energy needs and gains of the boutique hotel insulated (S1) and insulated- STP- PV (S2)

		Building Alternatives	
		Well Insulated S1	Well Insulated+STP+PV S2
Primary Energy (kWh)	A fossil (Fuel Oil)	29027	19979
	Secondary (Electric)	18643	10458
	Secondary (Central Cooling)	130	130
	Renewable (Solar)	0	10953
Annual CO_2 Emission (kg/m²)	Fossil (Fuel Oil)	7916	5448
	Secondary (Electric)	1291	724
Energy Cost (€)	Fossil (Fuel Oil)	1176.80	810.01
	Secondary (Electric)	162.26	91.01

5. Discussion and Conclusion

The increase in energy consumption on a global scale has highlighted the importance of energy efficiency and carbon emissions reduction, especially in buildings. Energy consumption varies depending on the purpose and scale of use of buildings. Climate, orientation, characteristics of the building envelope, etc. are among other factors affecting energy consumption. It is important to ensure energy efficiency in buildings without compromising user comfort. For this purpose, it is necessary to evaluate the physical environment data correctly and to provide the necessary parameters for user comfort, by considering them at the design stage in accommodation buildings.

Energy consumption analysis was performed in this study on a sample boutique hotel building in Greece showing mild climate characteristics, and the results were obtained by using the existing well-insulated system (S1) first and then adding active solar energy systems (S2) by the ArchiCAD Graphisoft EcoDesigner software are as follows:

- The thermal transmittance U value varies between 0.57 W/m^{2}K on the wall, 0.84 W/m^{2}K on the floor, 0.26 W/m^{2}K on the roof, and 1.7 W/m^{2}K on the window depending on the structural elements insulated in the building. The CO_2 emission of the building, corresponding to the primary energy consumption of 29027 kWh, is 7916 kg/m^2.

When 30 m^2 STP ve 30 m^2 PV Panels (60 m^2 in total) are added to the roof surface of the building:

- The CO_2 emission corresponding to the primary energy consumption of the building of 19979 kWh decreases to 5448 kg/m^2.

In this study of boutique hotel building, the rate of decrease in energy consumption by the refurbishment of the building envelope and addition of the building envelope (well-insulated) and the addition of STP and PV from active solar systems.

Although tourism has positive effects on the economy, it is accepted that it has negative effects on environmental pollution and energy consumption [14].

In conclusion, the annual energy consumption in the examined accommodation building decreased by approximately 30% with the addition of active solar systems (STP and PV). It is also seen that comfort temperatures are ensured for different seasons in terms of indoor temperature in the building envelope.

Similarly, the study examining the energy system optimization, cost, and carbon emissions of a medium-sized hotel in Greece also states that by introducing a Photovoltaic (PV) net measurement system, carbon emissions associated with the energy system can be reduced by 31% [11].

Reducing energy consumption by ensuring energy protection of accommodation buildings that are heavily present in tourism regions is very important from an urban, social, and global point of view. As with all kinds of buildings, ensuring user comfort conditions in these buildings is among the basic requirements. The building envelope selected depending on the climate characteristics directly affects energy conservation. In addition, energy consumption decreases with the integrated use of renewable energy sources such as solar energy in buildings for providing building energy needs. It is also important to develop actions and buildings aimed at reducing the carbon footprint. It is very important to use the solar potential in places such as Greece, which is located in a very favorable region in terms of geographical features, with integrated systems in buildings and thereby provide energy needs. Energy needs are mainly covered through electricity in Greece, while petroleum and natural gas only supplement. The usage of renewable energy sources in the hotel sector is

still low [13]. Solar energy, which will be used to meet the needs, will make an important contribution in many ways on a regional and global scale in terms of the environment, etc.

Declaration of Ethical Standards

The author of this article declares that the materials and methods used in this study do not require ethical committee permission and/or legal-special permission.

Conflict of Interest

The author declares that she has no known competing financial interests or personal relationships that could have appeared to influence the work reported in this paper.

Acknowledgments

This study was presented orally at the International World Energy Conference (IWEC) and only an abstract was published.

References

[1] Dünya Çevre ve Kalkınma Komisyonu (WCED), 1987. Ortak Geleceğimiz Brundland Raporu, BM Çevre Konferansı. Stockholm.

[2]https://yearbook.enerdata.net/totalenergy/World%20consumption-statistics.html. Last access date: 06.08.2023.

[3] Arvind Chel A., Kaush G., 2018. Renewable energy technologies for sustainable development of energy-efficient building, Alexandria Engineering Journal, **57** (2), June, pp.655-669.

[4] Silva L., 2022. Adoption of renewable energy innovations in the Portuguese rural tourist accommodation sector, Moravıan Geographıcal Reports, The Czech Academy of Sciences, Institute of Geonics. journal homepage: http:// www. geonika. cz/ mgr. html https://sciendo.com/article/10.2478/mgr-2022-0002. Last access date: 13.07.2023.

[5] Sarıtaş, T., Akar, G., 2022. Turizmin CO_2 Emisyonuna Etkisi: Panel Veri Analizi, Ekonomi Maliye İşletme Dergisi, **5**(1), pp.104-117.

[6] O'Riordan T., 1976. Environmentalism, ISBN No:0.85086.056.3, Pion Limited, Londra.

[7] Tong, Y., Zhang, R., He, B., 2022. The carbon emission reduction effect of tourism economy and its formation mechanism:an empirical study of china's 92 tourism-dependent cities, Int.J.Environ.Res.Public Health 2022, **19**(3), 1824, p.1-21; https://doi.org/10.3390/ijerph19031824. Last access date: 03.05.2023.

[8] Kim J., Rigdon B., 1998. Sustainable architecture module: qualities, use, and examples of sustainable building materials, edit. Graves J., College of Architecture and Urban Planning, The University of Michigan, National Pollution Prevention Center for Higher Education, Michigan, December, pp.1-43.

[9] Cohen E., 1978. Impact of Tourism on the Physical Environment. Annals of Tourism Research, **5**(2), pp. 215–37.

[10] Croall J., 1995. Preserve or Destroy: Tourism and The Environment. London: Calouste Gulbenkian Foundation, London.

[11] Spiller M., Müller C., Mulholland Z., Louizidou P., Küpper F.C., Knosala K., Stenzel P., 2022. Reducing carbon emissions from the tourist accommodation sector on non-interconnected islands: a case study of a medium-sized hotel in Rhodes, Greece, Energies 2022, **15**, 3801. https://doi.org/10.3390/en15103801 . Last access date: 06.02.2023.

[12] From Davos to Copenhagen and Beyond: Advancing Tourism's Response to Climate Change, UNWTO Background Paper World Tourism Organization (2009).

[13] Xydis G., Koroneos C., Polyzakis A., 2009. Energy and exergy analysis of the Greek hotel sector: An application, Energy and Buildings, **41**, pp.402–406.

[14] Gaglia A. G., Balaras C. A., Mirasgedis S., Georgopoulou E., Sarafidis Y., Lalas D. P., 2007. Empirical assessment of the Hellenic non-residential building stock, energy consumption, emissions and potential energy savings, Energy Conversion and Management, **48**, pp. 1160–1175.

[15] İnceoğlu M., İnceoğlu N., 2013. Otel Tasarımında Yeni Eğilimler, Arredamento Mimarlık, **3**, pp. 61-71.

[16] Hudman L. E., 1992. Turizm ve Çevre, Turizmde Seçme Makaleler:16, İstanbul.

[17] Nobles H., Thompson C., 2001. What is a boutique hotel? hotel online special report. http://www.hotel-online.com/News/PR2001_4th/Oct01_BoutiqueAttributes.html , Last Acces: 9 Kasım 2021.

[18] Mason P., 2016. Tourism Impacts, Planning and Management. Routledge.

[19] Albazzaz A., Birnbaum B., Brachfeld D., Danilov D., Kets de Vries O. J., 2003. Lifestyles of the rich and almost famous: the boutique hotel phenomenon in the

United States, High Tech Entrepreneurship and Strategy Group Project, Insead Business School, Fontainebleau, 5320105, pp.1-50.

[20] Zengel R., 2003. Yerel ile küresel arasında butik otel/tatil köyü ikilemi, Arredamento Mimarlık, **161** (9), pp. 100-105.

[21] Freund de Klumbis D., Munsters W., 2004. Seeking the Ultimate Hotel Experience ESADE Escuela Universitaria de Turismo Sant Ign si.

[22] Victorino L., Verna R., Plaschka G., Dev C., 2005. Service innovation and customer choices in the hospitality industry, Managing Service Quality, **15** (6), pp. 555-576.

[23] Erkutlu H., Chafra C., 2006. Relationship between leadership power bases and job stress of subordinates: example from boutique hotels, Management Research News, **29** (5), pp. 285-297.

[24] Aggett M., 2007. What has influenced growth in the uk's boutique hotel sector? International Journal of Contemporary Hospitality Management, **19** (2), pp. 169-177.

[25] Olga A., 2009. The alternative hotel market, 16th international conference on management science and engineering, Moskova, Rusya, 14-16 September, IEEE, pp.2021-2025, DOI: 10.1109/ICMSE.2009.5317702,

[26] Lim W., Endean M., 2009. Elucidating the aesthetic and operational characteristics of uk boutique hotels, International Journal of Contemporary Hospitality Management, **21** (1), pp. 38-51.

[27] Henderson J. C., 2011. Hip heritage: the boutique hotel business in Singapore, Tourism and Hospitality Research, **11**, pp. 217-223.

[28] Aykol E., Zengel R., 2014. 21st Century new generation accommodation buildings: approach of boutique hotel, Anatolia: Turizm Araştırmaları Dergisi, **25** (2), pp. 211-225, DOI: 10.17123/atad.

[29] Qawasmeh R., 2016. Role of the brand image of boutique hotel for customers choosing accommodation, Le Chateau Lambousa, Case Study, North Cyprus. J Hotel Bus Manage 5, November, **5** (2), p. 1-10. DOI: 10.4172/2169-0286.1000147.

[30] Loureiro, S.M.C., Rita, P. and Sarmento, E.M. (2020), What is the core essence of small city boutique hotels? International Journal of Culture, Tourism and Hospitality Research, **14**(1), pp. 44-62. https://doi.org/10.1108/IJCTHR-01-2019-0007.

[31] EPBD, 2018, Energy performance of buildings directive, https://energy.ec.europa.eu/topics/energy-efficiency/energy-efficient-buildings/energy-performance-buildings-directive_en. Last access date: 28.03.2023.

[32] Hafez F. S., Sa'di B., Safa-Gamal M., Taufiq-Yap Y.H, Alrifaey M., Seyedmahmoudian M., Stojcevski A., Horan B., Mekhilef S., 2023, Energy efficiency in sustainable buildings: a systematic review with taxonomy, challenges, motivations, methodological aspects, recommendations, and pathways for future research, Energy Strategy Reviews, **45**, January, pp. 1-31 DOI: 10.1016/j.esr.2022.101013

[33] Atmaca M., 2016, Avrupa birliği bina enerji performansi direktifi' nin türkiye' deki mevcut otel binalari için uyarlanmasina yönelik bir yaklaşım, İstanbul Teknik Üniversitesi, Fen Bilimleri Enstitüsü Yayınlanmamış Doktora Tezi, İstanbul.

[34] Avşar M., Karakaş Tandoğan G., 2023, Çevre dostu konaklama işletmelerine fazla ücret ödeme eğiliminin kuşaklara göre değişikliğinin incelenmesi, İnsan ve Toplum Bilimleri Araştırma Dergisi, **12** (2), pp. 976-994.

[35] Yurtlu, M., Kar, M., Metin, F. and Güneş, G., 2021. Kalite yönetim ödülü alan otellerin çevreduyarlılık faaliyetlerinin yeşil yıldız kriterleri kapsamında değerlendirilmesi. Journal of Architectural Sciences and Applications, **6** (2), pp. 476-493. DOI: https://doi.org/10,30785/mbud.972912.

[36] Androutsopoulos A., Giakoumi A., Centre for Renewable Energy Sources and Saving (CRES), 2020, https://epbdca.eu/wpcontent/uploads/2022/02/Implementation-of the-EPBD-in-Greece-2020.pdf .Last access date: 28.01.2023.

[37] Öykü Yazgan S., Koçak Soylu S., 2022, Otellerde enerji verimliliğini iyileştirmeye yönelik çeşitli yaklaşimlarin tasarruf oranlarina etkisinin karşilaştirilmasi: Antalya örneği, Journal of Engineering Sciences and Design, **10**(4), pp. 1375 – 1388, DOI: 10.21923/jesd.1063248.

[38] Demircan R. K., Gültekin A. B., 2017. Binalarda Pasif ve Aktif Güneş Sistemlerinin İncelenmesi, TÜBAV Bilim 10, **10** (1), pp: 36-51.

[39] Kaya G. N., Beyhan F., 2021. Integrated design approaches with photovoltaic panels and solar collectors in the building envelope. World Journal of Environmental Research. **11**(2), pp.46-61. DOI: https://doi.org/10.18844/wjer.v11i2.7232.

[40] https://solargis.com/mapsandgisdata/download/greece Last access date: 11.04.2023

[41] Coccossis H., Mexa A., 1997. Coastal management in Greece, Hellenic Ministry for the Environment, Physical Planning and Public Works, Athens. ISBN 0754635694.

[42] Husbands W., Harrison L.C., 1996. Practicing responsible tourism: understanding tourism today to prepare for tomorrow. in practising responsible tourism: International Case Studies in Tourism Planning, Policy, and Development, ed. Harrison L.C. ve Husbands W., pp. 1–15. Canada: Wiley.

[43] Çetin I., 2001. Turistik ürün çeşitlendirmesinde ekoturizmin yapısal analizi ve türkiye'de geliştirme stratejileri, Yüksek Lisans Tezi, Balıkesir Üniversitesi. Balıkesir.

[44] Kohler N., Hassler U., 2002. The building stock as a research project, Building Research and Information, **30**(4), pp. 226-236.

[45] Önder D. E., 1995. Kent otellerinde mekânsal kademelenmenin değerlendirilmesi için bir yöntem, Yıldız Teknik Üniversitesi Fen Bilimleri Enstitüsü, Yayınlanmamış Doktora Tezi, İstanbul.

[46] Shiratuddin M., F., Germany S., Sulbaran T., 2011, Introduction to ArchiCAD, Delmar, ISBN:9781428356658,1428356657.

[47] Samsaris D. C., 2005. Historical Geography of Western Thrace during the Roman Antiquity (in Greek), Thessaloniki 2005, pp. 91-96.

[48] European Commission, PVGIS-Grid Connected, 2017b. https://re.jrc.ec.europa.eu/pvg_tools/en/tools.html#PVP. Last access date: 15.02.2023

[49] Polikristal Güneş Kollektörü, 2022. https://www.solarkutu.com/urun/170w-polykristal-gunes-paneli Last access date: 17.02.2023

Koc. J. Sci. Eng., 7(1): (2024) 81-88 https://doi.org/10.34088/kojose.1363471

Kocaeli University

Kocaeli Journal of Science and Engineering

http://dergipark.org.tr/kojose

The Effect of Laser Power and Laser Exposure Time for Cavity Created on Al_2O_3 Ceramic Surface

Çağla PİLAVCI [1,2,*], Yasemin TABAK [3], Satılmış ÜRGÜN [4], Timur CANEL [5]

[1] *Department of Physics, Kocaeli University, Kocaeli, 41001, Turkey,* ***ORCID:*** *0009-0005-5237-9598*
[2] *TUBITAK Marmara Research Center Life Sciences, Kocaeli, 41470, Turkey,* ***ORCID:*** *0009-0005-5237-9598*
[3] *TUBITAK Marmara Research Center Material Technologies, Kocaeli, 41470, Turkey,* ***ORCID:*** *0000-0002-4912-8828*
[4] *Department of Aviation Electrics and Electronics, Faculty of Aeronautics and Astronautics, Kocaeli University, Kocaeli, 41250, Turkey,* ***ORCID:*** *0000-0003-3889-6909*
[5] *Department of Physics, Kocaeli University, Kocaeli, 41001, Turkey,* ***ORCID:*** *0000-0002-4282-1806*

Article Info

Research paper

Received : *September 20, 2023*
Accepted : *January 17, 2024*

Keywords

Al_2O_3 ceramic
Laser machining
Laser parameters
Surface texture
CO_2 laser

Abstract

Al_2O_3 ceramic materials have many industrial applications, especially because they are wear-resistant. In this study, dimples of different sizes were formed on the surface of ceramic plates with a CO_2 laser. The effects of laser power and laser exposure time on the dimensions of the cavity were investigated. For this purpose, laser powers of 40, 52, 65, 78, 91, and 105 W were applied to the ceramic material for 10 seconds. In addition, 80 W laser power was kept constant and the laser beam was sent to the material for 1, 5, 10, 15, 20, 25, and 30 seconds. High-resolution images of the resulting cavities were taken with an optical microscope. Using the images, the dimensions of the cavities were measured and the effects of laser power and laser exposure time on the cavity geometry were observed. The effects of both laser power and laser exposure duration on the cavity and Heat Affected Zone (HAZ) regions showed similar characteristics. The size of the cavities and HAZ increased almost linearly as laser power increased. However, when the effect of laser exposure duration was analyzed, the increase in cavity sizes slowed down after the exposure duration exceeded 10 s. When the laser exposure duration exceeded 15 seconds, it was observed that the dimensions of the cavities did not change.

1. Introduction

Al_2O_3 ceramics, also known as alumina ceramics or aluminum oxide ceramics, is a type of ceramic material composed mainly of aluminum oxide (Al_2O_3) molecules Alumina is a compound of aluminum and oxygen and is widely found in nature. Alumina ceramics are known for their excellent combination of mechanical, thermal, and electrical properties, making them valuable materials in a wide range of industrial and technological applications [1].

Alumina (Al_2O_3) ceramics are widely used in various technical applications due to their desirable properties. The surface characteristics of Al_2O_3 ceramics play a crucial role in determining their mechanical and bonding properties [2]. demonstrated that the surface roughness of Al_2O_3 substrates significantly influences the bond strength of Ti splats deposited on them [3]. This finding underscores the importance of surface quality in determining the bonding strength of materials to Al_2O_3 ceramics. Furthermore, highlighted the influence of surface properties on bonding quality, indicating that the hardness of the copper powders, rather than the Al_2O_3 surface roughness, significantly affects the bonding quality between the copper coating and the Al_2O_3 layer [4]. Moreover, the mechanical properties of Al_2O_3-based composites can be tailored by varying the content of other materials. For instance, evaluated the mechanical properties of metal matrix composites with different weight proportions of ceramic particles, including Al_2O_3, and found that the mechanical properties varied with the weight proportions of the ceramic particles [5]. This suggests that the mechanical properties of Al_2O_3-based composites can be optimized by adjusting the composition of the composites. In addition, the fabrication and properties of Al_2O_3 ceramics have been extensively studied. highlighted the widespread use of Al_2O_3 as a

* Corresponding Author: cagla.pilavci@gmail.com

ceramic material for technical applications, emphasizing its importance in the field of materials science [6]. Furthermore, investigated the fabrication of transparent Al_2O_3 ceramics using different commercial α-Al_2O_3 powders, demonstrating the potential for tailoring the properties of Al_2O_3 ceramics based on the raw powder used [7].

Alumina ceramics are extremely hard and wear-resistant, making them suitable for applications where components are exposed to corrosive environments or high levels of mechanical stress [8]. They can withstand high temperatures without significant degradation, making them suitable for use in high-temperature environments, such as furnace linings, spark plugs, and crucibles [9]. They have excellent electrical insulation properties, making them useful in applications where electrical insulation is required, such as electronic components and insulators [10]. Alumina ceramics are chemically inert and corrosion resistant, making them suitable for use in chemically aggressive environments [11]. Alumina ceramics are biocompatible, meaning they can be used in medical applications, such as implants and dental prostheses [12]. Alumina ceramics find applications in various industries and technologies, such as electronics, engineering applications, automotive, medical, aerospace, chemical processing, and textile manufacturing; in the electronics industry, for insulators, substrates, circuit boards, and electronic components [13], in mechanical engineering, for cutting tools, ball bearings, seals and wear-resistant parts [14], in the automotive industry, for pistons, valves, sensors, and spark plugs [15], in the medical field, for dental implants, joint replacements and medical instruments [16]. In the aerospace industry, it is used in high-temperature components, thermal barriers and radar windows [17]. They are also used in Chemical Processing, in crucibles, tubes, and liners for high-temperature chemical reactions [18]. In Textile Manufacturing, they are used in guide rollers and yarn guides for textile machinery [19].

Alumina ceramics can be produced by various methods, including advanced techniques, such as sintering, hot pressing, and spark plasma sintering. Different formulations and processing methods can result in differences in properties, allowing alumina ceramics to be customized for specific applications [20].

The surface texture of Al_2O_3 ceramics is of great importance due to its crucial role in shaping the mechanical, thermal and interfacial properties of the ceramic, thus influencing their performance in a spectrum of applications. Controlled manipulation of surface topography offers a versatile way to tailor tribological behavior, enhance adhesion, and optimize heat transfer. By precisely designing surface features, such as roughness, porosity, and microstructures, it becomes possible to increase load-carrying capacity, reduce friction, and improve wear resistance in tribological systems. Furthermore, the deliberate modulation of surface texture affects the thermal conductivity, emissivity, and wettability of ceramics, important attributes in thermal management, energy efficiency, and environmental interactions [21]. The surface texture of Al_2O_3 ceramics plays a crucial role in determining their mechanical, thermal, and tribological properties and thus influences their performance in various industrial applications.The complex interplay between surface topography, microstructure, and composition profoundly affects the functional properties of the ceramic [22]. Al_2O_3 ceramics typically exhibit a microscopically heterogeneous surface morphology characterized by features, such as grain boundaries, crystal facets, and surface defects. These qualities not only contribute to the mechanical strength and wear resistance of the ceramic but also significantly affect their interaction with the surrounding environment. The surface roughness of Al_2O_3 ceramics, resulting from the inherent properties of the ceramic material and the manufacturing processes used, has a direct impact on contact mechanics, friction and adhesion [23]. The presence of micro-scale roughnesses and irregularities on the surface can improve mechanical interlocking and promote close contact between mating surfaces, leading to improved load-bearing properties [24]. In addition, surface texture affects the thermal conductivity and emissivity of the ceramic, which are key considerations in applications involving heat transfer and thermal management [25]. The importance of surface texture becomes particularly evident in contexts where ceramics interface with other materials or media. For example, in biomedical applications, engineered surface textures can improve the biocompatibility and long-term stability of Al_2O_3 ceramic implants by promoting osseointegration, cellular adhesion and bioactivity. Similarly, in electronic packaging and microelectromechanical systems (MEMS), tailored surface topography can ensure reliable adhesion, reduce the risk of delamination and improve the mechanical robustness of Al_2O_3 ceramic substrates [26]. Furthermore, the advancement of surface engineering techniques has led to innovative strategies for creating functional textures, including laser cutting, chemical etching and nanopatterning. These methodologies provide precise control over surface properties at micro and nano scales, enabling the realization of special properties that exceed the inherent properties of the bulk material. As a result, strategically combining surface texturing strategies holds great promise in pushing the boundaries of Al_2O_3 ceramic applications spanning aerospace, automotive, energy, healthcare and beyond [27]. Furthermore, control of

surface texture has become increasingly important in tailoring the performance of ceramics to specific functions. Advanced surface engineering techniques, such as polishing, grinding and surface coatings offer ways to modify surface properties to achieve desired results [28]. For example, precise control over surface roughness can facilitate optimal lubrication, reduce friction losses and improve wear resistance in tribological applications [29]. The importance of surface texture in Al_2O_3 ceramics goes far beyond aesthetics, underlining its crucial role in shaping material behavior and optimizing performance. Leveraging the synergy between surface topography, microstructure and functionality, surface texture is emerging as a transformative tool that empowers the realization of enhanced properties and new functionalities, propelling Al_2O_3 ceramics into the realm of high technological utility and innovation.

Laser surface texturing is a versatile and precision engineering technique that involves the use of laser beams to create controlled patterns, textures or features on the surface of a material, such as Al_2O_3 ceramics [30]. This process offers unique advantages in tailoring surface properties to achieve specific functional outcomes in a variety of applications [31]. Laser surface texturing typically involves focusing a high-intensity laser beam onto the surface of a material. The energy from the laser interacts with the material, causing localized melting, vaporization or ablation. As the laser beam moves across the surface, complex patterns or textures can be produced with micron- or even nanometer-level precision. The resulting surface features can include microscale craters, grooves, channels or other complex geometries. Laser technology provides precise control over the size, depth and layout of surface features, enabling custom designs that optimize specific properties [32]. This level of precision is often difficult to achieve with traditional manufacturing methods. The flexibility of laser surface texturing enables the creation of customized surface patterns to achieve desired properties, such as improved lubricity, reduced friction, increased wettability or controlled adhesion. Laser texturing can improve the tribological performance of materials by reducing friction, wear and contact fatigue. It promotes the formation of oil reservoirs or increases the retention of lubricants within surface features. Laser texturing is often a more environmentally friendly alternative to traditional methods, such as chemical etching or abrasive processes, as it produces minimal waste and avoids the use of harsh chemicals [33]. Laser surface texturing can be applied to a wide range of materials, including metals, ceramics, polymers and composites, making it a versatile technique for a variety of industries.

Alumina, a widely used ceramic material, has been the subject of extensive research in laser applications. Laser treatment has been shown to significantly affect the surface properties of alumina, with laser-treated specimens demonstrating higher surface roughness values compared to untreated specimens [34]. Additionally, laser surface modification has been identified as an advanced technique for improving the surface performance of alumina ceramics in refractory and abrasive machining applications [35]. Furthermore, the use of lasers in the additive manufacturing of alumina ceramic has been investigated, demonstrating the potential for selective laser melting to produce ceramic parts [36]. The high absorptivity of alumina for CO_2 lasers has been highlighted, indicating the effectiveness of high scanning speed and low laser power for the powder bed selective laser processing of alumina [37].

Laser textured surfaces can improve the wear resistance, friction behavior and lubrication efficiency of Al_2O_3 ceramic components, extending their lifetime and reducing maintenance needs. Laser surface texturing represents a state-of-the-art approach to tailoring surface properties, enabling the optimization of Al_2O_3 ceramics and other materials for a wide range of industrial, scientific and medical applications. Its precision, versatility and functional enhancement capacity make it a valuable tool in modern materials engineering and design.

Moreover, laser texturing of zirconia-alumina ceramics has been recognized as a promising surface modification method for various applications, such as enhancing osseointegration of dental implants and improving friction behavior of hip replacement bearing components [38]. The potential practical application of alumina-substrate composites as efficient laser-driven color converters in high-brightness projection displays has also been highlighted [39]. Additionally, laser surface engineering of alumina ceramics has been recognized as an area of technological importance for various applications, with a focus on the effect of laser radiation on the mechanical and physical properties of alumina ceramics [40].

The influence of laser power and laser exposure time on cavity preparation in dentistry has been extensively studied. [41]. Investigated the effects of pump power and laser cavity length on the signal-to-noise ratio performance of an ultrasonic sensor system, providing insights into the influence of laser power on system performance.[42] Attributed changes in cavity surface features to the effects of laser exposure, indicating a direct relationship between laser parameters and cavity characteristics. [43]. Highlighted the increased time required for cavity preparation with lasers compared to high-speed turbines, emphasizing the influence of laser exposure time on the preparation process.

Furthermore, [44]. suggested the potential use of erbium lasers for ablative effects in healthy enamel and dentin, indicating the relevance of laser power and exposure time in cavity preparation. Additionally, [45]. compared the effects of laser cavity preparation with conventional methods on microleakage, providing valuable insights into the impact of laser parameters on restoration quality. These findings collectively underscore the significance of laser power and exposure time in cavity preparation, as they influence cavity characteristics, preparation time, and restoration quality in dentistry.

In this study, micro-sized dimples were formed on Al_2O_3 ceramic plates with a CO_2 laser. The effect of laser processing parameters on the formed dimples was investigated. The effects of laser power and laser exposure time on the dimensions of the cavity were investigated.

2. Materials and Methods

In this study, cavities were formed on 10 mm thick Al2O3 ceramic plates with CO2 laser using different laser power and different laser exposure duration. The laser parameters used in the experiments are given in Table 1. Different laser power of 52, 65, 78, 91 and 105 W were applied to the ceramic material for 10 seconds. In addition, 80 W laser power was kept constant and the laser beam was sent to the material for 1, 5, 10, 15, 20, 25 and 30 seconds.

Table 1. Laser parameters used in the experiments.

Laser Power (W)		52	65	78	91	105	
Laser Exposure Durations (s)	1	5	10	15	20	25	30

3. Results and Discussion

Effect of Laser Power on cavity formation

When the laser power was changed between 52 and 105 W, the laser exposure duration was applied for 10 seconds. When the laser exposure time was changed between 1 second and 30 seconds, the laser power was kept constant at 80 W. In order to examine the change in cavity dimensions with the change in laser power, cavities were formed with laser power 52 W, 65 W, 78 W, 91 W and 105 W as shown in Table 1. Optical microscope images of the formed cavities were given in Figure 1.

The diameter of the laser beam used is 200 µm. Within the laser beam diameter, the energy decreases from the center outwards in a Gaussian distribution. Ablation occurs around the center where the laser beam touches the surface. As it moves away from the center, traces of the heat affected zone (HAZ) can be seen by eye. Using optical microscope images, the average diameters of both the cavity formed as a result of ablation and the heat-affected zone observed in the outer region were measured as shown in Figure 2. The measurement results are given in Table 2.

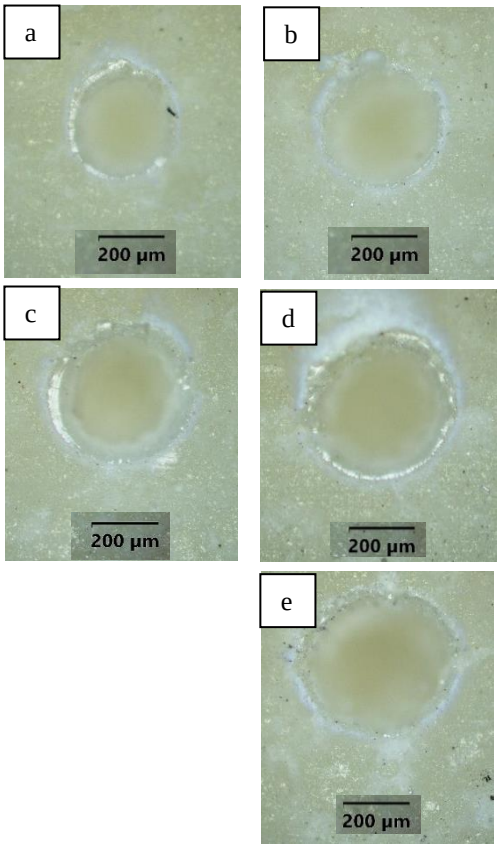

Figure 1. Optical microscope images of the cavities obtained when the laser powers were changed. a) 52 W, b)65 W, c) 78 W, d) 91 W and e) 105 W

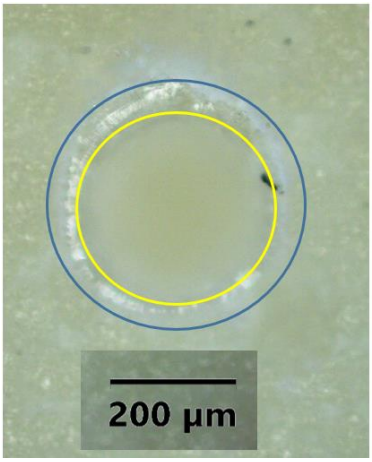

Figure 2. Representative figure showing the measurement of the average diameters of the cavity formed as a result of ablation and the heat-affected zone observed in the outer region (sample obtained with 52 W). The region shown in yellow indicates the approximate boundaries of the cavity obtained by ablation and the region shown in blue indicates the approximate boundaries of the HAZ.

Table 2. Results of the cavity and HAZ diameter measurements against laser power variation.

Laser Power (Watt)	Cavity Diameter (µm)	HAZ Diameter (µm)
52	324	422
65	368	443
78	400	508
91	411	519
105	432	562

The graph showing the change of cavity and HAZ diameters with the applied laser power is given in Figure 3.

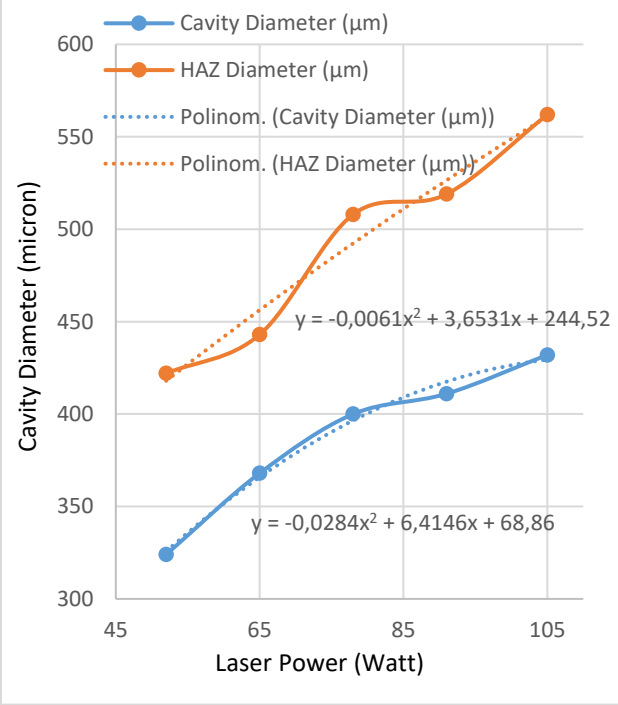

Figure 3. Variation of the cavity and HAZ diameters with applied laser power.

As can be seen from the graphs in Figure 3, as the laser power increases, both cavity and HAZ diameter increase. However, the rate of increase in cavity diameter slows down. As the laser power increases, the increase in HAZ diameter is also clearly seen. However, there is a fluctuation in this increase. One of the reasons for this fluctuation is thought to be due to the irregularity in the structure of the material. The 2nd order trend lines of the graphs and the equations of these lines are also shown in the figure. Although there are differences due to fluctuations, the equations of the 2nd order polynomial trend lines have similar characteristics.

Effect of Laser Exposure Duration on Cavity Formation

To examine the change of cavity size with laser exposure duration, laser exposure duration in Table 1 was applied as 1, 5, 10, 15, 20, 25, and 30 sec and cavities were formed. Optical microscope images of the formed cavities are given in Figure 4.

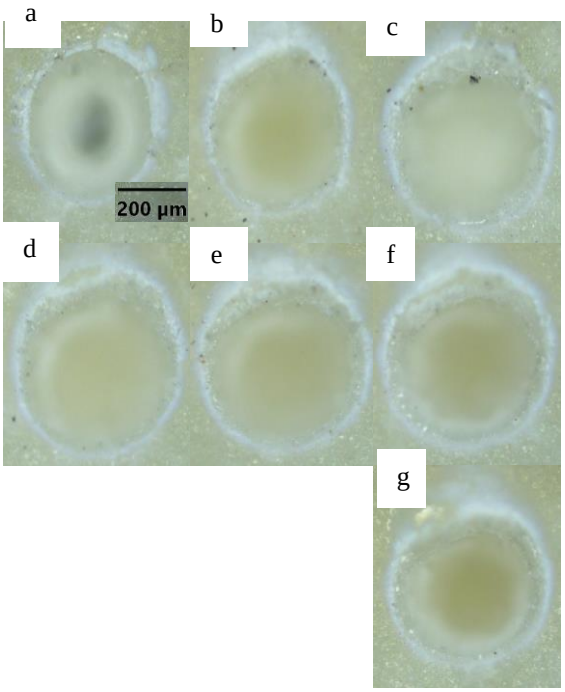

Figure 4. Optical microscope images of the cavities obtained when the laser exposure durations were changed. a) 1 sec, b) 5 sec, c) 10 sec, d) 15 sec, e) 20 sec, f) 25 sec, g) 30 sec.

Optical microscope images were used to measure the mean diameters of both the ablated cavity and the heat affected zone observed in the outer region. The measurement results are given Table 3.

Table 3. Results of cavity and HAZ diameter measurements against laser exposure duration change.

Laser Exposure duration (Sec.)	Cavity Diameter (µm)	HAZ Diameter (µm)
1	389	465
5	400	476
10	432	541
15	443	562
20	443	562
25	443	562
30	443	562

The graph showing the change of cavity and HAZ diameters with the applied laser exposure duration is given in Figure 5.

As can be seen from the graphs in Figure 5, both cavity and HAZ diameters increased exponentially during the first 10 seconds of exposure duration. However, the increase in both diameters slowed down after the 10th second. After 15 seconds, no change was observed in both cavity and HAZ diameter. When the graph is considered as a whole, trend lines have similar characteristics to the equations of 5th-order polynomials.

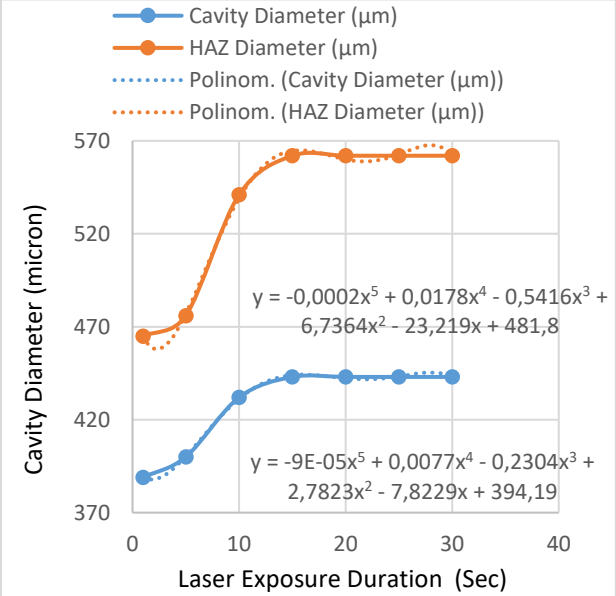

Figure 5. Variation of the cavity and HAZ diameters with applied laser exposure duration

4. Conclusions

In the first part of the study consisting of two parts, when the laser power was increased by keeping the exposure duration constant, the cavity diameters increased almost linearly.

In the second part of the study, laser power was kept constant and laser exposure duration was increased. It was observed that laser exposure duration had no effect on cavity diameters after a certain period of time.

In line with these results;

- It can be said that laser power is a more dominant parameter than laser exposure duration in the dimple geometry to be formed on ceramic material.
- If it is desired to obtain a wider dimple with a fixed laser beam diameter, laser power should be increased.
- If a deeper cavity is desired with an increase in width or a slight increase in width with a fixed laser beam, the laser exposure duration should be increased.

When the duration of laser exposure was increased in the second part of the experiment, both cavity and HAZ dimensions increased during the first 15 seconds, but no change in cavity and HAZ dimensions occurred after the 15th second. This may be due to the change in the thermophysical properties of the material with temperature. The slowing down of the increases in the first 15 seconds may also be evidence of this. As the interaction time increased, the temperature of the material increased and the heat transfer coefficient started to decrease. After a certain frequency value, heat could not be transmitted to further distances within the ceramic material.

Another reason for the inability to transmit heat may be that as the laser application time increases, the amount of heat lost from the surface increases with time.

Declaration of Ethical Standards

The authors of this article declare that the materials and methods used in this study do not require ethical committee permission and/or legal-special permission.

Conflict of Interest

The authors declare that they have no known competing financial interests or personal relationships that could have appeared to influence the work reported in this paper.

References

[1] Parikh P. B., 1995. Alumina Ceramics: Engineering Applications and Domestic Market Potential. Transactions of the Indian Ceramic Society, **54**, pp. 179-184.

[2] Zhu, B., Zhu, Y., Li, X., & Zhao, F. (2013). Effect of ceramic bonding phases on the thermo-mechanical properties of Al2O3–C refractories. Ceramics International, **39(6)**, 6069-6076.

[3] Imbriglio, S. I., Hassani-Gangaraj, M., Veysset, D., Aghasibeig, M., Gauvin, R., Nelson, K. A., ... & Chromik, R. R. 2019. Adhesion strength of titanium particles to alumina substrates: A combined cold spray and LIPIT study. Surface and Coatings Technology, **361**, 403-412.

[4] Huang, L., Yang, Z. H., YAN, L. J., Alhassan, S. I., Gang, H. Y., Ting, W. A. N. G., & Wang, H. Y. 2021. Preparation of 2D carbon ribbon/Al2O3 and nitrogen-doped carbon ribbon/Al2O3 by using MOFs

as precursors for removing high-fluoride water. Transactions of Nonferrous Metals Society of China, **31(7)**, 2174-2188.

[5] Pranavi, U., Venkateshwar Reddy, P., Venukumar, S., & Cheepu, M. 2022. Evaluation of mechanical and wear properties of Al 5059/B4C/Al2O3 hybrid metal matrix composites. Journal of Composites Science, **6(3)**, 86.

[6] Deckers, J. P., Shahzad, K., Cardon, L., Rombouts, M., Vleugels, J., & Kruth, J. P. 2016. Shaping ceramics through indirect selective laser sintering. Rapid Prototyping Journal, **22(3)**, 544-558.

[7] Ogashiwa, Y., Suzuki, Y., Tanaka, K., Okumoto, Y., Kuo, Y. L., & Nanko, M. 2022. Influences of Raw Powder on Transparent Al2O3 Prepared by Two-Step Pulsed Electric Current Sintering. In Journal of Physics: Conference Series (Vol. **2315**, No. 1, p. 012015). IOP Publishing.

[8] Medvedovski, E. 2001. Wear-resistant engineering ceramics. Wear, 249(9), 821-828.

[9] Evans K. A., 1996. The Manufacture of Alumina and its Use in Ceramics and Related Applications. Key Engineering Materials, **122-124**, pp. 489-526.

[10] Li S., Yu S., Feng Y., 2016. Progress in and prospects for electrical insulating materials. High Voltage, **1**, pp. 122-129.

[11] Gutierrez A. V., Cuevas J. L., Angeles A. G., Diaz N. P., 2019. Addition of ceramics materials to improve the corrosion resistance of alumina refractories. SN Applied Sciences, **784**, pp. 1-7.

[12] Patel N. R., Gohil P. P., 2012. A Review on Biomaterials: Scope, Applications& Human Anatomy Significance. International Journal of Emerging Technology and Advanced Engineering, **2**, pp. 91-101.

[13] Murayama N., Hirao K., Sando M., Tsuchiya T., Yamaguchi H., 2018. High-temperature electro-ceramics and their application to SiC power modules. Ceramics International, **44**, pp. 3523-3530.

[14] Liang Y., Dutta S. P., 2001. Application trend in advanced ceramic technologies. Technovation, **21**, pp. 61–65.

[15] Okada A., 2009. Ceramic technologies for automotive industry: Current status and perspectives. Materials Science and Engineering B, **161**, pp 182-187.

[16] Nissan B. B., Choi A. H., Cordingley R., 2008. Alumina ceramics, Bioceramics and their Clinical Applications. Woodhead Publishing Series in Biomaterials, **1**, pp. 223-242.

[17] Nag A., Rao R. R., Panda P.K., 2021. High temperature ceramic radomes (HTCR) – A review. Ceramics International, **47**, pp. 20793-20806.

[18] Roya S. K., Moorthy V. K., 1981. Alumina Special Ceramics. Transactions of the Indian Ceramic Society, **40**, pp. 212-216.

[19] Caldas P., Sousa F., Pereira F., Lopes H., Machado J., 2022. Automatic system for yarn quality analysis by image processing. Journal of the Brazilian Society of Mechanical Sciences and Engineering, **44**, pp.565-590.

[20] Otitoju, T. A., Okoye, P. U., Chen, G., Li, Y., Okoye, M. O., & Li, S. 2020. Advanced ceramic components: Materials, fabrication, and applications. Journal of industrial and engineering chemistry, **85**, pp.34-65.

[21] Liu, Y., Deng, J., Wang, W., Duan, R., Meng, R., Ge, D., & Li, X. 2018. Effect of texture parameters on cutting performance of flank-faced textured carbide tools in dry cutting of green Al2O3 ceramics. Ceramics International, **44**(11), pp.13205-13217.

[22] Della Bona, A. 2005. Characterizing ceramics and the interfacial adhesion to resin: I-the relationship of microstructure, composition, properties and fractography. Journal of Applied Oral Science, **13**, pp.1-9.

[23] Chang, C. W., & Kuo, C. P. 2007. Evaluation of surface roughness in laser-assisted machining of aluminum oxide ceramics with Taguchi method. International Journal of Machine Tools and Manufacture, **47**(1), pp.141-147.

[24] Bobby S., Samad M, A., 2016. Enhancement of tribological performance of epoxy bulk composites and composite coatings using micro/nano fillers: a review. Polymers Advanced Technology, **28**, pp. 633–644.

[25] Ye, C. C., Ma, K., Chen, H. M., Xiang, Z. L., & Wei, W. Q. 2024. Effect of texture on the thermal conductivity and mechanical properties of silicon nitride ceramic. Ceramics International, **50**(2), pp.4014-4021.

[26] Sanghvi, M. R., Tambare, O. H., & More, A. P. 2022. Performance of various fillers in adhesives applications: A review. Polymer Bulletin, **79**(12), pp.10491-10553.

[27] Kanishka, K., & Acherjee, B. 2023. Revolutionizing manufacturing: A comprehensive overview of additive manufacturing processes, materials,

developments, and challenges. Journal of Manufacturing Processes, **107**, pp.574-619.

[28] Niranatlumpong, P., & Koiprasert, H. 2006. Improved corrosion resistance of thermally sprayed coating via surface grinding and electroplating techniques. Surface and Coatings Technology, **201**(3-4), 737-743.

[29] Gachot, C., Rosenkranz, A., Hsu, S. M., & Costa, H. L. 2017. A critical assessment of surface texturing for friction and wear improvement. Wear, **372**, pp.21-41.

[30] Kumar, V., Verma, R., Kango, S., & Sharma, V. S. (2021). Recent progresses and applications in laser-based surface texturing systems. Materials Today Communications, **26**, 101736.

[31] De Zanet, A., Casalegno, V., & Salvo, M. 2021. Laser surface texturing of ceramics and ceramic composite materials–A review. Ceramics International, **47**(6), pp.7307-7320.

[32] Malinauskas, M., Žukauskas, A., Hasegawa, S., Hayasaki, Y., Mizeikis, V., Buividas, R., & Juodkazis, S. 2016. Ultrafast laser processing of materials: from science to industry. Light: Science & Applications, **5**(8), e16133-e16133.

[33] Bonse, J., Kirner, S. V., Griepentrog, M., Spaltmann, D., & Krüger, J. 2018. Femtosecond laser texturing of surfaces for tribological applications. Materials, **11**(5), 801.

[34] Usumez A, Inan O, Aykent F. 2004. Bond strength of a silicone lining material to alumina-abraded and lased denture resin. J Biomed Mater Res Part B: Appl Biomater; **71**, pp.196–200.

[35] Harimkar, S. P., & Dahotre, N. B. 2006. Crystallographic and morphological textures in laser surface modified alumina ceramic. Journal of applied physics, **100**(2).

[36] Li, H., Liu, Y., Liu, Y., Zeng, Q., Hu, K., Lu, Z., & Liang, J. 2020. Effect of sintering temperature in argon atmosphere on microstructure and properties of 3D printed alumina ceramic cores. Journal of Advanced Ceramics, **9**, pp.220-231.

[37] Abdelmoula, M., Küçüktürk, G., Juste, E. ve Petit, F. 2022. Alüminanın toz yatağı seçici lazer işlemi: Tarama stratejilerinin incelenmesi. Uygulamalı Bilimler , **12** (2), 764.

[38] Zhang, C., Han, K., Zhou, D., Song, C., Xu, P., Wu, T., ... & Wu, Q. 2022. High concentration Tm3+ doped TeO2-Al2O3-BaF2 glass for~ 2 μm fiber lasers. Journal of Alloys and Compounds, **901**, 163592.

[39] Yang, Y., Chen, F., Shen, T., Pariatamby, A., Wen, X., Yan, M., & Kanchanatip, E. 2023. Catalytic depolymerization of waste polyethylene terephthalate plastic in supercritical ethanol by ZnO/γ-Al2O3 catalyst. Process Safety and Environmental Protection, **173**, 881-892.

[40] Wu, X., Xu, L., & Weng, D. 2004. The thermal stability and catalytic performance of Ce-Zr promoted Rh-Pd/γ-Al2O3 automotive catalysts. Applied Surface Science, **221**(1-4), 375-383.

[41] Liu, Q., Gu, F., Lu, X., Liu, Y., Li, H., Zhong, Z., ... & Su, F. 2014. Enhanced catalytic performances of Ni/Al2O3 catalyst via addition of V2O3 for CO methanation. Applied Catalysis A: General, **488**, 37-47.

[42] Khamverdi, Z., Rezaei-Soufi, L., Paik, H. H., Jabari, P., & Ahmadian, M. 2021. Evaluation of the Effect of Cavity Preparation Using Er, Cr: YSGG Laser on Microleakage of Class V Composite Restorations. Avicenna Journal of Dental Research, **13**(3), 81-85.

[43] El-Dehna, A. M., Alyaski, M. A., & Mostafa, M. H. 2021. Clinical Evaluation of Laser Versus Conventional Cavity Preparation Methods in Primary Teeth Restorations. Al-Azhar Dental Journal for Girls, **8**(3-C), 483-489.

[44] Gorucu, Y., Albayram, S., Balci, B., Hasiloglu, Z. I., Yenigul, K., Yargic, F., ... & Kiris, A. 2011. Cerebrospinal fluid flow dynamics in patients with multiple sclerosis: a phase contrast magnetic resonance study. Functional neurology, **26**(4), 215.

[45] Yazıcı, E., Gurgan, S. E. V. İ. L., Gutknecht, N., & Imazato, S. 2010. Effects of erbium: yttrium–aluminum–garnet and neodymium: yttrium–aluminum–garnet laser hypersensitivity treatment parameters on the bond strength of self-etch adhesives. Lasers in medical science, **25**, 511-516.

Koc. J. Sci. Eng., 7(1): (2024) 89-95 https://doi.org/10.34088/kojose.1349807

Kocaeli University

Kocaeli Journal of Science and Engineering

http://dergipark.org.tr/kojose

The Effect of Energy Saving in Wastewater Treatment Plant on the Environmental Sustainability of the Plant

Simge ÇANKAYA [1, *]

[1] *Department of Environmental Engineering, Kocaeli University, Kocaeli, 41001, Turkey,* ***ORCID:*** *0000-0003-3095-7826*

Article Info

Research paper

Received : *August 25, 2023*
Accepted : *February 15, 2024*

Keywords

Energy saving
Life cycle assessment
Sustainability
Wastewater treatment plant

Abstract

Wastewater treatment plants (WWTPs) have significant function for the urban water management. However, they can consume large amount of energy for reducing the pollutant concentration in aquatic environments. In this work, the effect of energy saving in the selected wastewater treatment plant (before and after the energy saving revisions) on the environmental sustainability of the plant was investigated by life cycle assessment (LCA). Two situations were assessed comparatively: WWTP-1 (before energy saving) and WWTP-2 (after energy saving). Life cycle impacts were evaluated in terms of both mid-point and end-point impact categories by ReCiPe 2016 methodology. The results showed that contribution of electricity consumption in WWTP-2 significantly decreased in almost all mid-point impact categories compared with WWTP-1. Considering damage assessment, overall environmental burden of WWTP-2 was determined to be 36% lower than WWTP-1. It was also noted that in addition to electricity saving, the method chosen for sludge disposal was decisive in the environmental performance of the wastewater treatment plant.

1. Introduction

Water-energy nexus is one of the crucial elements for sustainable development and wastewater treatment plants (WWTPs) are central to water-energy interactions [1]. Although WWTPs play an important role to improve the water quality, they consume large amount of energy during their life cycle to remove pollutants from aquatic environment [2].

According to the literature, electricity demand for wastewater treatment constitutes about 1% total consumption of a country [3]. In the United States, wastewater treatment consumes approximately 4% of all electrical power produced in the country [4].

Electricity consumption varies approximately 0.3 – 2.1 kwh/m^3 of treated wastewater in a conventional WWTP, and about 25-40% of operating costs is mainly related to electricity consumption [5]. It has been estimated that energy consumption in the WWTPs will continue to rise by 20% in the next 15 years [6]. Therefore, sustainable wastewater treatment processes must be developed in order to decrease electricity consumption and the carbon footprint of WWTPs [4].

There are numerous approaches to investigate the environmental sustainability aspects of production and consumption [7]. Life cycle assessment (LCA) methodology is one of them and is often used to evaluate environmental impacts of products and services throughout their life cycle [8,9]. It has been continuously developing over the past 30 years, with notable improvements at the modelling level both in the inventory and impact assessment [10]. Recently, many LCA studies have been conducted in the field of wastewater treatment [11-13].

In this study, environmental sustainability of the selected wastewater treatment plant before (called as WWTP-1) and after the energy efficiency revisions (called as WWTP-2) was assessed comparatively by life cycle approach. In addition to the mid-point impacts, end-point impacts were also evaluated in order to compare the environmental performance of the two situations. Additionally, the most dominant processes (electricity, chemical usage, transport, etc.) that contribute to impact categories were identified with process contribution analysis.

* Corresponding Author: simge.taner@kocaeli.edu.tr

2. Materials and Methods

2.1. Description of the WWTP

In this study, environmental sustainability of the selected WWTP was assesssed before and after the energy saving revisions in order to reveal the effect of electricity consumption on environmental performance of the plant. For this purpose, two situations were investigated by LCA: conventional wastewater treatment without energy saving (called as WWTP-1) and advanced biological wastewater treatment with energy saving after revision (called as WWTP-2). WWTP-2 is the improved version of the WWTP-1. In 2021, WWTP-1 was revised to progress the advanced treatment and energy saving. The treatment configuration of WWTP-1, which is a conventional activated sludge (CAS), was transformed to anaerobic-anoxic-aerobic (A^2O) treatment configuration after revision. A diffuser-blower system has been introduced in aeration tank. In addition, a submersible mixer was installed in the tanks. As a result of this revision, significant savings were achieved in electrical energy consumption. In addition to electricity consumption and treatment configuration, there are some other differences (sludge treatment method, transport distances, etc.) between operational stage of the WWTP-1 and WWTP-2. The main characteristics of the two WWTP systems were comparatively summarized in Table 1.

Table 1. Main characteristics of the WWTP-1 and WWTP-2.

Inflow	**WWTP-1**	**WWTP-2**
Flow rate (m^3/d)	25782	35040
Treatment configuration	CAS	A^2O
Sludge treatment	Sent to cement plant with heat recovery (100%)	Sanitary landfill (95%) Incineration (5%)
Pollutant concentrations (mg/L)		
Inflluent		
BOD	352	200
COD	778	753
TN	22.6	34.8
TP	2.54	5.02
SS	420	403
Effluent		
BOD	12.5	15.6
COD	33.5	22.4
TN	7.81	8.36
TP	0.93	0.75
SS	13.3	7.12

2.2. Life Cycle Assessment

Life cycle assessment was conducted by four steps according to the ISO 14040: goal and scope definition, inventory analysis, impact assessment, and interpretation (ISO, 14040).

The goal of this LCA study is to determine the effect of energy saving in wastewater treatment plant on its environmental sustainability. Two situations (called as WWTP-1 and WWTP-2) were compared to achieve this goal. The scope of this LCA can be defined as "expanded gate-to-gate" that includes operational stage of wastewater treatment plant. System boundary constitutes transportation of chemicals to the WWTP, electricity and chemical consumption for WWTP operations, transportation of sewage sludge to disposal site, and treatment of sewage sludge. The functional unit (FU) was chosen as 1 m^3 of wastewater.

For inventory analysis, foreground and background data were used. Foreground data was obtained from operating reports of the selected WWTP and it includes the amount of chemical substances, suppliers of chemicals, electricity consumption, effluent concentration, air emissions, and waste declarations (the amount of wastes generated in plant and disposal methods). Background data (production of chemicals used in the WWTP, electricity grid mix, etc.) was obtained from Ecoinvent 3.7.1 database embedded in SimaPro (v.9.2). All input and output data for WWTP-1 and WWTP-2 were summarized in Table 2.

Table 2. Input and output data for LCA (FU: 1 m^3 of treated wastewater)

Parameter	**WWTP-1**	**WWTP-2**
Input:		
Land (m^2)	4.93E-03	4.08E-04
Chemical (kg):		
Polyelectrolyte	9.94E-04	5.71E-04
Iron (III) chloride		1.32E-02
Electricity consumption (kWh)	6.89E-01	5.47E-02
Transport (tkm):	2.49E-02	4.99E-01
Output:		
Air emissions (g):		
CH_4	3.72E+00	1.33E+00
N_2O	2.72E+00	2.09E+00
Water emissions (g):		
BOD	1.25E+01	1.56E+01
COD	3.35E+01	2.24E+01
TN	7.81E+00	8.36E+00
TP	9.30E-01	7.50E-01
SS	1.33E+01	7.12E+00
Wastes:		
Sewage sludge to treatment (kg)	3.64E-01	1.41E+00
Other wastes (kg)	7.50E-04	3.18E-02

Life cycle impact assessment is the third step of LCA process and constitutes compulsory (category definition, classification, characterization) and optional (normalization, grouping, and weighting) stages (ISO 14040). In this study, characterization (mid-point analysis) and damage (end-point analysis) assessment were conducted to evaluate the environmental performance of the selected WWTP. For this purpose, eighteen mid-point impact categories were evaluated using ReCiPe 2016 (v.1.03) Mid-point method, Hierarchist version; and three end-point impact categories were determined using ReCiPe 2016 (v.1.03) End-point method, Hierarchist version. The End-point method is used to aggregate results into three higher aggregation levels: environmental impact to human health, damage to ecosystems, and damage to resource availability (Life cycle assessment of mechanical recycling of post-consumer polyethylene flexible films based on a real case in Spain). Additionally, normalization and weigthting were performed to reveal most dominant end-point impact categories related to the wastewater treatment.

In the interpretation step, which is the final step of LCA, the effect of energy saving in the wastewater treatment was investigated and process contribution analysis was conducted to determine the significant processes that contribute to mid-point and end-point impact categories. Additionally, uncertainty analysis was conducted to reveal the difference between two situations (WWTP-1 and WWTP-2). Interpretation of comparisons was performed by Monte Carlo Simulation using SimaPro software (v.9.2). 1000-run were used for both situations.

3. Results and Discussion

3.1. Characterization Results

Life cycle impact assessment results of WWTP-1 and WWTP-2 were given in Table 3, comparatively. According to the Table 3, the impact categories of stratospheric ozone depletion, fine particulate matter formation, terrestrial acidification, freshwater eutrophication, human carcinogenic toxicity, and fossil resource scarcity in WWTP-2 were lower than WWTP-1. Especially human carcinogenic toxicity is quite low in WWTP-2 compared to WWTP-1. On the contrary, the other mid-point impact categories were determined higher in WWTP-2 compared to WWTP-1. The impact category of marine eutrophication was by far larger in WWTP-2, followed by mineral resource scarcity, ionizing radiation, and marine ecotoxicity. It is thought that the main reasons for this increase are the differences in the operational processes of WWTP-2 and WWTP-1 (sludge treatment method, transportation distances of sludge and chemicals, amount of chemicals, etc.). Apart from electrical energy savings, the most important difference between the operational stages of the two situation is the preferred method for the disposal of treatment sludge. While in WWTP-1, sewage sludge was sent to cement plant for incineration with heat recovery, in WWTP-2 sewage sludge was sent to sanitary landfill for final disposal.

Table 3. Characterization results.

Impact category	Unit	WWTP-1	WWTP-2
Global warming	kg CO_2 eq	1.33E+00	2.56E+00
Stratospheric ozone depletion	kg CFC11 eq	3.00E-05	2.41E-05
Ionizing radiation	kBq Co-60 eq	1.27E-04	1.87E-03
Ozone formation, Human health	kg NOx eq	8.83E-04	1.03E-03
Fine particulate matter formation	kg $PM_{2.5}$ eq	5.39E-03	8.01E-04
Ozone formation, Terrestrial ecosystems	kg NOx eq	9.55E-04	1.05E-03
Terrestrial acidification	kg SO_2 eq	2.11E-03	1.12E-03
Freshwater eutrophication	kg P eq	9.95E-04	9.53E-04
Marine eutrophication	kg N eq	4.92E-06	8.25E-03
Terrestrial ecotoxicity	kg 1,4-DCB	-4.24E-02	1.71E+00
Freshwater ecotoxicity	kg 1,4-DCB	1.83E-04	5.50E-04
Marine ecotoxicity	kg 1,4-DCB	2.17E-04	1.68E-03
Human carcinogenic toxicity	kg 1,4-DCB	2.38E-03	-7.90E-03
Human non-carcinogenic toxicity	kg 1,4-DCB	6.15E-02	8.82E-02
Land use	m^2a crop eq	-2.55E-02	1.23E-02
Mineral resource scarcity	kg Cu eq	6.91E-05	1.17E-03
Fossil resource scarcity	kg oil eq	1.03E-01	6.67E-02
Water consumption	m^3	2.48E-03	8.96E-04

For more detailed analysis, process contribution analysis was performed and the results were given in Figure 1. When Figure 1 was examined, it was clearly seen that contribution of electricity consumption on mid-point impact categories significantly decreased by electrical energy saving in WWTP-2 compared to WWTP-1. On the contrary, electricity consumption has significant contribution (above 90%) on almost all mid-point impacts (resource scarcity, freshwater ecotoxicity, ozone formation, toxicity, water consumption, fine particulate matter formation, and terrestrial acidification) in WWTP-1. The lowest contributions of electricity consumption was determined for stratospheric ozone depletion (0.40%), land use (5.05%), and freshwater eutrophication (6.54%). It was also observed that chemical consumption (polyelectrolyte) has high contribution (83%) on marine eutrophication for WWTP-1. Compared with WWTP-2, it is possible to say that the most important environmental friendly process was sludge treatment. In WWTP-1, dewatered sewage sludge (22% SS) is sent to cement plant, where sludge is dried by using waste heat and used as an alternative fuel in clinker manufacturing process. Treatment of sewage sludge by incineration for energy recovery ensures environmental gains on almost all mid-point impact in WWTP-1 as can be seen from Figure 1. The highest environmental gains of this process were determined on land use and terrestrial ecotoxicity (approximately 100%).

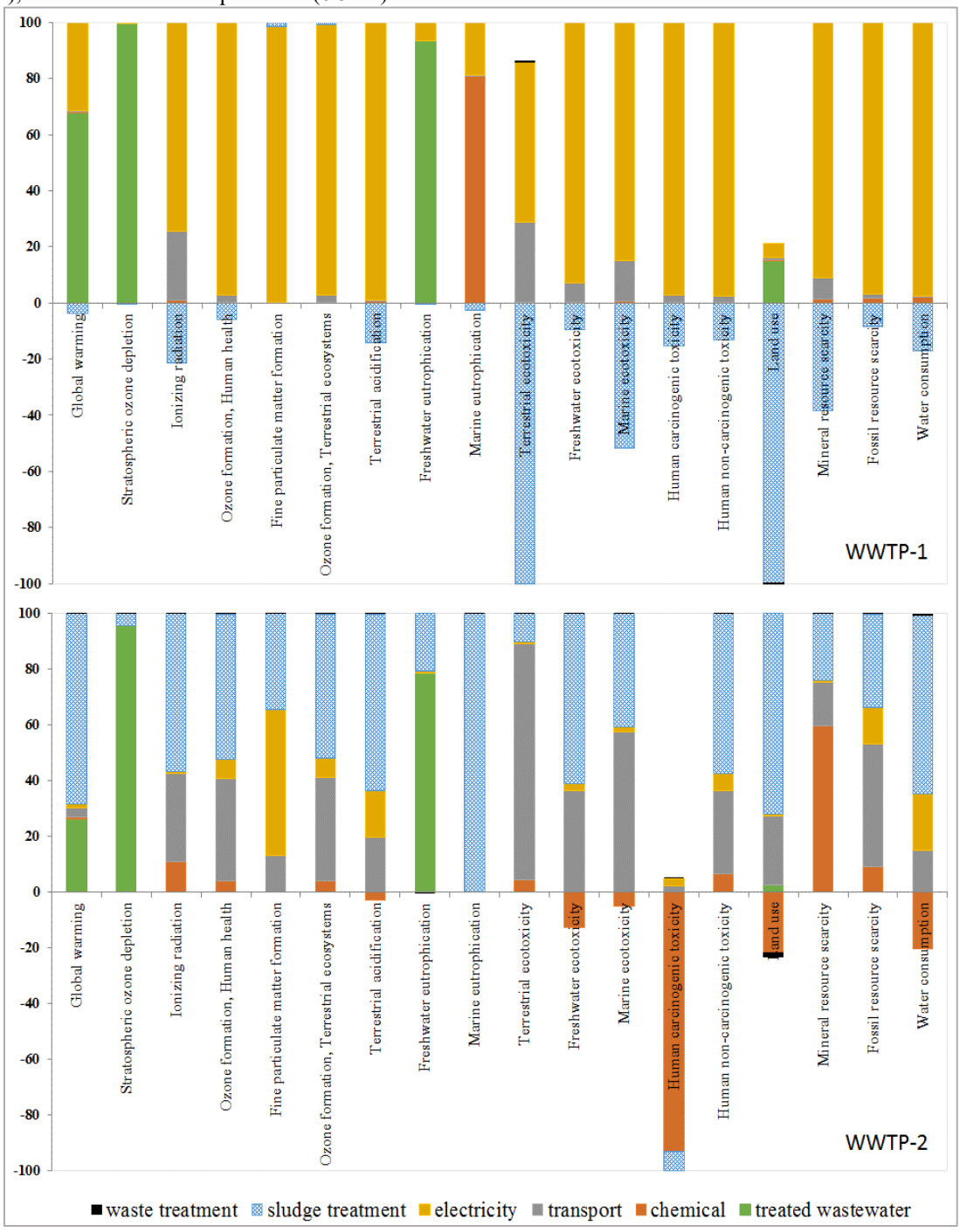

Figure 1. Process contributions to characterization results for WWTP-1 and WWTP-2.

Comparing with WWTP-1, the significant increase of marine eutrophication in WWTP-2 is mainly related to the treatment method of sewage sludge as can be seen from Figure 1. In WWTP-2, sewage sludge is sent to sanitary landfill for final disposal. It was observed that almost all the marine eutrophication impact category (99.9%) was associated with the landfill process according to the process contribution analysis (Figure 1). While energy saving in WWTP-2 ensures significant environmental advantages on almost all mid-point impacts, disposal of sewage sludge by sanitary landfill has adversely affected some of the mid-point impact categories. Treatment of sludge by sanitary landfill has significant contribution on land use (71.8%), global warming (68.4%), water consumption (68.4%), terrestrial acidification (63.3%), and freshwater ecotoxicity (60.9%). On the contrary, treatment of sludge by sanitary landfill ensures 7% environmental saving on human carcinogenic toxicity impact category. Additionally, it is noteworthy that consumption of iron (III) chloride provides 93% environmental gain on human carcinogenic toxicity. In alignment with this result, Selvarajan (2020) has also determined that preffering the iron (III) chloride as a coagulant decreased the human health impacts [14].

3.2. Damage Assessment Results

Three end-point impact categories were evaluated within the scope of damage assessment that was modelled by ReCiPe 2016 End-point (H) methodology: Resources (resource consumption), ecosystems (damage to ecosystems), and human health (damage to human health). After normalization and weigthing step, the results in milipoints (mPt) obtained from ReCiPe 2016 End-point (H) method were presented in Figure 2. As can be seen from Figure 2, overall environmental burden of WWTP-1 was 55% higher than WWTP-2 regarding environmental sustainability. Damage to human health constitues 97.6% and 93.5% of overall environmental burden for WWTP-1 and WWTP-2; respectively. Considering the mid-point impacts that contribute to human health impact category, it was identified that the main responsible mid-point impact category was fine particulate matter that is mainly related to electricity consumption for WWTP-1. For WWTP-2, the main dominant mid-point impact category that damages human health was determined as global warming that is mainly related to sludge treatment.

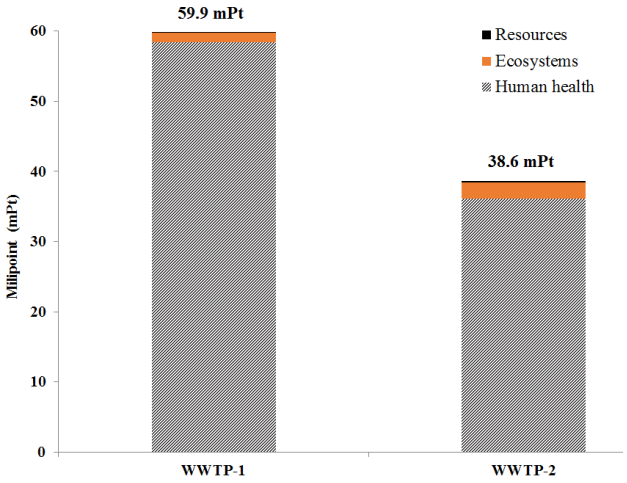

Figure 2. Damage assessment results of WWTP-1 and WWTP-2.

3.3. Uncertainty Analysis

Monte Carlo simulation results of damage assessment and single score for comparing WWTP-1 and WWTP-2 were given in Figure 3(a) and Figure 3(b), respectively. It showed that WWTP-2 preceded WWTP-1 with respect to human health impact category (93%). On the other hand, WWTP-1 was better in 93% and 94% of the iterations for resources and ecosystems. Considering the uncertainty analysis results of single score, WWTP-2 preceded WWTP-1 in terms of overall environmental burden (84%).

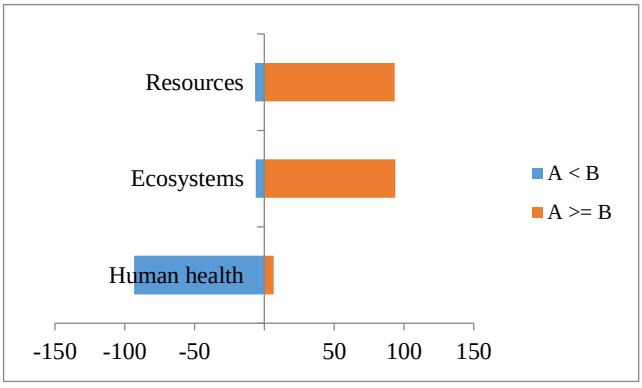

(a)

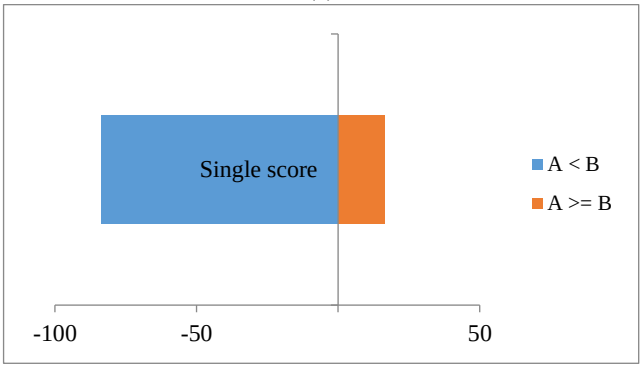

(b)

Figure 3. The results of uncertainty analysis of damage assessment (a) and single score (b). (A: WWTP-2, B: WWTP-1).

4. Conclusions

In this study, the effect of electrical energy saving on the selected WWTP to its environmental sustainability was investigated by life cycle assesment. Both mid-point and end-point impact analysis was conducted within the scope of this LCA study. The results have shown that adverse effects of electricity consumption decreased in almost all mid-point impact categories. However, treatment method of sewage sludge has significant effects on the mid-point impact categories. By energy saving, overall environmental burden of WWTP-2, which is the revised version of WWTP-1, have decreased 36% compared to WWTP-1. Considering with a life-cycle approach, the results indicated that damage to human health was the most significant category related to the wastewater treatment, and efficiency in electrical energy consumption plays a significant role in order to ensure the environmental sustainability in WWTPs. The results of this study can be beneficial in terms of demonstrating that ensuring energy efficiency in wastewater treatment plants has a significant contribution to environmental sustainability.

Declaration of Ethical Standards

The author(s) of this article declare that the materials and methods used in this study do not require ethical committee permission and/or legal-special permission.

Conflict of Interest

The authors declare that they have no known competing financial interests or personal relationships that could have appeared to influence the work reported in this paper.

Acknowledgements

This work was supported by Kocaeli University Scientific Research Projects Coordination Unit. Project Number: FKA-2020-2087.

References

[1] Maktabifard M., Zaborowska E., & Makinia J., 2018. Achieving energy neutrality in wastewater treatment plants through energy savings and enhancing renewable energy production. Reviews in Environmental Science and Bio/Technology, **17**, pp.655-689.

[2] Çankaya S., 2023. Evaluation of the impact of water reclamation on blue and grey water footprint in a municipal wastewater treatment plant. Science of The Total Environment, 166196.

[3] Longo S., d'Antoni B. M., Bongards M., Chaparro A., Cronrath A., Fatone F., ... & Hospido A., 2016. Monitoring and diagnosis of energy consumption in wastewater treatment plants. A state of the art and proposals for improvement. Applied energy, **179**, pp.1251-1268.

[4] Yan P., Qin R. C., Guo J. S., Yu Q., Li Z., Chen Y. P., & Fang F., 2017. Net-zero-energy model for sustainable wastewater treatment. Environmental science & technology, **51**(2), pp.1017-1023.

[5] Panepinto D., Fiore S., Zappone M., Genon G., & Meucci L., 2016. Evaluation of the energy efficiency of a large wastewater treatment plant in Italy. Applied Energy, **161**, pp.404-411.

[6] Gu Y., Li Y., Li X., Luo P., Wang H., Wang X., & Li F., 2017. Energy self-sufficient wastewater treatment plants: feasibilities and challenges. Energy Procedia, **105**, pp.3741-3751.

[7] Heijungs R., Huppes G., & Guinée J. B., 2010. Life cycle assessment and sustainability analysis of products, materials and technologies. Toward a scientific framework for sustainability life cycle analysis. Polymer degradation and stability, **95**(3), pp.422-428.

[8] ISO 14040 Environmental Management – Life Cycle Assessment – Principles and Framework. International Organization for Standardization, Geneva, Switzerland (2006).

[9] Gallego-Schmid A., & Tarpani R. R. Z., 2019. Life cycle assessment of wastewater treatment in developing countries: a review. Water research, **153**, pp.63-79.

[10] Sala S., Farioli F., & Zamagni A., 2013. Life cycle sustainability assessment in the context of sustainability science progress (part 2). The International Journal of Life Cycle Assessment, **18**, pp.1686-1697.

[11] Risch E., Boutin C., & Roux P., 2021. Applying life cycle assessment to assess the environmental performance of decentralised versus centralised wastewater systems. Water Research, **196**, 116991.

[12] Patel K., & Singh S. K., 2022. A life cycle approach to environmental assessment of wastewater and sludge treatment processes. Water and Environment journal, **36**(3), pp.412-424.

[13] Sheikholeslami Z., Ehteshami M., Nazif S., & Semiarian A., 2022. The environmental assessment of tertiary treatment technologies for wastewater reuse by considering LCA uncertainty. Process Safety and Environmental Protection, **168**, pp.928-941.

[14] Selvarajan S., 2021. Cradle-to-Gate LCA of Water Treatment Alternatives: A case study performed for Norrvatten's future waterwork expansion.